

# Nanoscale Coherent Control

Ultrafast dynamics of single molecules, individual light harvesting complexes and discrete nanoantennas at room temperature.

Daan Brinks

ICFO – Institut de Ciències fotòniques  
Universitat Politècnica de Catalunya  
Barcelona, 14 Juny 2012



# Nanoscale Coherent Control

Ultrafast dynamics of single molecules, individual light harvesting complexes and discrete nanoantennas at room temperature.

Daan Brinks

under the supervision of

Professor Niek F. van Hulst

submitted this thesis in partial fulfillment

of the requirements for the degree of

Doctor

by the

Universitat Politècnica de Catalunya  
Barcelona, 14 June 2012



*De dwaas weet zich, zoo ik mij niet vergis, het ware verstand van zaken eigen te maken door op alles los te gaan en zijn persoon aan alles te wagen.*

- Erasmus, Lof der Zotheid

*If any man is able to convince me and show me that I do not think or act rightly, I will gladly change; for I seek the truth, by which no man was ever injured. But he is injured who abides in his error and ignorance.*

- Marcus Aurelius, Meditations

*Dejate llevar.*

- Margherita Massaiu, The... Show



# Abstract

Ultrafast pulses allow observation of molecular dynamics with femtosecond time resolution through pump probe experiments. This provides information about the quantummechanical nature of complex molecular systems, and the dynamics and interactions that play a role in e.g. biophysical and biochemical processes at the cellular level. Since especially at room temperature, coherent effects that would point to quantummechanical rather than classical dynamics, are expected to dephase fast, this time resolution is required to investigate the intriguing transition from quantummechanical to classical mechanics in molecular systems.

However, averaging over an ensemble of molecules tends to wash out phase sensitive information as well, due to the intrinsic inhomogeneity in molecular conformations, orientations and interactions that lead to unique potential energy landscapes for each molecule. On top of that, in functioning biological systems, the position of a molecule in a supramolecular structure and the conformation, orientations and interactions that are the consequence of this, directly reflect the function the molecule has.

It is therefore important to go beyond the ensemble average when looking at quantum dynamics of organic systems at room temperature, and resolve the behaviour of specific molecules on an individual basis.

In this thesis, we show that it is possible to create, manipulate and observe ultrafast coherent effects in single molecules at room temperature, and resolve a certain measure of environmental influence on the specific dynamics of each molecule. Moreover, we apply this insight to investigate a functional light harvesting biosystem, and lay the basis for a technique that has the time and space resolution required to observe these systems *in vivo*.

In chapter 2, we investigate the possibility of controlling ultrafast pulses at the high-NA diffraction limit, and come to conclusions about the procedure to follow there that hold for all pulse-shaping experiments. We show in proof of principle experiments that we can control the ultrafast characteristics of optical pulses in nanometric excitation volumes.

In chapters 3 and 4 we create, detect and control, for the first time, ultrafast quantum dynamics of single organic molecules at room temperature. We establish that typical coherence times in these systems are of the order of 50 fs and show that superposition states can be manipulated as long as the manipulation is faster than that. This leads to the first observation of rabi-oscillations in room temperature single molecules, and to ultrafast operation of an organic qubit.

We show that we can create multilevel, non-stationary superposition states within 50 fs (wavepackets, composed of several vibrational levels) and probe the influence of the local environment on their composition and dynamics. Finally we show we can optimize the state preparation protocol for each individual molecule in its own nanoenvironment, leading to significantly higher fidelity of state preparation than in comparable systems in bulk. In these

chapters we lay out the proof of principle work of detecting the quantumdynamics of a complex system in interaction with its environment at room temperature.

In chapter 5 we apply these techniques to the intriguing phenomenon of long lived coherence in photosynthetic systems. We show for the first time unambiguously that electronic coherence between different rings of the LH2 system persists to time scales of 100s of femtoseconds, an order of magnitude beyond expectation for systems of this complexity. Moreover we show that the energy transfer pathways in LH2 adapt to environmentally induced changes in the molecule and that the nature of the transfer remains coherent for each pathway, providing strong evidence that coherent energy transfer is the optimum process for energy transfer in photosynthesis.

Finally, in chapter 6 we take the technical development one step further and create a framework based on plasmonic antennas that allows for control of the amplitude-phase characteristics in nanometric sized hotspot fields. We show for the first time that the ultrafast characteristics of plasmonic hotspots can directly be engineered through design of the plasmonic system and experimentally demonstrate two much-anticipated examples: a sub-diffraction resolution phase shaper, and an ultrafast plasmonic switch for pump probe experiments.

The results presented in this thesis form the first induction and observation of ultrafast coherent dynamics in individual molecular systems at room temperature. This is a necessary step to be able to do true quantum tomography in complex systems, resolve the influence of the environment on molecular dynamics, and investigate the physics that determines evolutionary optimization and functionality in biomolecules.

# Contents

<b>Abstract</b>	<b>v</b>
<b>Contents</b>	<b>vii</b>
<b>1. Introduction</b>	<b>1</b>
1.1 Ultrafast and ultrasmall	2
1.2 Single molecule detection	3
1.3 Pulse shaping	5
1.4 Ultrafast spectroscopy	9
1.5 Plasmonics	10
1.6 Conclusions	12
<b>2. Beating spatio-temporal coupling: implications for pulse shaping and coherent control experiments</b>	<b>15</b>
2.1 Introduction	16
2.2 Experimental method	17
2.3 Experimental quantification of spatio-temporal coupling	18
2.4 Fourier analysis of spatio-temporal coupling in 4f – pulse shapers	22
2.5 Reduction and compensation of spatio-temporal coupling	25
2.6 Fourier analysis of spatio-temporal coupling in the double pass scheme	26
2.7 Experiments free of spatio-temporal coupling	29
2.8 Conclusions	33
<b>3. Femtosecond coherence and quantum control of single molecules at room temperature</b>	<b>35</b>
3.1 Introduction	36
3.2 Experimental method	39
3.3 Coherence in single molecules at room temperature	39
3.4 Rabi-oscillation in a single molecule at room temperature	43
3.5 Control of the superposition state: a room temperature single molecule ‘qubit’.	44
3.6 Conclusions	48
<b>4. Visualizing and manipulating vibrational wavepackets of single molecules at room temperature</b>	<b>51</b>
4.1 Introduction	52
4.2 Experimental method	55
4.3 Wave packet oscillations in a single molecule at room temperature	56
4.4 Phase control of wavepacket interference	61
4.5 Conclusions	63

<b>5. Quantum coherence persists in time-varying energy transfer in light-harvesting complexes</b>	<b>67</b>
5.1 Introduction	68
5.2 Experimental method	69
5.3 Persistent coherence in single LH2	74
5.4 B800-B850 inter-band energy transfer in LH2	78
5.5 Coherence mediates robust energy transfer under external perturbation	85
5.5 Conclusions	88
<b>6. Plasmonic nanoantennas as design elements for coherent ultrafast nanophotonics</b>	<b>91</b>
6.1 Introduction	92
6.2 Experimental method	93
6.3 Phase measurements through antenna signatures	95
6.4 The building blocks: single bar antennas	99
6.5 The subwavelength resolution phase shaper	101
6.6 The ultrafast plasmonic switch	103
6.7 Conclusions	105
<b>Conclusion</b>	<b>107</b>
<b>Acknowledgments</b>	<b>111</b>
<b>Publications</b>	<b>115</b>
<b>Bibliography</b>	<b>117</b>

# **1. Introduction**

## 1.1 Ultrafast and ultrasmall

Let's start this thesis with an observation that should not shock anybody: physicists and chemists do science differently than biologists and medical researchers. Particularly, the approach towards complexity is different: physicists and chemists tend to investigate complex systems by figuring out its constituent components and their mutual interactions, whereas biologists and medical researchers tend to focus on the function of the complex system as a whole and its response to external stimuli. This is not just a practical, but a philosophical difference: chemists and physicists look for natural laws that hold generally, whereas biologists and medical researchers are more interested in particular incarnations of natural phenomena occurring under well-controlled, but specific, conditions.

This thesis is about breaking down the barrier between these two domains. It builds on the dream of looking at systems that are big (up to millions of atoms), messy (interacting in any conceivable way with any other construct that might appear in its environment) and hot (existing at room temperature where conventional wisdom says thermal averages are dominant) and yet being able to differentiate them down to the molecular and sub-molecular level and describe their behaviour, their dynamics, and their function in terms of generally applicable, fundamental physical laws.

Zooming in on complex systems to this level requires a quantummechanical description of matter, its dynamics and its interaction with light. The challenge faced here lies in introducing quantummechanical descriptions in regimes of temperature, density and complexity that are usually firmly classical. Hence, this thesis is also about the fundamental difference between one single molecule and an ensemble; about the limits of what constitutes "a quantum system"; about the elusive regime where a construct of multiple molecules becomes one single molecule; and about the intriguing transition between classical and quantummechanical descriptions of complex systems. If this thesis would need to have a theme, it would be summarized thus: the search for nontrivial quantummechanical aspects of the dynamics of complex molecular systems at room temperature.

At the heart of this is the concept of coherence: coherence in the exciton basis, i.e. between eigenstates of a quantum system, indicative of quantum dynamics in the system under investigation induced by interaction with coherent light, and coherence in the site basis, i.e. between different physical parts of a quantum system (or different quantum systems), indicative of a delocalized wavefunction between spatially separate parts of molecular complexes.

In dense, room temperature environments coherence typically decays fast enough for it to be unclear how fast exactly, for the visualization of coherence to be a technical challenge and for it to be an open question whether coherence can play any relevant role in biochemical processes. To investigate this, it is necessary to look at time and length scales where coherence has a chance of surviving. We do this by investigating single molecules at femtosecond timescales.

This thesis contains technical development of the setup needed to reach this time domain and to maintain phase sensitivity, necessary to probe coherence. It contains proof of principle results investigating the physical limits of coherent manipulation of a single molecule under ambient conditions, and application of the proof of principle results to biologically functional systems. It comes full circle with the technological development of the necessary next step to bring this research to the next level: to achieve true sub-diffraction limit resolution while retaining phase information.

Of course, the techniques utilized in the research presented here do not come from scratch: we built on proven concepts of single molecule detection, phase shaping, ultrafast spectroscopy and plasmonics to come to our results. Each of these fields will briefly be introduced here.

## 1.2 Single molecule detection

Ironically, the first single molecules were detected in absorption<sup>1</sup>. This is ironic, because it implies the possibility of detection of coherent signals from single molecules, which would make the task we set ourselves considerably easier. Unfortunately, this works at cryogenic temperatures with spectrally very narrow excitation<sup>2</sup>: this allows for a near perfect spectral overlap between the excitation dipole and the excitation light, leading to an extinction that is visible when narrowband laser systems are used with tight focusing<sup>3</sup> or near field excitation<sup>4</sup>.

At room temperature, this was long impossible due to the homogeneous broadening of the spectral lines. Despite this, several groups have made heroic efforts to detect single molecules with an absorption-based signal, which paid off last year: the Orrit group succeeded in detecting the change in refractive index of a polymer matrix around a single molecule, caused by the dissipation of excitation energy<sup>5</sup>. They were followed by the Sandoghdar group, who worked on minimization of laser noise and scattering noise until the single molecule absorption was visible directly<sup>6,7</sup>. This result was published back to back with that of the Xie group, who used a modulated laser beam to detect groundstate depletion<sup>8</sup>. Relevant in this context is that the Xie group also detected stimulated emission signals from highly diluted solutions of dye molecules, with claims of only 5-10 molecules contributing to the signal<sup>9</sup>.

However, the method of choice for room temperature single molecule spectroscopy and imaging is still fluorescence detection. First developed by Orrit and Bernard<sup>10</sup>, it was made into an imaging method at cryogenic temperature by Güttler et al<sup>11</sup> and optimized for room temperature usage by Betzig et al<sup>12,13</sup>, Ambrose et al<sup>14</sup>, Macklin et al<sup>15</sup> and Xie et al<sup>16,17</sup>. It relies on the emission of a stokes shifted fluorescent photon by a single molecule upon excitation<sup>18,19</sup>. Due to the spectral separation between excitation and emission, the excitation signal can be filtered out using colored or dichroic filters, to the point where the only photons in the signal are those emitted by the molecule. The only relevant noise sources then become the shot noise of the fluorescence itself, due to limited photon counts, and the dark noise of the detectors i.e. signal from the detector without an incident photon.

Dark noise can largely be avoided by applying photon counting instead of recording the photons as an analogue signal. Photon Counters (Photomultiplier Tubes and APDS can be used in this way) with backgrounds as low as 25 counts per second exist, meaning that a molecule emitting more than 25 photons per second can in principle be detected (adjusted for the detection efficiency of the total setup).

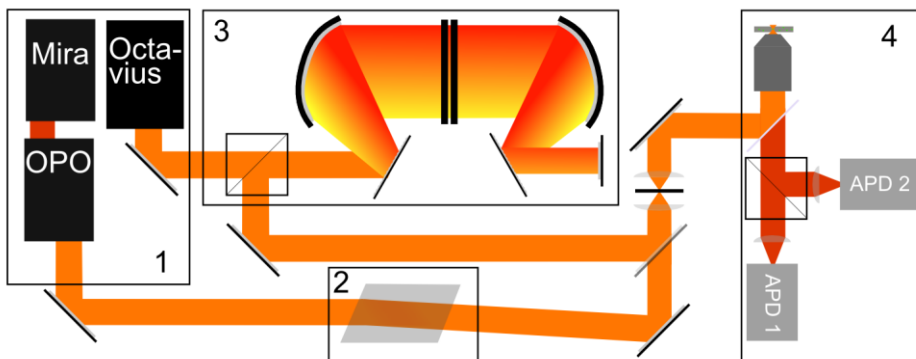


Figure 1.1: **Schematic sketch of the setups used for the work in this thesis.** 1. Pulsed laser sources. 2. Dazzler AOPDF. 3. Double Pass 4f shaper. 4. Confocal Microscope with polarization sensitive detection on two APDs.

Single molecule detection has found wide application in physics, chemistry and biology; schemes like PALM<sup>20,21</sup> and STORM<sup>22</sup> have become particularly popular and rely on the fundamental single molecule properties of one-step switching or blinking. Resolution here is based on a fitting algorithm and the molecules are used as labels, leading to an artificial increase in resolution and making it hard to do prolonged experiments on one particular molecule.

Confocal microscopy is still the technique of choice to achieve true high (setup-limited) resolution and perform prolonged experiments on the same molecule. The technique was first patented by Marvin Minsky<sup>23</sup> and relies on a double focusing mechanism: using a high NA objective, light is focused into a sample, which is then scanned through the focus. Any fluorescence is collected through the same objective, separated from the excitation light through suitable dichroic mirrors and long-pass filters, and projected onto a pinhole. This pinhole rejects any fluorescence that does not come from the area in the sample where the laser beam is focused: its effectiveness depends on the image of the pinhole that is projected in the sample and how well that overlaps with the laser focus. Ideally, when excitation and detection are truly confocal, this scheme leads to a resolution of  $\lambda/[2NA]$ , with  $\lambda$  the excitation wavelength and NA the numerical aperture of the objective.

This is the technique we will apply in our experiments (Fig 1.1): it allows for a true high setup-resolution and optimization of the detection efficiency.

## 1.3 Pulse shaping

Confocal microscopy provides the spatial resolution needed for our experiments. The temporal resolution has to come from ultrashort laser pulses. The combination is a challenge in itself, since the objectives necessary for high spatial resolution introduces a large amount of dispersion, typically in the 5000 fs<sup>2</sup> range. This will elongate any laser pulse that would be ten femtoseconds in the Fourier limit to hundreds of femtoseconds. We used pulse shapers to compensate for this dispersion and to create the shapes needed for our experiments (see chapter 2).

For relatively narrowband, relatively long pulses we used a Dazzler Acousto-Optical Programmable Dispersive Filter (AOPDF)<sup>24-26</sup> to apply a phase shape compensating for the dispersion of the objective. The Dazzler functions by application of an acoustic Bragg grating in a birefringent crystal. The polarization of the diffracted light rotates, meaning that it will experience a different refractive index. Due to the difference between the ordinary and extraordinary refractive index, the time it takes for light with horizontal polarization to traverse the crystal is 8ps longer than it is for light with vertical polarization. Since the refraction requires phase matching between the optical and acoustic wave, an applied chirped acoustic pulse determines the position in the crystal along the propagation direction where the polarization is rotated for each wavelength: this determines the total traversal time through the crystal for each wavelength. Changing the dispersion of the acoustic pulse therefore changes the dispersion of the optical pulse. This way, a precompensation phase was added based on an autocorrelation signal and documented values for the dispersion of the objective<sup>27</sup>.

For the relatively narrowband pulses this works, since a couple of fs<sup>2</sup> more or less will not fundamentally change the pulse shapes. However, for truly wideband pulses, this method does not suffice because a small inaccuracy in dispersion will cause a huge change in pulse length. Moreover, we are trying to detect minimal phase changes in our experiments (chapters 5 and 6) so a robust method is necessary to determine the spectral phase at the focal point.

For the measurement of the spectral phase of wideband pulses and compensation of their dispersion we used a modified 4f pulse shaper based on a double layer liquid crystal spatial light modulator<sup>28-31</sup>, and measured the dispersion of the total setup using a micrometric sliver of BBO crystal on a microscope coverslip. Through calibration of the focal spot shape we could determine the transition between glass and crystal, which allowed us to do the dispersion compensation focused right above the coverslip; the crystal is this thin to be able to accept all incoming wavevectors, i.e. to ensure that all angular and spectral frequencies contribute to a second harmonic spectrum and no phasematching conditions give a distorted (i.e. narrowed) second harmonic spectrum. This ensured that all conditions were the same for the calibration and the experiment, and that the calibration signal was taken from the same point as the measurement, i.e. at the top surface of the coverslip.

The calibration works as follows: we focus a pulse between 10 and 15 fs on the transition between the glass and the BBO crystal, collect the Second Harmonic Signal generated in transmission through a lens and focus it on the opening of an Ocean Optics Vis-UV fiber (aperture size 200  $\mu\text{m}$ ) leading to an Ocean Optics Vis-UV Spectrometer (Fig 1.2). This gives us a second harmonic Spectrum that depends on the Spectral amplitude and phase as follows: For a laser pulse with a spectrum centered at  $\omega_0$  and spectral amplitude and phase  $E(\Delta)e^{i\varphi(\Delta)}$  at  $\Delta=\omega-\omega_0$ , the spectral intensity of the second Harmonic Signal at a frequency  $\omega_{\text{SHG}}=2(\omega_0+\Delta)$  is given by<sup>32</sup>

$$SHG(\Delta) \propto \left| \int |E(\Delta + \Omega)| |E(\Delta - \Omega)| e^{i[\varphi(\Delta + \Omega) + \varphi(\Delta - \Omega)]} d\Omega \right|^2 \quad (1.1)$$

where the integration variable  $\Omega$  is a detuning from the central frequency  $\omega_0$  similar to  $\Delta$ . This already makes clear that the second harmonic intensity depends on the spectral phase in the fundamental spectrum.

Assuming continuous phases,  $\varphi(\Delta + \Omega) + \varphi(\Delta - \Omega)$  can be expanded into a Taylor series reading  $\varphi(\Delta + \Omega) = \varphi(\Delta) + \Omega\varphi'(\Delta) + 1/2\Omega^2\varphi''(\Delta) + \dots$ , so that  $\varphi(\Delta + \Omega) + \varphi(\Delta - \Omega)$  simplifies to  $2\varphi(\Delta) + \Omega^2\varphi''(\Delta) + \dots$ . Plugging this back into Eq. (1.1) we see that the common phase integrates out, i.e. does not influence the shape of the second harmonic spectrum, and the first derivative of the phase has fallen out of the Taylor expansion. This also makes intuitive sense: the common phase of a pulse, i.e. a constant spectral phase, i.e. a constant shift in carrier-envelope phase does not change the shape of a pulse; nor does a linear spectral phase, which is a delay of the complete pulse. These parameters are equally irrelevant for our experiments since our systems under investigation always relax back to the ground state between pulses and we shape the entire experiment out of one excitation pulse, i.e. only relative carrier-envelope phases and delays matter; absolute ones do not.

The leading term in the Taylor expansion is the second derivative of the phase,  $\varphi''(\Delta)$ . Intuitively, this again makes sense: The first function that will influence a pulse shape is quadratic phase, i.e. chirp; all higher order phases also influence pulse shape, which is clear from the fact that they will have non-zero second derivatives at some points in the spectrum.

This consideration gives us a condition to measure the dispersion: the signal at a particular  $\omega_{\text{SHG}}=2(\omega_0+\Delta)$  will be maximum if  $\varphi''(\Delta)=0$ . If we expand  $\varphi''(\Delta)$  into a known phase added in the shaper and an unknown dispersion:  $\varphi''(\Delta) = \varphi''_{\text{shaper}}(\Delta) + \varphi''_{\text{dispersion}}(\Delta)$ , we need to solve.

$$\varphi''_{\text{shaper}}(\Delta) + \varphi''_{\text{dispersion}}(\Delta) = 0 \quad (1.2)$$

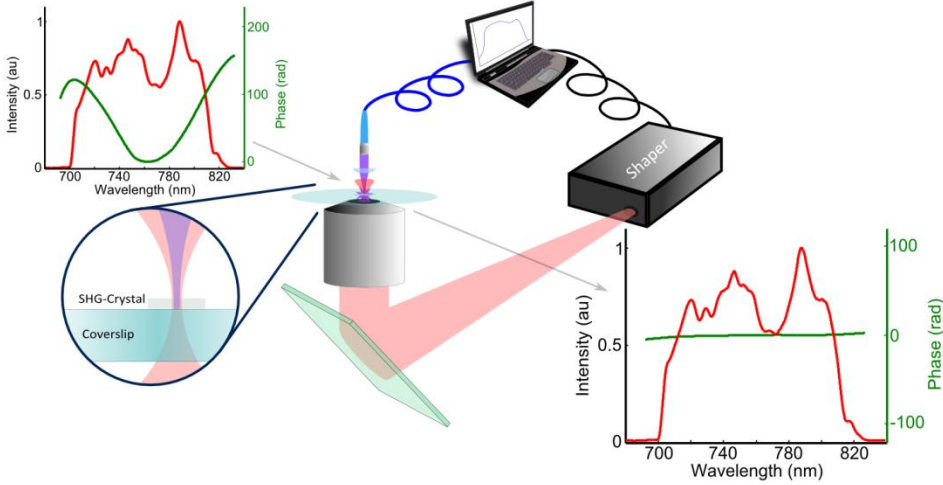


Figure 1.2: **Schematic sketch of the MIIPS procedure.** An ultrafast pulse with a random spectrum phase is focused into a micrometric sliver of BBO crystal; the resulting second harmonic spectrum is modulated by adding a series of well-known phases in the shaper. This allows for calculation of the unknown spectral phase, which can be subtracted from the pulse in the shaper, leading to a spectral phase that is flat for all practical purposes and a fourier limited pulse in the focal plane of the experiment.

To this end, we employ the MIIPS (Multiphoton Intrapulse Interference Phasescan) method<sup>32–40</sup>. Developed in the lab of Markus Dantus, this method utilizes  $\varphi_{shaper}(\omega) = \alpha \sin(\beta[\omega - \omega_0] + \delta)$ . What follows is an explanation of the calibration process adapted from refs<sup>32–34</sup>.

The sine function has two well-defined points per period where the second order derivative is 0, namely in the zero crossings. By varying the frequency offset  $\delta$ , this zero crossing is scanned through the spectrum. Appropriate tuning of  $\beta$  ensures that for a scan of  $\delta$  from 0 to  $2\pi$ , both zero-crossings traverse the spectrum once, giving a double measurement. Keeping in mind that for a Gaussian pulse the relation between pulse length and spectral width is given by  $\tau f = 0.44$  this can in good approximation be done by letting  $\beta$  approach the pulse length.

For a Fourier limited pulse, the SHG would be maximum at the frequency where the zero-crossing of the sine sits, i.e.

$$\varphi''_{shaper}(\omega, \delta_{max}) = -\alpha\beta^2 \cos[(\omega - \omega_0)\beta + \delta_{max}] = 0 \quad (1.3)$$

This means that the argument of the cosine has to be  $\pm\pi/2$ , which shows there is a linear relationship, with a periodicity of  $\pi$ , between the frequency and the value for  $\delta$  where twice this frequency gives a maximum SH signal.

When  $\varphi_{dispersion}(\omega) \neq 0$ , equation (1.2) now gives a method to determine  $\varphi_{dispersion}(\omega)$ ; the value for  $\delta$  where the Second Harmonic for a particular frequency reaches a maximum gives the second derivative of the phase at that frequency by

$$\varphi''_{dispersion}(\omega) - \alpha\beta^2 \cos([\omega - \omega_0]\beta + \delta_{max}) = 0 \quad (1.4)$$

Recording second harmonic spectra for  $0 < \delta < 2\pi$  allows the determination of  $\delta_{max}$  for each frequency, which gives the full second derivative of the spectral phase: this can be integrated twice to obtain the spectral phase, keeping in mind that zeroth and first order terms do not matter and can be set to 0 (Fig 1.3).

This method gives the best result when the second derivatives of the shaper phase and the dispersion have the same order of magnitude, since that will give the clearest deviation from a constant spectrum (when the shaper phase is negligible compared to the dispersion) or a linear relation between  $\delta$  and SHG maximum (when the dispersion is negligible compared to the shaper phase).

Given that the magnitude of the second derivative of the shaper phase depends on  $\alpha$  and  $\beta$ , but  $\beta$  is restricted by the pulse width,  $\alpha$  should be tuned for maximum accuracy of the method. It follows that the best way to compensate for the dispersion is to do MIIPS-runs with progressively better compensated dispersions, measured with progressively smaller  $\alpha$ 's in an iterative fashion. From the first iteration where  $\alpha$  is large enough to satisfy Equation 1.4 for a given  $\delta$  for any  $\omega$ , but not (too much) larger, it typically takes between 3 and 6 iterations more to compensate the phase to a level that the residual disappears in the experimental noise.

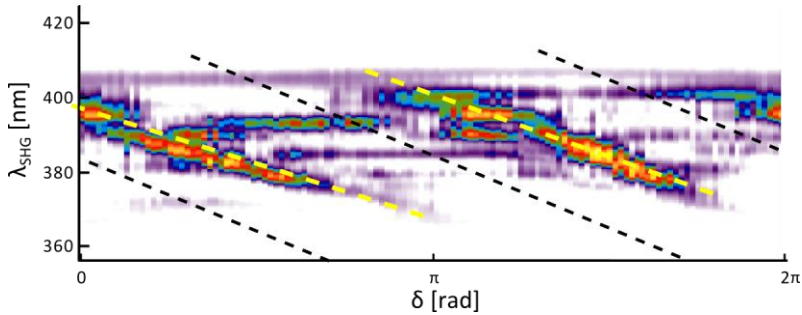


Figure 1.3: **Typical noisy MIIPS trace of a femtosecond pulse.** The result of a MIIPS-run typically looks like this; the black dotted lines are guides to the eyes indicating the slope with which the zero-crossings of the sines are shifted through the spectrum by varying delta; the two areas in between the 3 dotted black lines are the areas where the maximum of the SHG should shift between the highest and lowest wavelength in the spectrum. This gives intensity bands as indicated by the dashed yellow lines, that are a measure for  $\varphi''_{dispersion}(\omega)$ . The difference in slope between the two lines indicates that there is some quadratic chirp left in the pulse.

## 1.4 Ultrafast spectroscopy

For our experiments, it is important to distinguish two kinds of coherence: coherence in the exciton basis, and coherence in the site basis. As explained before, coherence in the exciton basis means induced coherence between eigenstates of a quantum system; coherence in the site basis means a delocalized wavefunction between spatially separate parts of molecular complexes.

In ultrafast spectroscopy, induced coherence in the exciton basis is measured<sup>41,42</sup>. Most of our measurements are based on phaselocked pump probe measurements that fit in this mold. In these schemes, a first pulse creates a coherence between a ground and an excited state, which the second pulse maps to a population. This is sufficient to probe coherence between ground and excited states (chapter 3) and to modify this by vibrational interactions (chapter 4). To probe coherence between 2 excited states, typically 2D spectroscopy is used: this is a massive field in itself, with myriad similar but slightly different techniques (2D photon echo spectroscopy, 2D infrared spectroscopy, 2D fourier transform infrared spectroscopy, 2D electronic spectroscopy, etc) that would require too much space to explain in detail: for this we point to Mukamel's standard work on nonlinear optical spectroscopy<sup>41</sup>.

Generally though the technique utilizes 3 pulses followed by a photon echo, or 4 pulses when a (coherent) photon echo is too weak and a stimulation pulse for a coherent or incoherent signal is needed, and depends therefore on the third order susceptibilities  $\chi^{(3)}$ . The general picture is that the first pulse creates a coherence between the ground state and a manifold of excited states. This coherence develops for a certain time under field free conditions, subject to coherence dephasing. The second pulse maps this coherence to populations in the various excited states (where different techniques variously look at the population of the excited state(s), the resultant coherences between the excited state(s) or the dumped back population in the ground state). This population or excited state coherence then develops again for some time under field free conditions, after which a third pulse interacts with the system, leading to a total of 4 possible different superposition states (i.e. where coherence plays a role) with 8 pathways leading there (provided all possible combinations of frequencies lead to accessible states). Typically one of these is pathway of interest, and the resulted state is then either creating an echo, allowed to collapse into populations followed by fluorescence, or stimulated to a signaling end-state.

At the single molecule level, the minimal absorption cross-section makes it hard to address higher order susceptibilities. For the experiments of chapter 3 and 4 we therefore only follow the 2D scheme outlined here up to the second pulse; this interaction depends upon the linear susceptibility (another way of looking at this that might make that clearer is to see that the interaction that creates the coherence is that with the first pulse, followed by the signaling probe pulse). In chapter 3, we approximate a single molecule as a fast dephasing two level system: the first pulse creates coherence between the ground and the excited state and the second pulse converts this to an excited state population,

which we read out in fluorescence<sup>43,44</sup>. In Chapter 4, we perform a degenerate experiment in that multiple vibrational levels can be excited by the same pulse and are probed by the same pulse; vibrational wavepacket oscillations thus modulate the coherence between the ground and the excited state.

In chapter 5 we also do a phaselocked pump-probe experiment, but we apply a trick: using a phase shaper, we can lock the relative carrier-envelope phase between two frequency bands in one pulse. This allows for the targeted investigation of two coupled quantum systems<sup>44</sup>. The first pulse creates a coherence between the ground and the excited state of the first quantum system; due to exciton delocalization this coherence is now shared between the two systems and can be probed (i.e. converted to a population) in the second quantum system. This gives information about the coupling between the systems, i.e. it allows us to probe coherence in the site basis, which matters for energy transfer even under excitation with incoherent light.

In chapter 6, we probe two-photon photoluminescence (TPPL) of gold antennas, which technically is proportional to  $\text{Im}[\chi^{(3)}]$ <sup>45</sup>. We again perform a pump-probe experiment, but this time not of molecular resonances and molecular dipoles, but of plasmonic resonances. We could still describe this in terms of ultrafast spectroscopy: the first pulse then excites the plasmonic resonance (“establishes the coherence”), and the second pulse interferes with the field in the hotspots creating a double-frequency resonance (“creates a higher order coherence”) which probes the strength of the fields in the hotspots. This leads to two-photon absorption (“coherence relaxes to population”), which is probed in fluorescence (TPPL).

However, since the description of processes in the 2D spectroscopy picture requires phase stability between the pulses, this process can also be described directly in the frequency domain: if for the entire pulsetrain the delays and phases are well-defined, this translates directly into an amplitude and phase-modulated-spectrum which can be used, analogous to Eq (1.1), to calculate the probability for multiphoton processes. This is a description that makes more sense in chapter 6.

## 1.5 Plasmonics

A plasmon is defined as a collective oscillation of free electrons, for example in a metal. At optical frequencies, the skin depth of metals is in the nanometer range and the plasmons that can interact with an optical field are confined to the surface of metal particles (broadly speaking: for nanometric particles, the plasmon can also exhibit a bulk characteristic). The field of plasmonics therefore mainly concerns itself with surface plasmons.

Plasmonics has gone through many revivals over the years; first predicted in 1957 by Ritchie<sup>46</sup>, it got renewed attention after the discovery of Ebbesen et al<sup>47</sup> of extraordinary transmission. Since that point, any effect of dimensions, geometry, material, quality, substrate, or configuration of plasmonics systems on any plasmonic phenomenon, i.e. field confinement, spectral properties, loss, coupling to emitters, transmission, absorption, guiding, scattering, etc. has been the subject of heavy investigation (see e.g. <sup>48-51</sup> and references therein). It goes

too far to treat the entire field of plasmonics here, mainly because this thesis only touches on it lightly, but some results of these past 15 years of research should be mentioned in this context.

First of all, surface plasmons exist on the interface between a dielectric and a metal and have an exponentially decaying strength with distance from this surface<sup>52,53</sup>. This makes plasmonics an extraordinarily promising field for high resolution microscopy, since excitation-fields could be confined to nanometric regions near metallic surfaces, so called hotspots (Fig. 1.4). This was the basis of the field of near-field optics<sup>54-57</sup>, where a sharp or small metallic structure, like a tip or particle, was scanned over a sample while being illuminated, and the field-enhancement at the sharp end of the structure allowed signal to be mainly excited in the nanometric volume of the near field around the structure.

Second, the resonances of plasmonic particles depend straightforwardly on their dimensions<sup>58,59</sup>. It was realized that rod-like structures especially allowed for easy tuning of the plasmon resonance<sup>60</sup>, as well as a strong polarization sensitivity of the resonance excitation<sup>61</sup>(Fig 1.4). The discovery that plasmonic rods could be coupled to emitters and function as antennas to mediate the coupling between far field radiation and near field systems has led to a recasting of a lot of plasmonics research in terms of antennas<sup>62,63</sup>; to this day the question whether a plasmonic particle is a cavity (albeit a lossy one) or an antenna can still elicit heavy discussion among plasmonic physicists.

Finally, plasmonic antennas are resonators, which can be coupled together just like any other oscillator; the coupling will modify their properties<sup>64,65</sup>. Plasmonics is inherently broadband: there are no sharp resonances in either the dispersion diagrams of surface plasmons, nor in the spectra of plasmonic particles<sup>66-68</sup>. Fano-resonances (interactions of sharp resonances with a continuum leading to sharp dip in resonance strength) have gained a lot of attention recently<sup>51</sup> but even here, sharp is a relative notion. Plasmonics generally supports femtosecond pulses<sup>53,67,69</sup>.

We will use these properties in the experiments in chapter 6.

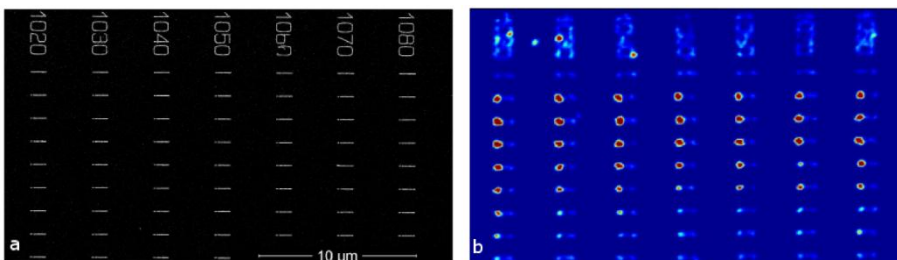


Figure 1.4: **SEM-image and corresponding TPPL image of plasmonic antennas.** a) The SEM-image displays coupled plasmonic antennas (two antennas with a gap in between) with varying lengths, denoted by the markers, and gaps that shift 10 nm from left to right for every row. b) The corresponding TPPL image shows the strength of the hotspots on each antenna.

## 1.6 Conclusions

In order to investigate the ultrafast quantumdynamics of complex molecular systems at room temperature, it is necessary to observe single molecules at femtosecond timescales with a phase sensitive method. Doing this will allow to investigate the influence of the specific nano-environment of the molecule on its dynamics, will lead to quantum tomography in complex molecular systems and allow for investigating the physical properties that determine the evolved functionality of biomolecules.

We build on concepts from single molecule detection, pulseshaping, ultrafast spectroscopy and plasmonics to reach this regime. The next chapters in the thesis will elaborate on the themes introduced here.

In chapter 2, we threat the experimental developments needed to do an ultrafast experiment at the single molecule level. In chapters 3 and 4 we show we can induce, probe and manipulate coherent superposition states in single organic molecules. In chapter 5 we apply the techniques developed in the previous chapter to investigate long lived coherence in light harvesting complexes. In chapter 6, we engineer a plasmonic technique that allows for the spatial resolution and temporal flexibility to investigate supramolecular systems with single molecule resolution.



**In this chapter, we argue that diffraction of finite sized laser beams limits the degree of control that can traditionally be exerted over ultrafast pulses. This limit manifests as spatio-temporal coupling induced in standard implementations of pulse shaping schemes. We demonstrate the influence this has on coherent control experiments that depend on finite excitation, sample, and detection volumes. Based on solutions used in pulse stretching experiments, we introduce a double-pass scheme that reduces the errors produced through spatio-temporal coupling by at least one order of magnitude. Finally, employing single molecules as nanoscale probes, we prove that such a double pass scheme is capable of artifact-free pulse shaping at dimensions two orders of magnitude smaller than the diffraction limit and employ this scheme in a variety of proof of principle experiments.**

**2. Beating spatio-temporal coupling:  
implications for pulse shaping and  
coherent control experiments**

## 2.1 Introduction

Many experiments in physics<sup>70–73</sup>, chemistry<sup>35,74,75</sup>, communication technology<sup>76–78</sup>, and quantum information technology<sup>79,80</sup> make use of shaped ultrafast laser pulses, e.g. for addressing dynamic processes in molecules<sup>81–86</sup>, to optimize contrast in stimulated emission<sup>9</sup> or Raman spectroscopy<sup>87,88</sup> and to enhance stability and output power in pulse amplification<sup>89</sup>, parametric conversion<sup>90</sup>, and supercontinuum generation<sup>91,92</sup>. Compensation of acquired second and third order dispersion can be accomplished with pulse stretchers and compressors based on prisms<sup>93</sup>, gratings<sup>94,95</sup> or chirped mirrors<sup>96</sup>, but for higher order or non-polynomial phase compensation these do not suffice. Moreover, experiments with few-femtosecond pulses often require sculpting the spectral amplitude<sup>71,72</sup> or polarization<sup>97,98</sup>. For these more intricate pulse-shaping actions, more advanced shapers that can address individual bands in the spectrum with high resolution are necessary.

The two most used pulse shaping techniques are based on Liquid-Crystal (LC) Spatial Light Modulators (SLMs) integrated in a 4f-configuration<sup>28–31</sup> and on Acousto-Optic Programmable Dispersive Filters (AOPDFs)<sup>24–26,99–101</sup>.

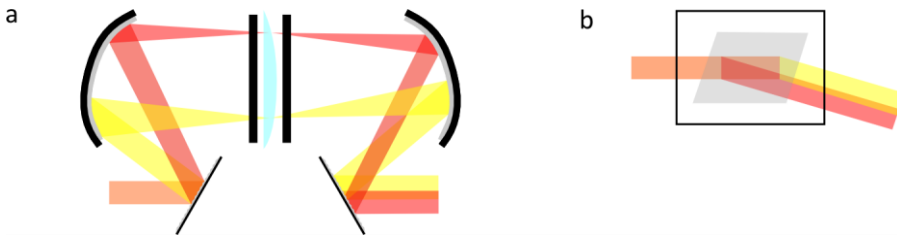


Figure 2.1: **The standard single-pass configurations of pulse shapers.** a) Based on Spatial Light Modulators (SLM). b) Based on Acousto-Optic Programmable Dispersive Filters (AOPDF). In both cases, different phase shifts applied to different spectral components will cause a spatial displacement in the output beam; this is called spatio-temporal coupling.

In Fig. 2.1a a sketch of a 4f-shaper based on a LC SLM is shown. The frequency components of a laser pulse are dispersed spatially by a diffraction grating and then focused on an LC-array that is placed in the Fourier plane. Each pixel in the LC-array is a birefringent element, the optical length of which can be adjusted by applying a voltage, thus creating a spectrally dependent phase function. Simultaneous application of an extra mask can create a spectrally dependent polarization, since the change in optical length is accompanied by a gradual variation of the polarization state of the light passing through the pixel. After the LC the light is recollimated and the frequency components are recombined on a second grating to form the output pulse. A

polarizer after the shaper projects the spectral polarization function into an amplitude modulation if desired.

In AOPDFs (Fig. 2.1b) laser pulses are shaped by interaction with an acoustic pulse in a birefringent crystal<sup>101</sup>. The phase matching requirement for efficient acousto-optic interaction leads to control of the position in the crystal where the optical and acoustic pulses interact, through dispersion of the acoustic spectrum. The amplitude and phase modulations of the acoustic spectrum are in this way imprinted on the optical spectrum<sup>24,25</sup>.

Pulse shaping is generally performed in a single-pass configuration<sup>9,24–26,28–31,35,70–72,74–78,81,82,87–92,97–100</sup> (Figs. 2.1a and 2.1b). In this context, we define ‘single pass’ as one complete passage of a pulse through a shaper, that is, in AOPDF-based shapers one pass through the crystal, and in SLM-based 4f-shapers one sequence of dispersion, focusing, shaping, collimation, and frequency recombination.

This chapter discusses the nature and magnitude of spatio-temporal coupling induced by single-pass shaping<sup>102–104</sup>, shows its adverse effect on typical coherent control experiments and presents solutions, most importantly in the form of a double pass through a pulse shaper. As examples, measurements both in the single pass and the double pass configuration are presented.

## 2.2 Experimental method

The spatio-temporal coupling induced in shaped laser pulses was studied in detail using nanoparticles and single molecules as local field probes; these were also employed in proof of principle experiments showing nanoscale coherent control free of spatiotemporal coupling.

The effect of spatiotemporal coupling is shown on gold nanoparticles in the linear, single photon excitation limit, where, due to the wide absorption band of gold, no intrinsic material effect is expected. For the solution based on double pass shaping we show the difference in response from a gold particle and a single molecule; we show the response of a single molecule at different positions in a pulsed, diffraction limited focus; and the ability to do a pulse compression measurement using a nanometer shaped BBO crystal. These measurements demonstrate that the double pass scheme has the sensitivity, selectivity and focal uniformity to perform nanoscale coherent control experiments.

Shaped and pre-compensated pulses were directed into a confocal microscope and focused with a 1.3 NA objective (Fluar, Zeiss) onto a thin microscope cover slip containing a sample layer with a few nanometer thickness. The full-width at half maximum of the focus ranged from 250 to 300 nm depending on the experiment. The signal recorded from the sample was the single photon excited fluorescence for gold and molecules, and the Second Harmonic for the BBO nanocrystals. The signal was separated from the excitation light using suitable dichroic beam splitters and filters, and detected by an avalanche photodiode (APDs, Perkin Elmer, SPCM-AQR-14). The excitation power was simultaneously recorded with a photodiode at the sample position

and was typically in the range of a few  $\mu\text{W}$ . The sample position is controlled with a precision of about 1 nm using a closed-loop piezo stage (Mad City Labs).

A measurement started with scanning the sample to image the emission intensity as a function of position. This allows for localization of nanoparticles or single molecules in the sample, which are consecutively brought into the focus of the excitation beam. The signal is then recorded as function of the position and the applied pulse shape.

We used two setups. In the first, the pulses were produced by an optical parametric oscillator (OPO, Automatic PP, APE, pumped by a Titanium:Sapphire-system, Mira, Coherent). The resulting pulse train was passed through a pulse picker (PulseSelect, APE) to reduce the repetition rate from 76 MHz to effectively 1.25 MHz (bunches of pulses with a repetition rate of 25 kHz, repetition rate within bunches: 10 MHz). The pulses in this experiment were shaped with an acousto-optic programmable dispersive filter (AOPDF, Dazzler, Fastlite). This shaper was used for dispersion compensation, to provide transform limited pulses with 50 fs duration at the sample plane, as well as for shaping to generate pulse sequences with a well defined delay time and relative phase. This shaped beam was inspected by direct imaging onto a CCD camera (Andor).

In the second setup, the pulses were provided in an 85 MHz pulse train by a broadband Titanium Sapphire laser (Octavius 85 M, Menlo Systems) that was tuned to a center wavelength of 676 nm. The resulting pulses had a spectral bandwidth of 120 nm and were compressed to 14 fs in the sample plane. For dispersion compensation and shaping a 4f-shaper based on a double-pass spatial light modulator was used (adapted from MIIPS-box, Biophotonics Solutions Inc).

### **2.3 Experimental quantification of spatio-temporal coupling**

Adding spectral phase to a pulse in a single pass shaper spatially disperses the frequency components of the output pulse as sketched in Fig. 2.1. A 4f-shaper theoretically forms an ideal telescope with a magnification of one. The spot of the incoming beam on the first grating can be viewed as an object that will be imaged perfectly on the second grating. An SLM with a phase function applied can be viewed as a discretized cylindrical Fresnel lens; when placed in the Fourier plane of the shaper it will modify the imaging properties of the telescope. As a result, the "image" will be magnified along the shaping direction on the second grating. Since the light is diffracted by the first grating, with an angle proportional to the wavelength, the magnified image will additionally exhibit a spatial dispersion of wavelengths equal to the "magnification" introduced by the lensing action of the phase mask applied on the SLM.

In an AOPDF, the laser pulse propagates through a chirped Bragg grating, created by the applied acoustic pulse, which refracts different wavelengths at different positions in the crystal. Because of the phase matching condition, the acoustic wave is launched with a  $k$ -vector non-collinear to that of the laser

beam; the outgoing laser beam therefore has a modified propagation direction according to  $k_{\text{out}}=k_{\text{in}}+k_{\text{acc}}$ <sup>26</sup>. This change of direction at different points in the crystal for different wavelengths causes a spatial chirp accompanied by a broadening of the beam profile<sup>105</sup>.

The spatio-temporal coupling created by these shaping processes has two main negative consequences. First, the non-ideal recombination of frequencies after the shaping action puts a limit on the spectral bandwidth available at each spatial coordinate in the laser beam<sup>106</sup>. It is therefore impossible to compress a pulse to the theoretical Fourier limit, which reduces temporal resolution and peak power available in experiments. Second, simultaneous application of a spectral amplitude modulation and a phase modulation will cause an additional spatial modulation of the intensity across the beam profile<sup>100</sup>. This is illustrated with the beam images shown in Fig. 2.2, corresponding to a pulse with a 30 nm spectral bandwidth shaped in an AOPDF. The shaping action consists of a  $-36000 \text{ fs}^2$  phase mask for dispersion compensation and an additional cosinusoidal (Fig. 2.2a) or sinusoidal (Fig. 2.2b) amplitude modulation to create two pulses with 100 fs delay and 0 or  $\pi$  mutual phase difference, respectively. The difference between the two profiles (Fig. 2.2c) clearly reveals regular spatial intensity variations across the beam of up to 30%, caused by the spectral amplitude modulation.

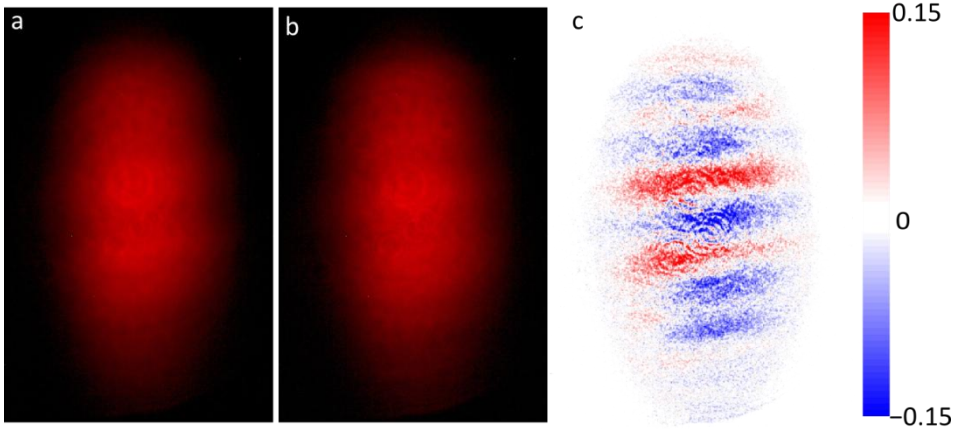


Figure 2.2: **Spatial effect of pulseshaping.** a-b) Spatial profiles of a laser beam with 20 nm spectral bandwidth after passing through a single-pass AOPDF-based shaper. A cosinusoidal (a) and sinusoidal (b) amplitude modulation is applied on top of a  $-36000 \text{ fs}^2$  compensation phase to create two phase-locked pulses with 0 and  $\pi$  phase difference, respectively, and 100 fs delay time. c) The difference between the images in a and b reveals clear spatial intensity modulations of up to 30% of the local intensity.

A spectrally and therefore spatially modulated beam will be focused differently according to the Fourier principle. Coherent control experiments are generally influenced by this effect, because of their dependence on the overlap of three volumes: The excitation volume, the sample volume, and the detection volume. The excitation volume is defined by the focal volume of a shaped pump beam. The detection volume is given by the focal volume of a probe beam or the projection of a detector-area into the sample. The sample volume is the space occupied by the system under investigation.

In bulk experiments in liquids or solids, where the sample is uniform, the sample volume is irrelevant as long as it is larger than the excitation and detection volumes in every dimension. However, in experiments on non-uniform samples the effective sample volume becomes important, as it is determined by the spatial distribution of the sample unit under investigation (e.g. molecular beams, single molecules<sup>85,86</sup>, nanoparticles<sup>98</sup>, quantum dots<sup>107</sup>). A changing position of the excitation volume as a function of temporal pulse shape, will cause a varying overlap with finite sized detection and sample volumes and result in a varying signal irrespective of any temporal dynamics in the sample.

An example of effects produced by spatio-temporal coupling and limited sample, excitation and detection volumes is shown in Fig. 2.3, which presents the results of a degenerate pump-probe experiment on gold nanoparticles (see experimental section). The roughly spherical particles with a diameter of 100 nm define the sample volume; the pump focus is nominally  $\sim 250$  nm FWHM along the smallest dimension but is elongated due to the elliptical profile of the shaped excitation beam. The imaged detector area is about  $2 \mu\text{m}$ , and the centers of the pump and detection volumes overlap. The sample is scanned through those volumes to obtain an image as shown in Fig. 2.3a. (Convolution of the particle size with the excitation volume determines the spot sizes in the image.) A nano-particle is then placed at different positions in the pump focus and excited with two phase-locked pulses generated by the AOPDF (see above) with a sinusoidal amplitude modulation of the pulse spectrum applied on top of a phase modulation to compensate for  $36000 \text{ fs}^2$  dispersion of the setup. The inter-pulse delay is varied from 0 to 300 fs and the phase between the pulses is locked at 0 rad.

We chose 100 nm gold particles for this experiment because they are comparable in size to the focus and therefore show that artifacts do not only play a role on scales very much smaller than the focal volume (i.e. the excitation volume). In addition, since the signals are linear with excitation power and the absorption spectrum of the gold particles is much broader than the pulse bandwidth, no signal change as a function of temporal pulse shape is expected. However, as shown in Fig. 2.3b, the signal of the nanoparticles presents strong variations as a function of the applied pulse shape. Moreover, the result of the experiment varies dramatically depending on the position of the gold particle in the focus, with the largest difference occurring between the particle in the top and bottom side of the focus (red and magenta curves).

This is a consequence of two effects: i) a variation of the beam width, and ii) changes in the symmetry of the beam profile. At short delays the application of

the spectral amplitude-mask has, through spatio-temporal coupling, the effect of a “breathing” of the beam width, with the beam first getting narrower and then wider with increasing delays. This means the excitation focus will get wider and subsequently narrower with delay<sup>108</sup>. Depending on the position of the particle, this causes a better or worse overlap of the excitation volume with the gold particle, which results in higher or lower signals for particular delays depending on the particle position, as Fig. 2.3 shows. In addition the exact shape of the spectrum is important, as an asymmetric spectrum will cause an asymmetric beam profile after single pass shaping, which will thus be focused lopsided. Introducing a spectral amplitude modulation will therefore cause translational motions of the excitation volume on top of the breathing of the focal size.

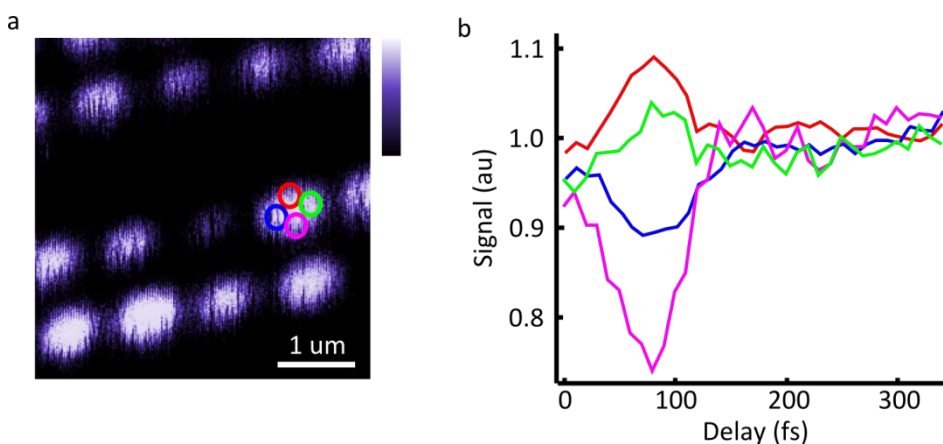


Figure 2.3: **Spatio-temporal coupling in coherent control experiments.** a) 5x5 μm<sup>2</sup> scan of a sample of regularly arranged gold-nanoparticles with a diameter of 100 nm. The emission intensity is color coded with high signal indicated by white. b) Normalized photoluminescence as a function of inter-pulse delay at constant phase difference for a single Au-particle placed at different positions in the excitation focus, indicated by the colored circles in a). Here, the pulse sequences were created with a single-pass AOPDF.

This variation of position and size of the excitation volume with the pulse shape, as illustrated in Fig. 2.3, can have profound influence on coherent control experiments. The changing overlap between excitation, sample and detection volume leads to artificial signal fluctuations as a function of applied pulse shape, which can steer the outcome of optimization routines in coherent control experiments towards undesired target states. Moreover, after an optimization routine influenced by this artifact, an examination of pulses perceived as optimized to achieving a particular target state will lead to incorrect deductions about the molecular energy landscapes involved.

Spatio-temporal coupling is the natural result of optical transformations fundamentally limited by diffraction. Spatial shifts of finite-sized beams cause the coupling between space and time in AOPDFs; diffraction of finite-sized beams is its source in 4f-shapers; diffraction limited propagation and focusing cause a finite excitation volume, preventing ideal spatial and temporal recombination of the resulting pulse in a sample.

The spatial effects of spatio-temporal coupling influence each type of pulse shaping experiment differently: in principle, they could cancel out when both sample and detection volume are uniform and larger than any spatial change in the excitation beam, for example when using detectors with a projected area significantly larger than the pump focus in a uniform sample. This cancelling however, is not possible in the case of experiments utilizing probe beams for signal read-out, due to the non-uniform spatial nature of beam foci, and therefore of the detection volume. Experiments on structured samples, e.g. single molecules, nanostructures, quantum dots, and biological structures such as membranes or cells, by their very nature do not have a uniform sample volume and will therefore be influenced by this effect independent of the detection method.

Furthermore, this relaxing of the experimental conditions does not hold for experiments involving nonlinear process, because the excitation power density does vary locally, which will change the overall outcome of multiphoton process even when integrated spatially. Finally, the temporal effect of spatio-temporal coupling, i.e. the limit imposed on time resolution by non-ideal frequency recombination and the smaller effective bandwidth utilized, cannot be overcome this way. To achieve this, the spatio-temporal coupling needs to be canceled in the shaping process itself.

### **2.4 Fourier analysis of spatio-temporal coupling in 4f – pulse shapers**

To gain a more detailed understanding of the way a shaper induces spatio-temporal coupling we performed a Fourier analysis of the passage of a pulse through a single-pass 4f-shaper.

We note that space-time coupling in shapers is often treated in terms of pixilation effects in SLMs<sup>109,110</sup>. This chapter aims to show that even in an ideal, non-pixilated shaper spatio-temporal coupling is a source of artifacts. As the effect of full and limited pixilation in LC-arrays has been investigated elsewhere<sup>109,110</sup>, we focus here on the purely geometrical effects induced in a 4f-shaper. We therefore represent the pulse spectrum as well as the phase and amplitude modulations as continuous in frequency space.

The laser pulse is modeled with a Gaussian spatial cross-section and a Gaussian spectral profile in the x-z-plane propagating along the z-direction. The dispersion on the grating as well as the shaping action is along the x-coordinate. As the action of the focusing elements is equal along x and y, and the beam is propagated as a Gaussian in both x and y, the laser pulse is described as a 2-

dimensional Gaussian in  $x-\omega$  or  $x-\lambda$  space. The beam undergoes the following transformations<sup>109,111,112</sup>:

1. Dispersion on the first grating according to

$$E_1(x, \omega) = \sqrt{\beta} E_m(\beta x, \omega) \exp[i\gamma(\omega - \omega_0)x] \quad (2.1)$$

with  $\beta = \cos \theta_i / \cos \theta_d$ ,  $\theta_{i(d)}$  being the angle of incidence (diffraction) of the central frequency  $\omega_0$  on the grating; and  $\gamma = 2\pi(d\omega_0 \cos \theta_d)^{-1}$ , with  $d$  being the line spacing of the grating.

2. Propagation from the grating to the first focusing element according to

$$E_2(k, \omega) = E_1(k, \omega) \exp\left[\frac{-ik^2 f \lambda_0}{4\pi}\right] \quad (2.2)$$

where  $E_1(k, \omega)$  represents the spatial Fourier transform of  $E_1(x, \omega)$ ,  $f$  denotes the focal length of the focusing elements, which is the propagation distance from the grating to the first focusing element, and  $k = 2\pi / x$ ;

3. Focusing of the beam according to

$$E_3(x, \omega) = E_2(x, \omega) \exp\left[\frac{-i\pi x^2}{f \lambda_0}\right] \quad (2.3)$$

4. Propagation from the focusing element to the shaping plane over a distance of  $f$  according to (2.2)
5. Shaping action according to

$$E_5(x, \omega) = E_4(x, \omega) T_{mask}(x) \quad (2.4)$$

with  $T_{mask}(x)$  being a complex function  $A(x)e^{i\phi(x)}$  for amplitude and phase shaping;

6. Propagation from the shaping plane to the second focusing element according to (2.2);
7. Collimation according to (2.3);
8. Propagation from the focusing element to the second grating according to (2.2);
9. Recombination according to

$$E_9(x, \omega) = \sqrt{1/\beta} E_8(x/\beta, \omega) \exp[i\gamma(\omega - \omega_0)x/\beta] \quad (2.5)$$

10. Propagation out of the shaper according to (2.2).

The output field after a single-pass shaper can thus be written as

$$E_{out}(k, \omega) = E_{in}(k, \omega) T_{single}(k, \omega) \quad (2.6)$$

with

$$T_{single}(k, \omega) = T_{mask} \left( -\frac{\gamma(\omega - \omega_0) - \beta k}{2\pi} \lambda_0 f \right) \quad (2.7)$$

Here  $T_{mask}(x)$  is the spatial shaping function as defined in transformation (5). The  $(k, \omega)$ -content of each  $x$ -coordinate is determined by  $\beta$  and  $\gamma$ ;  $\beta k$  gives the spatial dispersion induced by the part of the  $k$ -space occupied by the beam;  $\gamma(\omega - \omega_0)$  represents the dispersion induced by the grating.

In the shaping plane a negative quadratic dispersion is added to the pulse to pre-compensate dispersion by optical elements. Since quadratic dispersion through spatial phase application effectively creates a lens,  $T_{mask}$  can be expressed as  $T_{mask} = \exp\left[\frac{-i\omega_0 x^2}{2cl_m}\right]$ , where  $l_m$  is the equivalent focal length of the applied quadratic phase mask.

As the coordinate transformation  $x \rightarrow -\frac{\gamma(\omega - \omega_0) - \beta k}{2\pi} \lambda_0 f$  yields a  $T_{single}$  with a cross term between  $k$  and  $\omega$ , it follows that there is a coupling between the dominant wavelength and the  $x$ -coordinate in the beam.

This analysis is illustrated in the top row of Fig. 2.4, which shows the simulation of a single-pass shaper for an initial Gaussian spectral and spatial profile of the beam in  $x$ - and  $\lambda$ -dimension (Fig. 2.4a) with a beam diameter of 2 mm (FWHM) and a spectral bandwidth of 20 nm (0.06 rad/fs) centered at  $\lambda_0 = 800\text{nm}$ . In this example an amplitude modulation is applied to create phase-locked pulses with 50 fs delay and 0 phase shift (Fig. 2.4b) and 50 fs delay and  $\pi$  phase difference (Fig. 2.4c), and simultaneously,  $-25000\text{ fs}^2$  dispersion is added to this amplitude mask. The value of  $-25000\text{ fs}^2$  is in the range of what is typically needed to compensate for passage through several optical elements and an objective. Although the pulses have the desired spectral characteristics if integrated over the entire spatial profile (Fig. 2.4b,c, red and blue curves), the 2D plots demonstrate that their spectral content varies significantly over the beam profile. Moreover, their spatial intensity profile differs from that of the unshaped beam (Fig. 2.4d). Both the broadening of the beam due to the spatio-temporal coupling as well as the spatial intensity modulation resulting from the applied spectral amplitude modulation is clearly visible (see also the experimental data in Fig. 2.2).

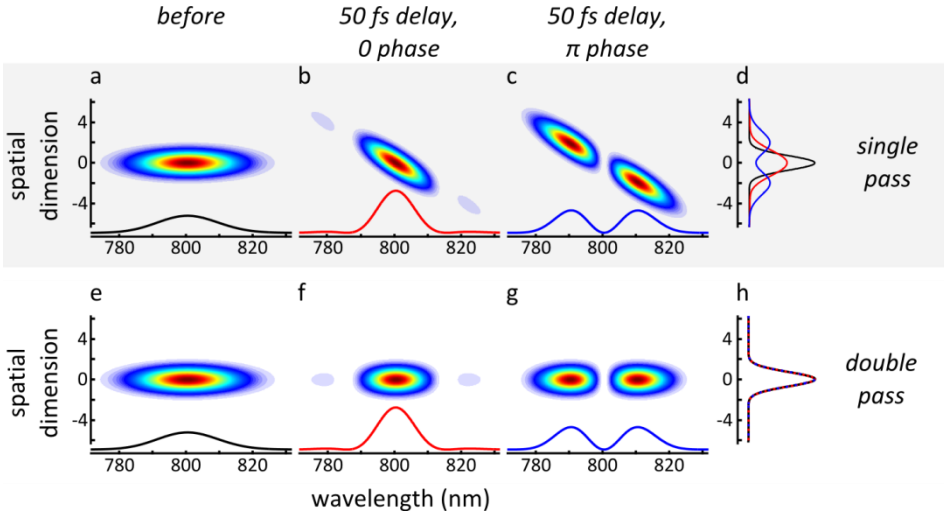


Figure 2.4: **Spatio-Temporal Coupling illustrated in Fourier space.** A laser beam with Gaussian spatial and spectral profile is propagated through a single-pass (top row, a-d) and a double-pass 4f-pulse shaper (bottom row, e-h), respectively. For both shaper configurations a quadratic phase mask is applied to compensate for  $25000 \text{ fs}^2$  dispersion and an additional amplitude mask is imprinted to create a phase-locked pulse pair with 50 fs delay and 0 ( $\pi$ ) rad relative phase. The intensity profiles of the beam are shown in a wavelength-space ( $\lambda-x$ ) frame (a-c and e-g), together with the integrated spectral intensity below each profile for the incoming (a,e, black curve), 0 phase (b,f, red curve), and  $\pi$  phase shaped beam (c,g, blue curve). The corresponding integrated spatial intensity profiles are depicted in the rightmost panel (d,h).

## 2.5 Reduction and compensation of spatio-temporal coupling

Diffraction being the limiting factor in obtaining correct pulse shapes suggests that relaxing the requirements for complete overlap of all spectral and spatial components of the beam can function as a patch solution to reduce the effects caused by spatio-temporal coupling. For certain classes of experiments this can be accomplished by scanning sample and detector area through the pump beam and averaging the signal over the entire pump area, effectively making them uniform in the excitation volume<sup>85</sup>. Another approach is manipulation the pulse beyond far field optical transformations, i.e. using near field optics<sup>113,114</sup> or spatial filtering<sup>85,86,115</sup> to force a particular spatial mode on the pulse.

While in principle allowing for cleaned up coherent control experiments, these solutions are not ideal. Instead of canceling out the effects spatio-temporal coupling causes, this approach only reduces their magnitude, and therefore has to be adapted to and checked before each experiment. Whether the residual

effects will be negligible compared to the actual signal depends on the experiment. Especially for coherent control experiments utilizing optimization routines based on genetic algorithms, it is virtually impossible to estimate beforehand whether the artifact level will have been reduced enough. It is equally hard to disentangle the artifact from an actual temporal effect in hindsight. Moreover, these solutions do not lift the limit spatio-temporal coupling imposes on the spectral bandwidth in the output pulse.

An ideal solution would result in a beam that: i) exhibits no spatio-temporal coupling after shaping independently of the specific shaping action, ii) utilizes the full bandwidth and all available power in the beam, and iii) is applicable in any experiment. Hence, the spatial part of the optical transformations that causes the spatio-temporal coupling should be reversed, without losing the temporal transformations on the pulse to be shaped.

High power, ultrafast laser and parametric amplification experiments suffered from a similar problem with pulse stretchers and compressors based on prisms and gratings. Passage through two prisms or gratings for stretching or compression purposes will result in collimated beams at the output, but any temporal stretching or compression of the pulse will cause a spatial dispersion of frequencies in the output beam. Especially pulse stretchers are direct precursors of the common 4f-shaper. It was realized long ago that stretching pulses in a single pass configuration would not allow the pulse to be recompressed to the theoretical Fourier limit. An elegant solution was found by Martinez and others: placing a mirror at the end of the beam path and sending the pulses back through the stretcher. This arrangement gives the pulse double the stretching in the temporal domain and cancels out the spatial dispersion<sup>95,108,116</sup>. In the following we analyze this double-pass approach theoretically and describe its application to a 4f-shaper.

## 2.6 Fourier analysis of spatio-temporal coupling in the double pass scheme

In the simulation of a double-pass shaper the pulse undergoes transformations 1-10 followed by a mirror transformation, after which it goes through transformations 1-10 again. Applied to  $E_m(k, \omega)$ , the transformation of the second pass is inverted in k-space compared to the transformation of the first pass due to the telescoping action of the first pass through the shaper. It can therefore readily be seen that the total output of a double pass shaping action is

$$E_{out}(k, \omega) = E_{in}(k, \omega) T_{double}(k, \omega) \quad (2.8)$$

with

$$T_{double}(k, \omega) = T_{mask}\left(-\frac{\gamma(\omega - \omega_0) - \beta k}{2\pi} \lambda_0 f\right) T_{mask}\left(-\frac{\gamma(\omega - \omega_0) + \beta k}{2\pi} \lambda_0 f\right) \quad (2.9)$$

In order to directly compare the single- and double-pass configurations,  $T_{mask}$  is adapted. In the latter scheme the pulse passes through the shaper twice, so the amplitude modulation is changed to its square root, and the applied phase is halved. The result after a forward and backward pass is a pulse with identical spectral amplitude modulations (Fig. 2.4f, g and insets) as compared with the single-pass configuration (Fig. 2.4b,c and insets). As can be seen from the 2D figures, however, the coupling between the spatial and spectral coordinates is absent and every point in the beam has the same spectral content. As a result, the output beam possesses the same Gaussian spatial profile as the input beam independent of the pulse shape (Fig. 2.4h).

Spatio-temporal coupling in pulse shapers has been analyzed before both experimentally and theoretically<sup>31</sup>. An influential theoretical comparison between the performance of the double-pass and single-pass shaper has been performed by Wefers and Nelson<sup>112,117</sup>, where the output of a double pass shaper is effectively defined by the same formula as (2.9). However, the sign inversion between  $-\beta k$  and  $+\beta k$  in the first and second pass was given as reason for not applying a double pass implementation as it implies an asymmetry between the forward and backward paths through the shaper and therefore a sustained spatio-temporal coupling. The double pass configuration is subsequently dismissed as apparently not reversing the spatio-temporal coupling, but instead creating a more complicated coupling between spectral and spatial content of the shaped beam.

In the context of this chapter, and the entire thesis, it is worth taking another look at this reasoning with an eye on modern equipment. Through the  $x \rightarrow -\frac{\gamma(\omega - \omega_0) \pm \beta k}{2\pi} \lambda_0 f$  coordinate transformation the  $\beta k$  term propagates as an error on  $\gamma(\omega - \omega_0)$  in the  $T_{mask}(x)$  function. Any continuous mask function can be written as a summation of Fourier components, which in turn can be expanded in a summation over a collection of Taylor series. In the double-pass shaper, the error  $\beta k$  is perfectly canceled in first and second order terms of a Taylor expansion. This means that Eq. (2.9) becomes separable and the spatio-temporal coupling is completely reversed for first and second order polynomial masks. In higher order masks, the error propagates no larger than  $O([\beta k]^2)$ , which is in stark contrast to the shaping in single pass, where the error always propagates as  $O(\beta k)$  or larger if a spectral phase is applied. The error caused by spatio-temporal coupling in double pass shaping is therefore either cancelled completely or at least one order of magnitude smaller than in the equivalent shaping action in a single pass configuration.

We note that the resultant uncoupling does not mean that a spectral amplitude shape is not influenced by the spatio-temporal coupling inside the confines of the shaper. Especially for higher order masks a correction can be necessary to create the desired spectral amplitude shape. This is possible if the amplitude is obtained with a spectral polarization rotation mask and after passage through the double-pass shaper a linear polarization is projected out. Because polarization and phase are uncoupled transformations and the polarization transformation is unitary (as opposed to a hard amplitude

transformation in the shaping plane, which will indeed produce more complicated and fundamentally uncorrectable shapes in a double pass configuration, as correctly pointed out by Wefers and Nelson), a polarization shape is influenced by the coupling between  $\omega$  and  $k$  in the same order as a phase shape. It follows that it is generally possible to define a desired continuous polarization shape as a function of  $\gamma(\omega - \omega_0)$  with error no larger than  $O([\beta k]^2)$ .

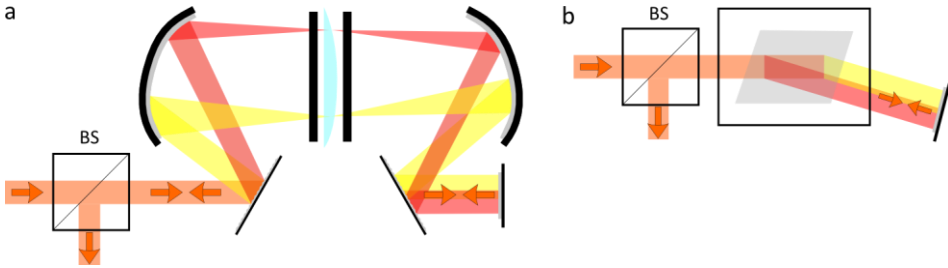


Figure 2.5: **Double-pass pulse shaping.** a) Based on SLMs. b) based on AOPDFs. The double pass is achieved by passing the beam through a beam splitter (BS) and putting a mirror at the output of the shaper.

The implementation of the double pass schemes are sketched in Fig. 2.5 for both the 4f- and AOPDF-based shaper. In the 4f-shaper this can simply be realized by placing a 50-50 beam splitter (BS) at the entrance of the shaper and a mirror at the exit. This will, however, result in a power loss of a factor of four. In order to increase the output power, the 50-50 beam splitter can be replaced by a polarizing beam splitter. Recalibration of the amplitude transformations ( $A$ ) in the LC-mask, according to  $A_{new}(\omega) = 1 - A_{old}(\omega)$ , will provide the correct amplitude modulation at the output. Alternatively, it is possible to insert a  $\lambda/4$  retardation plate at the output of the shaper, right before the mirror. Note that such schemes cannot be employed in shapers that are also meant to provide polarization shapes at the output. Another solution is to use the 3<sup>rd</sup> dimension, such that input and output beams are at different heights and no beam splitter at all is necessary.

Due to the small active area in AOPDFs and the dependence on the incoming polarization of the shaping action, such power optimization schemes cannot be employed. However, the basic double pass scheme with a 50-50 beam splitter and a mirror functions as well.

## 2.7 Experiments free of spatio-temporal coupling

We implemented the clean up and compensation of the pulses for both the narrow-band (OPO plus AOPDF) and broadband (Ti:Sapph plus 4f-shaper) setup. For the narrowband setup (OPO plus AOPDF), it turns out a sufficiently stringent spatial filter goes a long way towards cleaning up spatio-temporal coupling. This circumvents the alignment of the second pass through the AOPDF, which can be a daunting task since the output beam of the AOPDF tends to suffer from bad collimation. However, this comes at the expense of power loss (typically  $>98\%$  for sufficient cleanup) and, as stated before, the necessity to perform experiments in an iterative way, i.e. to check whether measured effects turn out to be sufficiently large that residual artificial effects due to spatio-temporal coupling can be neglected, and if necessary, to correct the level of cleaning.

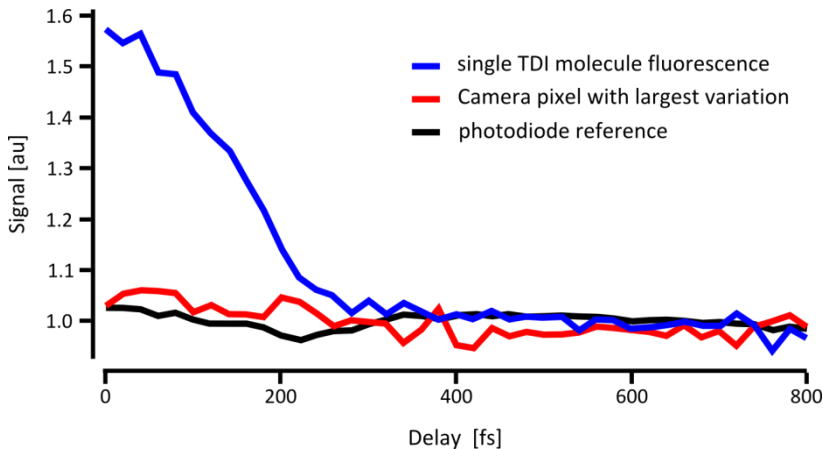


Figure 2.6: **Cleaned up pump probe comparison.** A pump probe experiment with a cleaned up beam was done focused through a 1.3 NA objective on a single TDI molecule (blue line), focused with a 10 cm lens on a CCD-camera (depicted is the pixel with the largest variation in intensity over the experiment, red line) and on a photodiode collecting the entire beam (black line).

An example is shown in Figure 2.6. A degenerate pump probe experiment was performed, where the output of the OPO was shaped with the AOPDF to give two pulses with variable delay and 0 relative phase difference. For the pump probe experiment, the delay was varied between 0 and 800 fs. Three experiments were compared. In a first reference experiment, the shaped pulse were recorded with a photodiode, which gave the overall variation in power for

each delay (Fig. 2.6, black line). This shows the power is basically constant for each shaped pulse pair. Then, the beam was imaged on a CCD camera for each delay, with a lens with 10 cm focal length. The intensity per pixel was traced; This gives a pump-probe experiment not an absolute high resolution, but relatively with detection areas about  $1/250^{\text{th}}$  of the focal area, i.e. with deep sub-focal resolution. Plotted is the delay line experiment for the pixel that showed the largest variation in signal as a function of delay, i.e. the largest difference between maximum and minimum intensity as a function of delay. It is clear that this trace follows the integrated intensity of the entire beam, i.e. there is no noticeable space-time coupling in the output beam that creates variations in the spatial distribution of intensity for different temporal distribution of intensity (i.e. delay). In contrast however, the experiment performed on a single TDI molecule (Fig. 2.6, blue line) shows a marked variation of signal as a function of delay. For this experiment, a single TDI molecule was positioned in the center of a focus created with a 1.3 NA objective, and the fluorescence as a function of delay was measured.

It is clear from this that the variation in signal from the TDI molecule is not related to spatio temporal coupling, but in fact due to the internal dynamics of the molecule. This was the first coherent control experiment, free of spatio-temporal artifacts, on a single quantum unit; in Chapter 3, the expansion of this measurement into a project on quantum coherence in single molecules will be described.

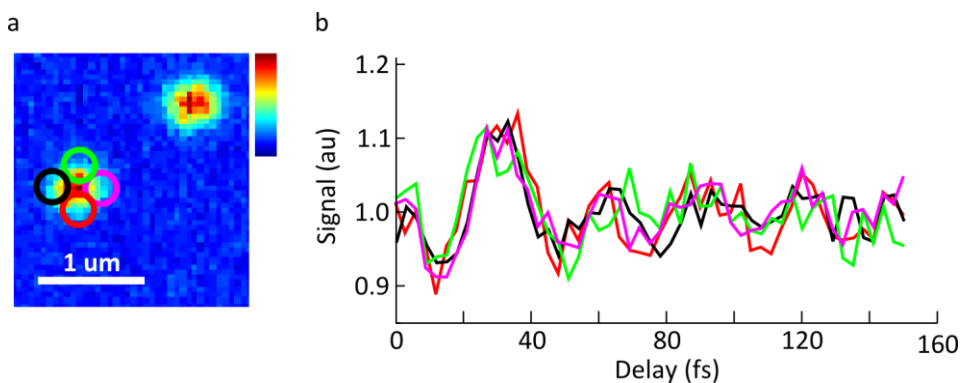


Figure 2.7: **A spatially resolved pump probe experiment on a single DNQDI molecule with a double pass 4f-shaper.** a) Scan of a sample containing single DNQDI molecules with a size of about 2 nm. The emission intensity is color coded from blue to red. b) Normalized fluorescence as a function of delay and constant phase difference between the excitation pulse pair for a single DNQDI molecule placed at different positions in the excitation focus indicated by the colored circles in a.

For the broadband setup (Ti:Sapph + 4f shaper), cleaning up the beam alone proved to be insufficient to obtain measurements free of spatio-temporal coupling. Apart from the clean up, the double pass scheme was therefore implemented here. To test the performance of the double-pass scheme with the highest resolution and sensitivity we could think of, we performed measurements analogous to those on gold nanoparticles, but using single fluorescent molecules instead. Employing single molecules to probe spatial variations of the field has the important advantage that they provide a much higher spatial resolution than gold particles. The fluorophores we used (the terrylene homologue DNQDI<sup>118</sup>) have a size, and thus provide a spatial resolution, of about 2 nm.

In this experiment, we employed pulses from the Octavius, shaped with a double-pass 4f shaper (see above). Through amplitude shaping on top of the pulse compression, we created a phase-locked double pulse. We varied the delay between the two pulses between 0 and 150 fs and kept the relative phase locked at 0 rad. As can be seen in the example of Fig. 2.7, the signal from a single molecule oscillates as a function of the delay between the two pulses. In contrast to the measurements using single-pass pulse shapers, repeating the measurement at different positions in the focus shows no changes in the signal. The same oscillatory behavior is observed for all positions, demonstrating that the field presents no spatial variations whatsoever. Rather than an artifact product of spatial field variations, this oscillatory trace is a signature of temporal molecular dynamics, visualized through vibrational wavepacket interference. In chapter 4 the expansion of this measurement into a project investigating the ultrafast dynamics and vibrational coherence in single molecules will be treated.<sup>85,115</sup>

The diffraction limited excitation spot in this experiment is ~300 nm (FWHM), whereas DNQDI has a size of ca. 2 nm. The insensitivity of this measurement to the position of a 2 nm sample in the 300 nm excitation spot shows that pulse shaping free of diffraction-based spatio-temporal artifacts was achieved with a resolution approximately 2 orders of magnitude beyond the diffraction limit. The importance of correcting for spatio-temporal coupling is demonstrated by the fact that the magnitude of the signal variations obtained with uncorrected beams is comparable to the real molecular signals obtained in these types of measurements; i.e. the vibrational wavepacket oscillations would almost totally be obscured by the spatio-temporal coupling artifact.

While these experiments show that no variations in signal from the detection volume due to fluctuations in the overlap between excitation and sample volume are present anymore, it is important to show that the double pass scheme not only frees the experiment from spatiotemporal coupling, but also provides the absolutely correct phase shape in the focus. An experiment investigating this would have two purposes: to show that the Wefer-Nelson objection against the double pass scheme does not hold, i.e. a correct phase measurement is possible; and to show that phase control with subwavelength resolution is therefore a viable possibility.

## 2. Beating spatio-temporal coupling

We achieved these objectives through phase measurements on BBO nanocrystals. Briefly, the pulses of the broadband setup (Ti:Saphh plus 4f-shaper) were calibrated using the MIIPS method outlined in Chapter 1. The calibrated, Fourier limited pulses were then used for imaging Second Harmonic Generation from nanocrystals (as shown in Figure 2.8). The resulting image clearly shows an isolated crystal; the width feature in the image is close to the diffraction limit for 2-photon signals ( $\lambda(2\sqrt{2}NA)^{-1}$ ), indicating that the crystal is not larger than several nm.

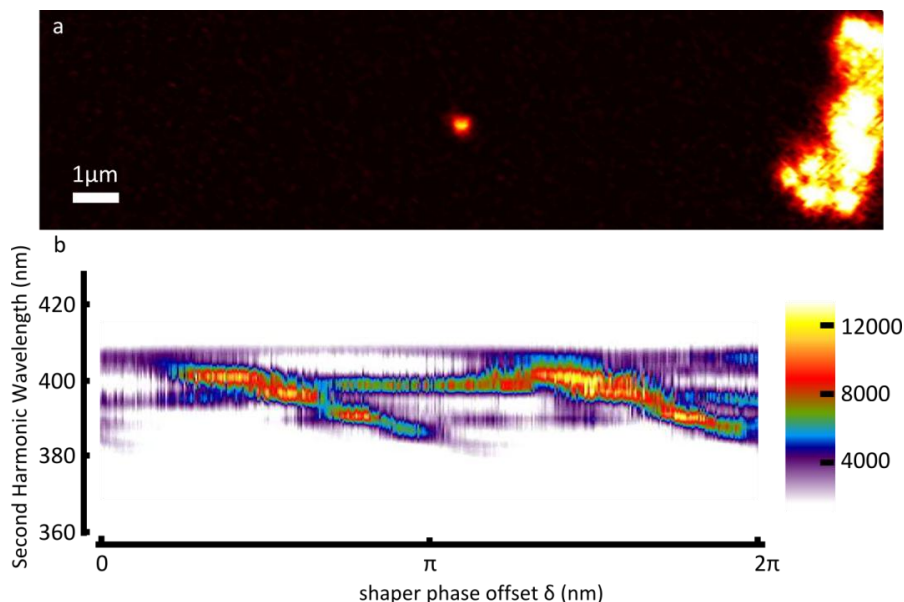


Figure 2.8: **Phaseshaped Second Harmonic Generation from a nanocrystal.**  
a) Image in Second Harmonic from a sample with BBO crystals. b) MIIPS trace obtained from the central nanometric BBO crystal.

The crystal was subsequently brought into the center of the focus and a MIIPS-run was performed, using the SH from the crystal as signal. The resulting MIIPS trace displays the two parallel lines (within the noise limits of the measurement) that mark a diffraction limited pulse. This shows that a calibration, averaged over the focus with a micrometric BBO plate, and one with a BBO nanocrystals at a specific point in the focus, provide the same result, indicating that not only the intensity but also the spectral phase is uniform over the focus, and the double pass system performs as required. Finally, it shows the for phase-controlled and coherent control experiments at deep subwavelength and single molecule resolutions; this will be expanded upon in chapters 5 and 6, with phase-sensitive measurements on coherence in single light harvesting complexes, and deep-subwavelength phase shaping utilizing plasmonic antennas.

## 2.8 Conclusions

We have shown that pulse shapers in the general single-pass configuration introduce a spatio-temporal coupling in laser pulses that can severely influence ultrafast spectroscopy and coherent control measurements. The magnitude of the spatial effects caused by spatio-temporal coupling depends on the spectral modulations applied to the shaped pulse, on the steepness of the phase gradients created in the shaping mask, and on the relative sizes and spatial uniformity of the excitation, sample and detection volumes in the experiment. Through experiments on single gold nanoparticles we have demonstrated the significant magnitude of these effects. Theoretically, spatio-temporal coupling can be canceled out or significantly diminished with pulse shapers in a double-pass configuration. By using single fluorescent molecules and BBO nanocrystals as local probes of the electric field, we have demonstrated with a resolution of down to 2 nm that the double-pass pulse shaping produces homogeneous shaped fields, both in amplitude and phase. This kind of correction is essential to obtain reliable information in experiments using shaped laser pulses, and will be utilized throughout the thesis to achieve nanoscale coherent control.

This chapter has partially been published as Brinks et al, *Optics Express* **19**, 26486 (2011).

**In this chapter, we argue that a phase-lock brings a new dimension to pump probe experiments and allows for resolving the persistence of coherence in a room temperature single organic molecule. We show measurements of coherence decay, signatures of a rabi-oscillation, and create an ultrafast qubit, all in and from one single organic molecule at room temperature.**

### **3. Femtosecond coherence and quantum control of single molecules at room temperature**

## 3.1 Introduction

Quantum coherence is a central feature in many physical phenomena, connecting fields as diverse as quantum computing and light harvesting. The former relies on manipulations of coherent superposition states in multi-level systems to store and process information, surpassing the most powerful classical computers for several applications<sup>119–122</sup>. For light-harvesting nature exploits very long-lived electronic coherences of hundreds of femtoseconds in the initial steps of photosynthesis in bacteria and algae to achieve highly efficient and unidirectional energy flow towards reaction centres<sup>83,84,123–125</sup>. This observed longevity of coherences in photosynthetic pigment-protein complexes at physiological conditions<sup>124</sup> questions the notion that interactions with the local environment universally lead to decoherence. The particular structure of protein scaffolds may rather protect electronic coherences<sup>83,84,123,124</sup>, which opens interesting perspectives for natural quantum devices, as also suggested by the recent proposal of entanglement in light-harvesting complexes<sup>125–128</sup>. Hence, unravelling the origins of coherence and decoherence on a nanoscopic scale is of high interest in many areas of physics.

Single-molecule detection combined with femtosecond pulse-shaping techniques provides a unique approach to gain insights into the ultrafast photophysics of individual quantum systems and to reveal correlations between e.g. structural properties and coherence times. In previous years, the van Hulst group succeeded in resolving incoherent vibrational relaxation in individual molecules at room temperature<sup>129</sup> through an incoherent (degenerate) pump-probe measurements. Part of my PhD was to implement a coherent, phaselocked pump-probe scheme, based on pulseshaping, and investigate what extra information could be extracted from single molecules this way.

Here we demonstrate that electronic coherences in single molecules can be established, probed, and controlled in disordered, non-crystalline environments under ambient conditions that are typical in e.g. biologically relevant systems. Our data reveal large variations in the time scales of the coherence decay for different individual molecules resulting from varying interactions with their particular local surroundings. In the coherent regime we are able to induce Rabi-oscillations, which were on single systems so far only observed on organic molecules in crystalline matrices<sup>130,131</sup> and quantum dots<sup>132,133</sup> at low temperatures, as well as on nitrogen-vacancy centres in diamond at room temperature<sup>134</sup>. Moreover, we explore the limits of ultrafast manipulation of coherent superposition states by controlling the Bloch vector of a single molecule. This fundamental step constitutes a single-qubit operation at femtosecond time scales.

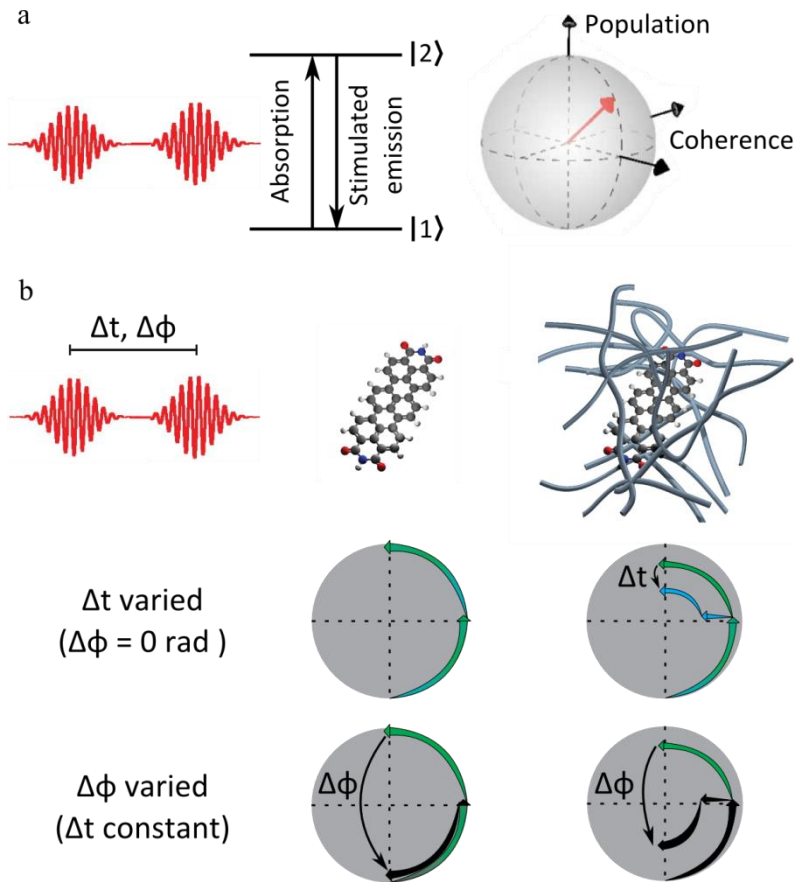


Figure 3.1: **Concept of the experiments.** a) A sequence of ultrafast, phaselocked pulses resonantly drives a single molecule between the ground ( $|1\rangle$ ) and lowest excited level ( $|2\rangle$ ). The state of this 2-level system is visualised by the Bloch-vector (red arrow) on the Bloch sphere, where the poles correspond to the eigenstates (“south”:  $|1\rangle$ , “north”:  $|2\rangle$ ) and any other point indicates a coherent superposition between ground and excited state electronic wavefunctions. b) Influence of varying the delay time  $\Delta t$  and relative phase  $\Delta\phi$  on the trajectories of the tip of the Bloch vector: Without electronic dephasing a change of  $\Delta t$  at constant  $\Delta\phi$  does not affect the trajectory (top left sphere). In contrast, with dephasing the magnitude of the Bloch vector continuously decreases, resulting in a measurable change in the excited state population for increasing  $\Delta t$  (top right). The introduction of a phase change  $\Delta\phi$  (at constant  $\Delta t$ ) allows control of the superposition state by altering the rotation direction of the Bloch vector (bottom). The fidelity of preparation and control of coherent superposition states is reduced with dephasing (right) as compared to the situation without dephasing (left).

Although recent room temperature experiments allowed for the detection of a very small number of molecules by stimulated emission<sup>9</sup> and even of individual chromophores by absorption<sup>5,8,135</sup>, for single fluorescent molecules the best signal-to-noise and signal-to-background ratios are still achieved by recording the incoherent emission. The challenge in our experiments is therefore to translate information about variations of electronic coherences into changes of the spontaneous emission, i.e. of the excited state population probability. The basic idea of our approach is sketched in Fig. 3.1: A single molecule is resonantly excited into the purely electronic transition between the electronic ground ( $|1\rangle$ ) and lowest excited state ( $|2\rangle$ ) by femtosecond phase-locked double-pulse sequences. This induces stimulated absorption and emission processes and prepares this 2-level system in a certain state that is visualised by a vector (Bloch vector) on a sphere with unity radius (Bloch sphere, Fig. 3.1a)<sup>43,136,137</sup>. A vector pointing to the poles represents an eigenstate of the 2-level system, while any other position indicates a coherent superposition between levels  $|1\rangle$  and  $|2\rangle$ . Interaction with the first pulse generally creates a coherent superposition state corresponding to a rotation of the Bloch-vector away from its ground state position (“south” pole, Fig. 3.1b). Depending on the experimental conditions several situations can then be distinguished. In the simplest case the molecule is completely isolated without interactions with its environment (Fig. 3.1b, left). If the phase difference  $\Delta\phi$  between the pulses is fixed at 0 rad, the second pulse rotates the Bloch vector further about the same axis as the first pulse<sup>137</sup>. Since interaction with the light field is the only process changing the state of the Bloch vector, its final position is independent of the delay time  $\Delta t$  (Fig. 3.1b, top left sphere). However, if the molecule is embedded in a disordered environment at room temperature (Fig. 3.1b, right), the phase memory between the ground and excited state wavefunctions is broken rapidly by pure dephasing processes, i.e. by interactions with the matrix<sup>138</sup>. Here, the magnitude of the Bloch vector is not preserved and decreases with time. Consequently, the position of the tip after the pulse sequence changes, and importantly, the excited state population becomes smaller as a function of  $\Delta t$  (Fig. 3.1b, top right sphere, green and blue arrows). The resulting decay of the spontaneous emission with increasing  $\Delta t$  directly provides information about the coherent superposition state of the molecule provided that population decay due to (non-)radiative transitions is negligible on the time scales of  $\Delta t$ . Key for the detection of coherence with this approach is the control of the relative phase  $\Delta\phi$  between the electric fields of the laser pulses, since  $\Delta\phi$  determines the rotation direction of the Bloch vector induced by the second pulse. Specifically, a  $\pi$  phase shift inverts the rotation direction and moves the Bloch vector back towards its ground state position (Fig. 3.1b bottom, green arrows:  $\Delta\phi = 0$  rad, black arrows:  $\Delta\phi = \pi$  rad). This control of  $\Delta\phi$  therefore offers the possibility to manipulate the motion of the Bloch vector before loss of phase memory and gives direct insight into the dephasing dynamics of single molecules.

## 3.2 Experimental method

For the experiment, single terrylenediimide (TDI, Fig 3.1b) molecules were dispersed in a poly(methyl-methacrylate) (PMMA) matrix at concentrations of ca.  $10^{-10}$  M and investigated on a sample-scanning inverted confocal microscope. The excitation source was an optical parametric oscillator (OPO, Automatic PP, APE) that provided non-transform limited pulses with a width of 260 fs (spectral band width: 18 – 21 nm full width at half maximum, FWHM) at a repetition rate of 76 MHz. The central wavelengths were between 622 and 640 nm to excite into (the high-energy tail of) the purely electronic transition of TDI (absorption max. in hexadecane: 643 nm, see Ref.<sup>139</sup>). A pulse picker (PulseSelect, APE) reduced the repetition rate to effectively 500 kHz (bunches of pulses with a repetition rate of 25 kHz, repetition rate within bunches: 4 MHz) to match it to the input of an acousto-optic programmable dispersive filter (Dazzler, Fastlite) that was used for pulse shaping. The shaper compressed the output of the OPO to transform-limited pulses with a width of 70 – 75 fs (FWHM) at the sample plane and generated pulse sequences with controlled delay time  $\Delta t$  and phase difference  $\Delta\phi$  between the electric fields of the output pulses. The shaped light was spatially filtered and collimated by a lens-pinhole-lens arrangement (see also chapter 2), directed into the microscope, and focussed on the sample by an oil-immersion objective with a high numerical aperture, NA = 1.3 (Fluar, Zeiss). To localise individual molecules a  $10 \times 10 \text{ um}^2$  region of the sample was scanned, spatially well-separated molecules were selected, and then successively moved into the focus of the objective. The fluorescence light was split on two single photon counting avalanche photodiodes (APDs, Perkin-Elmer) by a polarising beam splitter to determine the degree of polarisation, i.e. the orientation of the transition dipole moment in the focal plane. The emission of each molecule was monitored as a function of  $\Delta t$  and  $\Delta\phi$  until photobleaching. For data analysis (see below) only molecules were considered, for which a trace could be measured at least twice. The excitation intensity at the sample was simultaneously recorded by a photodiode and was between 0.2 and  $5 \text{ kW/cm}^2$ . All experiments were carried out at room temperature under ambient conditions.

## 3.3 Coherence in single molecules at room temperature

Upon (near-)resonant excitation of the purely electronic transition of TDI with phase-locked double-pulse sequences (pulse width 75 fs) different molecules show distinct emission responses as a function of the delay time and relative phase. Examples of delay traces with  $\Delta\phi$  fixed at 0 rad are depicted in Fig. 3.2a-d (black curves), with the time-averaged excitation intensity being kept constant during the acquisition of each trace. The emission signals in Figs. 3.2a,b,d feature pronounced variations of up to a factor of 2 with decay and recovery times, respectively, of several tens of fs, whereas the trace in Fig. 3.2c

is constant within the signal-to-noise ratio. For  $\Delta t > 300$  fs the emission of all investigated molecules remained constant.

The traces in Figs. 3.2a,b reflect the decay of coherences in single molecules with time constants of ca. 50 fs, because for TDI spontaneous emission as well as non-radiative transitions are negligible within the first 600 fs after excitation<sup>140</sup>. The turnover to flat and rising traces (Fig. 3.2c,d) is attributed to an increasingly stronger interaction between the laser field  $\vec{E}$  and the transition dipole moment  $\vec{\mu}_{12}$  between the electronic ground and excited state, i.e. an increasing Rabi-frequency  $\hbar\omega_{R,0} = \vec{\mu}_{12} \cdot \vec{E}_0$ . These variations in  $\omega_R$  come from different excitation intensities, random orientations of the TDI-molecules, and an intrinsic distribution of  $\vec{\mu}_{12}$  caused by varying local surroundings. For a given  $\Delta t$  this gives rise to different excited state probabilities from molecule to molecule, which in turn are reflected in the number of detected photons. In the examples in Fig. 3.2a-d the count rates increase from 400 to 2400 s<sup>-1</sup>, and the highest observed rate was 8000 s<sup>-1</sup> (Fig 3.3). These highest count rates correspond to the maximum that can be recorded from a single molecule excited at saturation levels with a repetition rate of 500 kHz and a typical detection efficiency of 1 – 2 %.

To gain quantitative insights into the ultrafast dynamics we evaluated the density matrix  $\rho$  for a two level system:

$$\rho = \begin{pmatrix} \rho_{11} & \rho_{12} \\ \rho_{21} & \rho_{22} \end{pmatrix} \quad (1.1)$$

by performing numerical simulations based on the optical Bloch equations in the rotating-wave approximation (RWA)<sup>43,137</sup>. These are given by

$$\frac{d\rho_{12}}{dt} = \frac{d\rho_{21}^*}{dt} = \frac{1}{2}i\omega_R(\rho_{11} - \rho_{22}) + (i\delta - \frac{1}{T_2^*})\rho_{12} \quad (1.2)$$

$$\frac{d\rho_{22}}{dt} = -\frac{d\rho_{11}}{dt} = -\frac{1}{2}i\omega_R(\rho_{12} - \rho_{21}) \quad (1.3)$$

with

$$\rho_{12} = \rho_{21}^* \quad (1.4)$$

$$\rho_{11} + \rho_{22} = 1 \quad (1.5)$$

where  $\omega_R$  is the rabifrequency,  $\delta$  is the detuning between the carrier frequency and the transition frequency and  $T_2^*$  is the pure dephasing time. We calculated the elements of  $\rho$  as a function of the delay time immediately after the pulse sequence interacted with the 2-level system. In the equations of motion for the diagonal terms of the density matrix  $\rho$ , pure electronic dephasing processes described by the time constant  $T_2^*$  (relaxation of off-diagonal elements of  $\rho$  or coherences) were included, while population decay (relaxation of diagonal elements of  $\rho$  or populations due to spontaneous emission and non-radiative

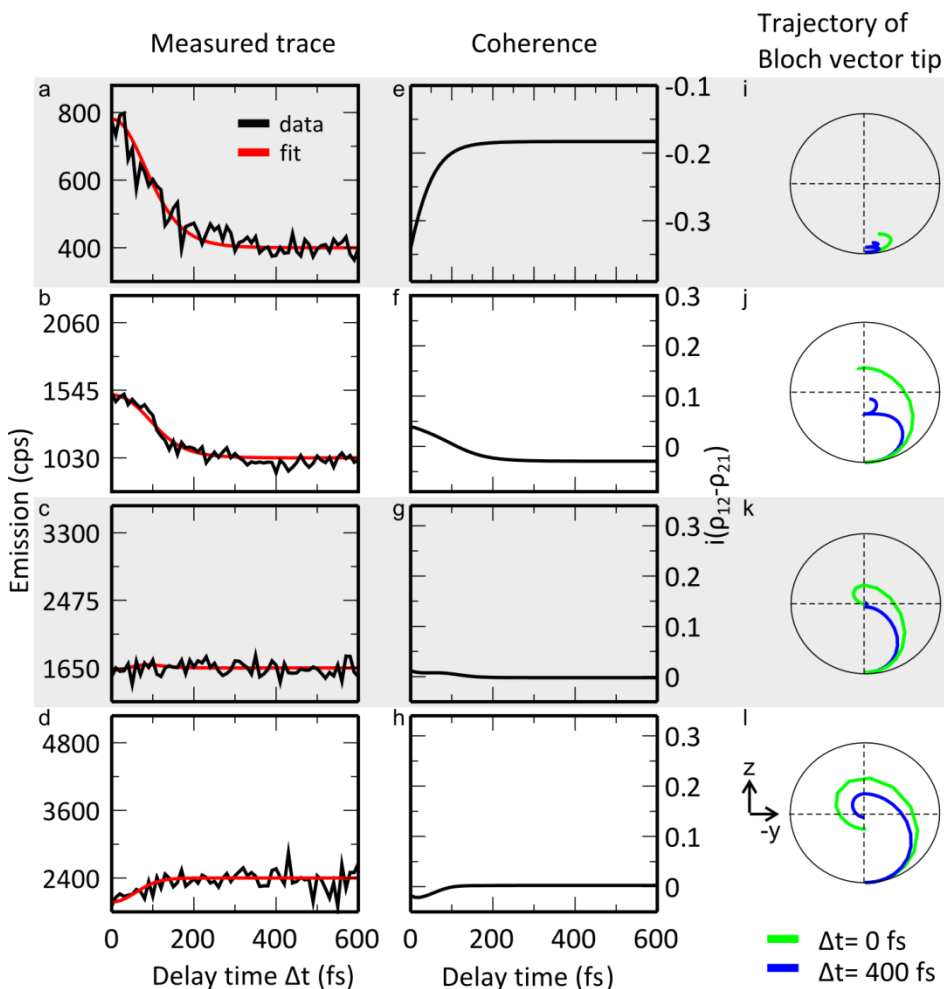


Figure 3.2: **Quantum coherence in single molecules: Coherence decay and Rabi-oscillations.** a-d): Black curves: Delay traces from different molecules with increasing Rabi-frequency  $\omega_{R,0}$  ( $\Delta\phi=0$  rad, cps: counts per second). Red curves: Simulations of the data based on the optical Bloch equations for a 2-level system yielding a)  $\omega_{R,0} = 0.01$   $\text{fs}^{-1}$ ; b)  $\omega_{R,0} = 0.035$   $\text{fs}^{-1}$ ; c)  $\omega_{R,0} = 0.06$   $\text{fs}^{-1}$ ; d)  $\omega_{R,0} = 0.06$   $\text{fs}^{-1}$ . e-h): Coherences as a function of  $\Delta t$  for the corresponding data. The magnitudes of the coherences decay with time constants  $T_2^*$  between 25 and 50 fs. i-l): Trajectories of the tip of the Bloch vector as a function of time for delays of  $\Delta t = 0$  fs (green) and  $\Delta t = 400$  fs (blue). The nutation angle of the Bloch vector increases with rising Rabi-frequencies and the magnitude decays with time due to pure electronic dephasing. For the highest  $\omega_{R,0}$  a full Rabi-oscillation is observed (d: nutation angle  $2\pi$ ). The trajectories always start in the ground state  $z = -1$ .

decay) was neglected, since we are only interested in the dynamics up to 600 fs and TDI has an excited state lifetime  $T_I$  of 3.5 ns in PMMA with a fluorescence quantum yield of  $\sim 1$  (see Ref.<sup>140</sup>).

The excitation into (the high-energy tail of) the purely electronic transition allowed the energy level structure of TDI to be described by a simple 2-level system with the electronic ground ( $|1\rangle$ ) and excited state ( $|2\rangle$ ), Fig. 3.1. To account for this slightly off-resonant excitation as well as for the distribution of transition frequencies of individual TDI-molecules due to locally different interactions with the matrix<sup>15</sup>, we included the detuning  $\delta = \omega_{12} - \omega$ , the offset between the transition frequency  $\omega_{12}$  and the carrier frequency  $\omega$  of the pulses. Owing to the pulsed excitation with similar values for the pulse width  $\tau_p$  and the pure dephasing time  $T_2^*$  we had to solve the Bloch equations numerically. The pulsed excitation is described by a time-dependent electric field amplitude  $\vec{E}(t) = \vec{E}_0 \cdot f(t)$  with the peak value  $\vec{E}_0$  and the envelope function  $f(t) = \exp(-t^2/2\tau_p^2) + \exp(-(t - \Delta t)^2/2\tau_p^2)$  of the double-pulse sequence in RWA. Consequently, the Rabi-frequency becomes time-dependent as well,  $\hbar\omega_R(t) = \vec{\mu}_{12} \cdot \vec{E}(t)$ , where  $\vec{\mu}_{12}$  is the transition dipole moment. We define the time-independent maximum Rabi-frequency  $\hbar\omega_{R,0} = \vec{\mu}_{12} \cdot \vec{E}_0$ , which is a free parameter in the simulations in addition to  $T_2^*$  and  $\delta$ . The density matrix  $\rho$  was evaluated as a function of  $\Delta t$  (in steps of 5 – 10 fs) immediately after the decay of the envelope of the second delayed pulse ( $\sim 3 \cdot \tau_p$  after the peak of the delayed pulse). Owing to the low repetition rate in our experiment both the excited state probability ( $\rho_{22}$ ) and the coherences ( $\rho_{12}, \rho_{21}$ ) completely decay before arrival of the next pulse pair. Therefore the initial conditions for the simulations at a given delay time are  $\rho_{11}(0) = 1$  (only ground state occupied) and for all other elements  $\rho_{ij}(0) = 0$ .

In our situation the excited state population probability as a function of  $\Delta t$   $\rho_{22}(\Delta t)$ , is directly proportional to the fluorescence count rate in the recorded traces. To fit the data we varied the free parameters in the Bloch equations, i.e. the pure dephasing time  $T_2^*$ , the maximum Rabi-frequency  $\omega_{R,0}$ , and the detuning  $\delta$ , and minimised the residuals between the measured traces and the simulated  $\rho_{22}(\Delta t)$ -curves.

We found that the density matrix as a function of the delay,  $\rho(\Delta t)$ , is very sensitive to the interplay between  $\omega_{R,0}$ ,  $T_2^*$ , and  $\delta$ , which is a consequence of the comparable values of  $\tau_p$ ,  $T_2^*$ , and the inverse maximum Rabi-frequency  $\omega_{R,0}^{-1}$  in our experiment (see Fig. 3.2). This sensitivity of the shape of the calculated traces to the fitting parameters is demonstrated by comparing the curves in Fig. 3.2c and d, which differ only in  $T_2^*$ . Hence, for the fits (Fig. 3.2a-d) the calculated  $\rho_{22}(\Delta t)$ -curves could be scaled such that their values at  $\Delta t = 600$  fs match the average count rate of the experimental traces between  $\Delta t =$

550 and 600 fs. Both curves can thus be overlaid without knowledge of the exact detection efficiency of our setup that depends, among other factors, on the detuning as well as on the unknown and random 3-dimensional orientation of the molecules. The best fit was determined by minimising the residuals between data and simulations. The coordinates of the Bloch vector tip used to calculate its time-dependent trajectories in Fig. 3.2 are related to the density matrix elements by  $x = \rho_{21} + \rho_{12}$ ,  $y = i(\rho_{21} - \rho_{12})$ , and  $z = \rho_{22} - \rho_{11}$  (see Refs. 23,24).

As evident from Fig. 3.2a-d the calculations (red curves) reproduce the data (black) very well and we find that  $\omega_{r,0}$  increases from 0.01 to 0.06 fs<sup>-1</sup> (from top to bottom). The turnover from decaying to rising delay traces thus indeed results from an increasing Rabi-frequency. The decay (Fig. 3.2a,b) and recovery (Fig. 3.2d) time constants are determined by the pure dephasing time  $T_2^*$  (convoluted with the finite pulse width), which is between 25 and 50 fs. The detuning  $\delta$  is always 0 cm<sup>-1</sup> for the examples shown here. Importantly, also the flat trace in Fig. 3.2c can be unambiguously simulated. This curve cannot be modelled by allowing very long or short dephasing times ( $T_2^* > 150$  fs or  $< 20$  fs), because this would have to be compensated for by unreasonable  $\omega_{r,0}$ -values.

Since we compute the entire density matrix to fit the delay traces, the coherent superposition state of each molecule can be reconstructed. The off-diagonal terms of  $\rho$  [here:  $i(\rho_{21} - \rho_{12})$ ] are depicted as a function of  $\Delta t$  in Fig. 3.2e-h for the corresponding data in Fig. 3.2a-d. The coherences decay with increasing delay times, and both the magnitudes and decay times are correlated to those of the emission signals. This demonstrates that the recorded fluorescence signals directly reflect the coherence decay in single molecules. We note that the coherences shown in Fig. 3.2e,f do not decay to zero for long delays, because for any given  $\Delta t$  the density matrix elements were calculated immediately after the decay of the delayed pulse and the coherences prepared by this pulse did not completely vanish in these two examples.

### 3.4 Rabi-oscillation in a single molecule at room temperature

The good agreement between data and theory justifies the approximations in the Bloch equations, and the femtosecond dynamics of single molecules is fully determined by  $T_2^*$ ,  $\omega_{r,0}$  and  $\delta$ . Using these parameters we can now directly visualise the time-dependent trajectories of the tip of the Bloch vector on the Bloch sphere<sup>136,137</sup> to gain further insight into the subtle differences in the interaction between the excitation pulse train and the molecules. For the traces in Fig. 3.2a-d, the corresponding trajectories are displayed in Fig. 3.2i-l for delays of  $\Delta t = 0$  fs (green) and  $\Delta t = 400$  fs (blue). In the trajectories in Fig. 3.2i,j the Rabi-frequencies are rather small and only absorption takes place. Here, the excited state population probability (z-component) after the pulse

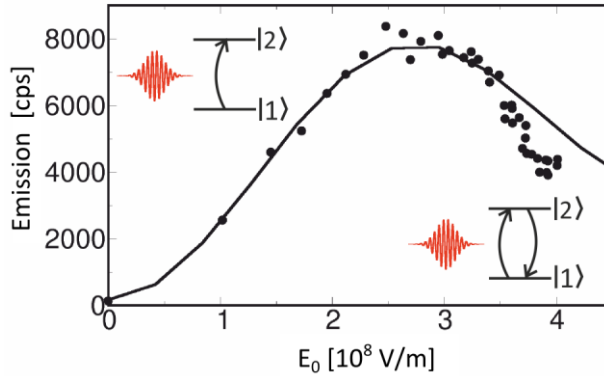


Figure 3.3: **One-Pulse Rabi-flopping of a single molecule.** The fluorescence of a single molecule shows a clear turning point in intensity when the power of a 50 fs excitation pulse is increased, passing through the point of full population inversion and back to an almost complete depletion of the excited state.

sequence decreases with  $\Delta t$ , since dephasing leads to less efficient interaction between the laser pulses and the increasingly shorter Bloch vector. Consequently, the observed emission signals decay with  $\Delta t$  (Fig. 3.2a,b).

In Fig. 3.2k,l the substantially higher  $\omega_{R,0}$ -values give rise to large nutation angles of the Bloch vector, and also stimulated emission during interaction with the laser pulses becomes important. Loss of phase memory renders this dumping of excited state population less efficient with increasing  $\Delta t$ , resulting in higher  $\rho_{22}$ -values at longer delays. The trajectory in Fig. 3.2d is particularly interesting because for  $\Delta t = 0$  fs (green) the nutation angle of the Bloch vector is about  $2\pi$ . Thus the observation of a rising emission signal as a function of  $\Delta t$  indicates that we monitor a full Rabi-cycle in a single molecule for  $\Delta t = 0$  fs. This interpretation is verified by single-pulse experiments ( $\Delta t = 0$  fs) on individual molecules, depicted in Figure 3.3, where we continuously increased the Rabi-frequency, i.e. the excitation power, and recorded the emission intensity. For several molecules we found first a rise and, at higher excitation intensities, a decrease of their fluorescence signals. This observation directly demonstrates Rabi-oscillations in single molecules at room temperature.

### 3.5 Control of the superposition state: a room temperature single molecule ‘qubit’.

Having established coherent superposition states and monitored their evolution in single molecules at room temperature, the next step is to manipulate these states before the inevitable fast decoherence in disordered matrices. For delays shorter than  $T_2^*$  a variation of  $\Delta\phi$  between the excitation pulses changes the axis

of rotation of the Bloch vector in a well defined way with respect to the rotation axis determined by the first pulse<sup>137</sup>. In particular, a  $\pi$  phase difference exactly reverses the sense of rotation (Fig. 3.1b, bottom). This provides a means to control the final coherent superposition state.

In Fig. 3.4 a delay- and phase-dependent measurement (dots) on the same single molecule is displayed together with numerical simulations (lines), where the pulses were in-phase (0 rad, green) and out-of-phase ( $\pi$  rad, black), respectively. The time-averaged excitation intensity was kept constant during the acquisition of both traces. Evidently, for long delays ( $\Delta t \gg T_2^*$ ) the emission is independent of  $\Delta\phi$  indicating a complete loss of phase memory, whereas before decoherence the count rate is strongly reduced by introducing the  $\pi$  phase shift. These data demonstrate that it is indeed feasible to manipulate the Bloch vector of single molecules despite femtosecond dephasing times.

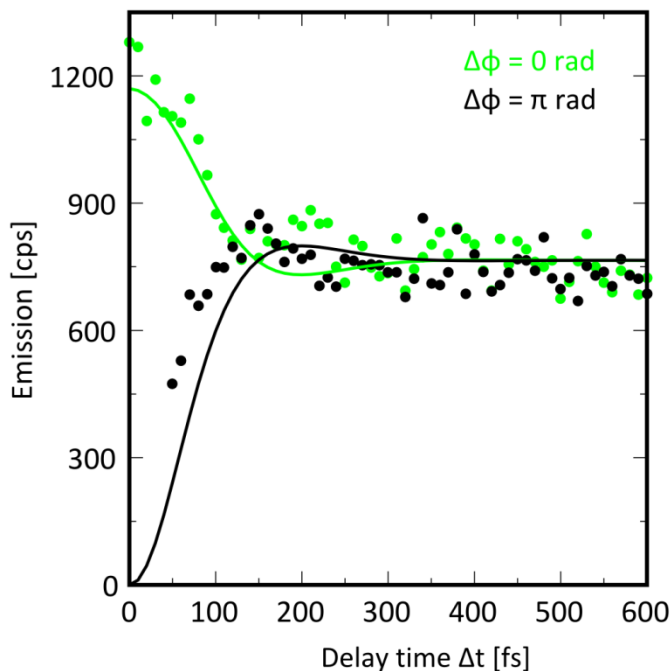


Figure 3.4: **A single molecule ‘qubitflip’**. Delay traces with  $\Delta\phi = 0$  rad (green dots) and  $\Delta\phi = \pi$  rad (black dots) measured on the same molecule (cps: counts per second). The solid curves represent numerical simulations for the corresponding data, yielding  $\omega_{R,0} = 0.03 \text{ fs}^{-1}$ ,  $T_2^* = 60 \text{ fs}$ , and  $\delta = 80 \text{ cm}^{-1}$ . Note that the excitation intensity was always constant during acquisition of all traces. Because for  $\Delta\phi \neq 0$  rad and  $\Delta t < 50 \text{ fs}$  the excitation intensity could not be kept constant, these data points were not retrieved.

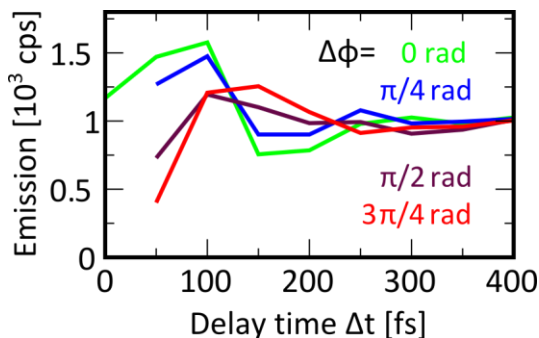


Figure 3.5: **Controlling the coherent superposition state of a single molecule.**

Emission signal of a single molecule as a function of the delay time and relative phase [ $\Delta\phi = 0$  rad (green),  $\pi/4$  rad (blue),  $\pi/2$  rad (brown), and  $3\pi/4$  rad (red)]. The oscillatory behaviour of these traces comes from a detuning of ca.  $200\text{ cm}^{-1}$ . Note that the excitation intensity was always constant during acquisition of all traces. Because for  $\Delta\phi \neq 0$  rad and  $\Delta t < 50\text{ fs}$  the excitation intensity could not be kept constant, these data points were not retrieved.

This is further illustrated by data from another single molecule, where the phase was changed in smaller steps of  $\pi/4$  rad (Fig. 3.5); the time-averaged excitation power is again constant for all data points. By an appropriate choice of  $\Delta t$  and  $\Delta\phi$  the Bloch vector can be rotated to any arbitrary position and any coherent superposition state, and thus excited state probability, can be created. In fact, such pulse sequences with particular  $(\Delta t, \Delta\phi)$ -combinations ( $\Delta t < T_2^*$ ) can be interpreted as basic ultrafast single-qubit operations.

The fidelity of coherent state preparation and control is determined by the interplay between the pulse width and the pure dephasing times of single molecules. For 53 molecules we determined the dephasing times, which are between 25 and 110 fs with a peak at ca. 60 fs. (Fig. 3.6).

This broad distribution of  $T_2^*$  reflects the heterogeneous nano-environments of individual TDI-molecules in the amorphous PMMA-host, because pure dephasing is caused by (near-)elastic scattering with matrix vibrations<sup>138</sup>, giving rise to rapid (i.e. faster than the excited state lifetime) fluctuations of the transition energy between the ground and excited state. The dephasing times are consistent with values determined from the line width of room-temperature fluorescence spectra of individual chromophores of ca.  $500\text{ cm}^{-1}$  (FWHM), which constitutes an upper limit for the homogeneous line width and yields a lower boundary for  $T_2^*$  of about 20 fs.

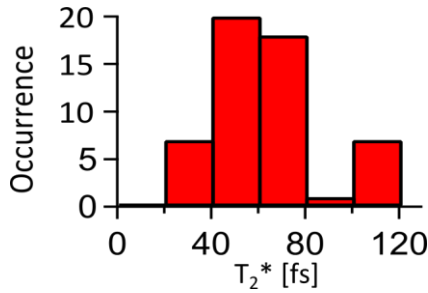


Figure 3.6: **Histogram of the pure dephasing times  $T_2^*$ .** The dephasing times were retrieved from 53 molecules; the broad distribution, with  $\sigma(T_2^*)$  almost equal to  $\langle T_2^* \rangle$ , reflects the heterogeneity of the environment of the TDI molecules.

In our experiments the dephasing time of each molecule represents a time-averaged value, because we have to average over many excitation-dephasing-emission cycles to collect a sufficient number of photons for each  $(\Delta t, \Delta\phi)$ -combination. Individual “dephasing events” that destroy the coherent superposition state occur at a particular time after excitation. For consecutive excitation-dephasing cycles this time varies due to the disordered, temporally fluctuating surroundings of single molecules at ambient conditions. As a consequence, both the simulated density matrix elements as a function of  $\Delta t$  as well as the time-dependent trajectories of the Bloch-vectors (Fig. 3.2) represent time-averaged curves. From the ergodic principle, stating that a time average is equivalent to an ensemble average, it follows that the coherence decays observed in our experiments (Figs. 3.2, 3.3) can be identified with the envelopes of the optical free-induction decays (OFID) of individual molecules. The OFID is usually associated with the coherence decay in an ensemble of transition dipole moments<sup>137,141,142</sup> However, in contrast to such bulk measurements, where an ensemble-averaged OFID is recorded, we are able to resolve variations in the coherence decay times for different individual molecules caused by varying local surroundings and interactions. These data constitute the first measurement of the OFID of a single quantum system in a solid, disordered matrix at room temperature. This was so far only observed on single nitrogen-vacancy electron spins in the crystalline and highly pure diamond environment<sup>143</sup>.

## 3.6 Conclusions

The techniques introduced in this chapter were our first foray into single molecule coherent control, state preparation at room temperature, and measurements of coherence in single quantum-systems at room temperature. They can be applied to many types of single quantum systems, particularly to natural photosynthetic light-harvesting complexes with their ten times longer electronic coherences<sup>83,84,123</sup>. For these multichromophoric systems coherent exciton dynamics and the influence of structural properties on electronic coherences can thus be probed on the level of single units even in highly complex and heterogeneous environments under physiological conditions. Together with the recent proposal of entanglement in such assemblies<sup>126,127</sup> this also opens fascinating routes towards ultrafast optical control of a single complex, representing a truly nanoscopic quantum device. These are projects that will be explored in the next chapters, investigating manipulation of single molecules below the decoherence times (chapter 4) and coherence in single light harvesting systems (chapter 5).

Most of this chapter was published as  
R. Hildner, D. Brinks & N.F. van Hulst, *Nature Physics* **7**, 172-177 (2011)



**In this chapter, we argue that the single molecule approach is necessary to bring control and measurements of quantum states in complex systems to the next level: from isolated or uniformized samples to complex systems interacting with their environment. We show that, staying below the decoherence times established in the previous chapter, we can probe vibrational wavepacket oscillations in and perform coherent control of a single organic molecule in a disordered environment at room temperature.**

**4. Visualizing and manipulating  
vibrational wavepackets of single  
molecules at room temperature**

### 4.1 Introduction

The active steering of chemical reaction pathways and the optimization of energy conversion processes<sup>35,81</sup> provide striking examples of the coherent control of quantum interference through the use of shaped laser pulses: i.e. creating a coherent superposition state in a quantum system, manipulating this superposition state before dephasing events have destroyed it, and thereby steering the quantum system into a predetermined state.

Experimentally, coherence is usually established by synchronizing a subset of molecules in an ensemble<sup>71,72,82–84,123,144</sup> with ultra-short laser pulses<sup>145</sup>. But in complex systems where even chemically identical molecules exist with different conformations and in diverse environments, the synchronized subset will have an intrinsic inhomogeneity that limits the fidelity of control can be achieved. A natural—and, indeed, the ultimate—solution to overcoming intrinsic inhomogeneities is the investigation of the behaviour of one molecule at a time.

The single-molecule approach<sup>1,10,146</sup> has provided useful insights into phenomena as diverse as biomolecular interactions<sup>147–149</sup>, cellular processes<sup>150</sup> and the dynamics of supercooled liquids<sup>151</sup> and conjugated polymers<sup>152</sup>. The advent of superresolution techniques like STED<sup>153,154</sup> and PALM<sup>20,21</sup> has made single molecule physics a defining aspect of applied microscopy, while its fundamental aspects remain of high interest<sup>3,15,155–162</sup>.

Before we showed the first preparation, probing and manipulation of coherent superpositions in single molecules at room temperature<sup>85,86</sup>, coherent state preparation of single molecules was restricted to cryogenic conditions<sup>130</sup>, while at room temperature only incoherent vibrational relaxation pathways had been probed<sup>129</sup>. Here we report the observation and manipulation of vibrational wave-packet interference in individual molecules at ambient conditions. We excite molecules with pulses significantly shorter than their decoherence time; this provides the room to manipulate and read out the dynamics of superposition states encompassing multiple vibrational levels: vibrational wavepackets. We show the possibility of adapting the time and phase distribution of the optical excitation field to the dynamics of each molecule and achieve control with a fidelity unattainable in bulk experiments.

For few-atom molecules, coherent control schemes can be designed on the basis of theory<sup>163</sup>. For more complex systems, such as large (bio-)molecules at ambient conditions, ab initio quantum mechanical calculations fail, and the elegant approach of closed-loop adaptive feedback<sup>164</sup> has gained attention. The process of examining a physical system provided by these black box optimization routines is fundamentally different from that of an experimenter recording a molecular response as a function of deterministically changed parameters. The entire experiment is viewed as an information carrying entity, almost a computer, that can be used to write algorithms which allow certain tasks; the way the information carrying system responds to a particular algorithm then allows to extract properties from the system<sup>164–166</sup>.

This approach provides a unique perspective on physics as a science of information, and the interpretation of physical phenomena in terms of

information storage and transfer has been remarkably effective. The implementation of pulse shaping by self-learning algorithms has led to the coherent control of a wide variety of photo-induced processes, e.g. selective fragmentation<sup>74</sup>, laser-induced fluorescence<sup>167</sup>, coherent anti-Stokes Raman<sup>168</sup> and high-harmonic generation<sup>169</sup>. In all of these studies, the time, phase and frequency content of the optical field is experimentally optimized to obtain a certain product state. The resulting optimized pulse reflects the dynamics of the underlying processes and can take non-trivial shapes.

The closed loop approach has however one disadvantage as outlined in chapter 2: it is prone to artifacts, due to the fact that for the implementation of the genetic algorithms the molecular system and the laser interrogating the molecular system are one physical entity. This is often not explicitly taken into account, and any change in the combined system is for the sake of the research interpreted as a response of the molecule. A laser system that does not respond as expected to changing pulse shapes (i.e. due to spatio-temporal coupling, see chapter 2) will therefore easily introduce artifacts into the experiment that, due to black box nature of the measurement, are hard to weed out<sup>170</sup>.

This practical consideration does not preclude the theoretical beauty of an experiment where, in essence, the system under investigation lets the experimenter know by itself what the most relevant information about the system is. A more fundamental issue with applying this approach to real life physical entities is that a full optimization, theoretically, depends on the ability to run an optimization *ad infinitum* in order to be sure that the experiment has not got stuck in a local optimum instead of the global optimum. This is often not compatible with the finite lifetime or stability of an experiment. This consideration critically influences the conclusions drawn from coherent control experiments run for limited amounts of time.

Especially in a single-molecule measurement, the challenge is to extract information from the limited number of fluorescence photons obtainable before photobleaching; a long optimization process is not feasible. The practical consideration of spatiotemporal coupling is a further reason why we have chosen not to apply genetic algorithms, but to deterministically scan parts of the parameter spaces we have available.

Fortunately, optimal control theory on model systems<sup>171,172</sup> and experiments on large molecules<sup>71</sup> have demonstrated that complex pulses can often be simplified to a physically more intuitive shape with comparable efficiency. Typically, in the time domain, the optimum optical field takes the shape of a sequence of pulses separated by a time (femtoseconds to picoseconds) that is characteristic of the molecular dynamics. We therefore interrogated the coherent dynamics of individual molecules by monitoring the fluorescence emission after excitation with a sequence of equi-spaced phase-locked laser pulses. Both the inter-pulse time delay ( $\Delta t$ ) and phase shift ( $\Delta\phi$ ) were controlled (Fig. 4.1) The excitation intensity was kept constant for all ( $\Delta t$ ,  $\Delta\phi$ ) combinations, at values causing no significant depletion of ground state population probability, so that the single-molecule fluorescence intensity provided a direct measure of the excitation probability.

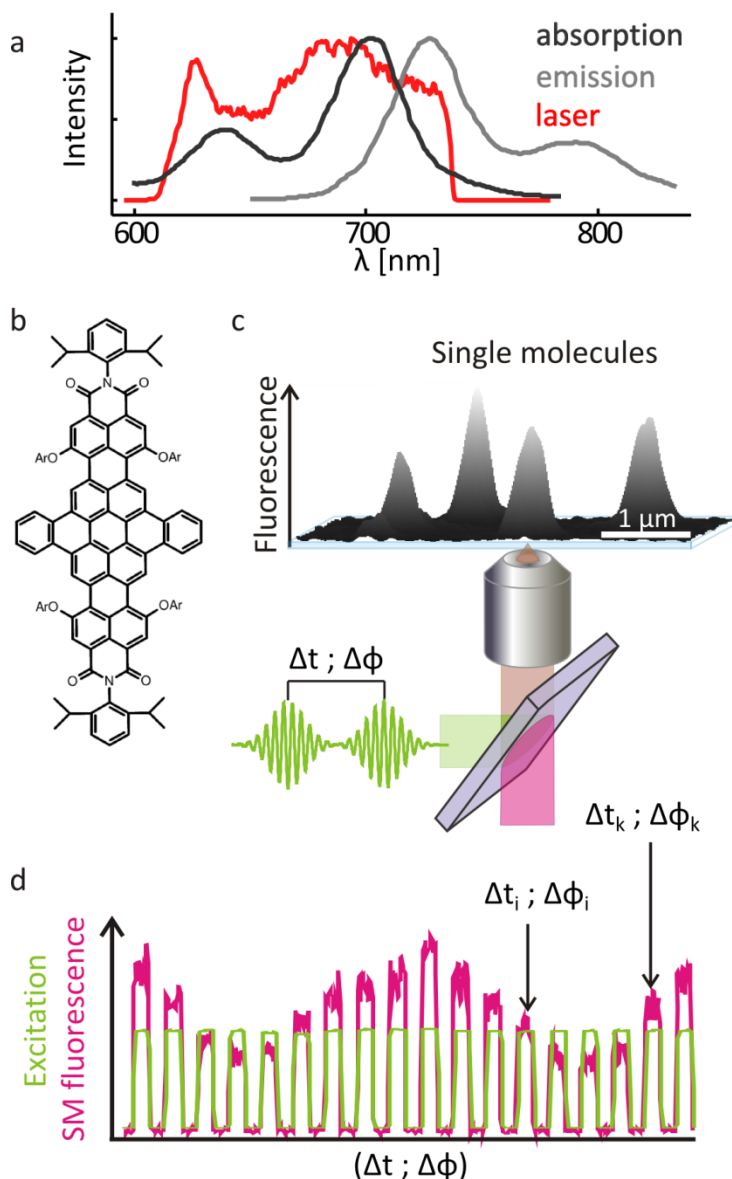


Figure 4.1: **Ultrafast coherent excitation of single molecules.** a) Spectra of the fluorophore (DNQDI<sup>118</sup> dissolved in toluene) and broad-band excitation laser used (see §4.2) b) Structure of DNQDI. c) Single fluorescent molecules were imaged and investigated in an epi-confocal microscope. Each individual molecule was excited with tailored sequences of 15-fs (full-width at half-maximum) pulses defined by the inter-pulse time delay  $\Delta t$  and phase shift  $\Delta \phi$ . Both  $\Delta t$  and  $\Delta \phi$  were controlled with a double-pass 4f pulse shaper as explained in chapter 2. c) The fluorescence intensity of the single molecules was recorded for different combinations of  $\Delta t$  and  $\Delta \phi$  (e.g.  $(\Delta t_i, \Delta \phi_i)$ ,  $(\Delta t_k, \Delta \phi_k)$ , etc) which were applied sequentially, separated by periods of no illumination and repeated until the molecule photobleached.

## 4.2 Experimental method

Dinaphthoquaterrylenebis(dicarboximide) (DNQDI; N,N'-bis-(N-2,6-diisopropylphenyl)-1,6,11,16-tetrakis[4-(1,1,3,3-tetramethylbutyl)phenoxy]-8,9:18,19-dinaphthoquaterrylene-3,4:13,14-bis(dicarboximide))<sup>118</sup> molecules were immobilized in a poly(methyl-methacrylate) film spin-cast from a toluene solution onto a standard microscopy glass coverslip. Conditions were adjusted to obtain a film thickness of about 40 nm and one DNQDI molecule per square micrometer on average. DNQDI has a fluorescence lifetime of about 3 ns, a quantum efficiency of 40% and a molar extinction coefficient  $\epsilon = 142,900 \text{ M}^{-1} \text{ cm}^{-1}$  ( $62,800 \text{ M}^{-1} \text{ cm}^{-1}$ ) at 700 nm (638 nm)<sup>118</sup>.

A broad-band, temperature and atmosphere (100% N<sub>2</sub> with 0.05 bar overpressure) stabilized, Ti:Sapphire oscillator (Octavius 85M, Menlo Systems) was used to obtain femtosecond pulses in the visible–near-infrared at a repetition rate of 85 MHz. For the molecular excitation, a band of 120 nm, centered at 676 nm, was selected and compressed to 15-fs pulses in the focus of a 1.3 NA Zeiss Fluor objective. Pulse shaping was performed with a modified double-pass 4f-shaper based on a liquid crystal spatial light modulator (see chapter 2). After spatial filtering, pulse characterization was carried out at the sample plane using the multiphoton intrapulse interference phase scan (MIIPS) method. The fluorescence of single molecules was detected in an epifluorescence confocal configuration. Suitable optical filters were used to separate the Stokes shifted fluorescence emission from residual excitation light, which was suppressed to a fraction of about  $10^{-10}$  in the detected signals from single molecules. Avalanche photo-diodes (APDs, Perkin-Elmer) were used as single photon detectors. The photon collection-and-detection efficiency of the set-up was ~1-2%.

Images (Fig 4.1b) were obtained by scanning a  $10 \times 10 \mu\text{m}^2$  area of the sample on a  $256 \times 256$  pixel grid with an integration time of 6 ms per pixel. Fluorescence versus  $\Delta t$  traces (Figs. 4.2, 4.4) were obtained by selecting a region of interest (ROI) containing the image of one molecule and integrating the fluorescence of all pixels in that ROI. The  $(\Delta t, \Delta\phi)$  excitation maps (Fig 4.5) were obtained by monitoring the fluorescence emission of the single molecules for 400 ms at each combination of  $(\Delta t, \Delta\phi)$ . In between different  $(\Delta t, \Delta\phi)$  combinations, the excitation light was blocked for another 400 ms (as shown in Fig 4.1c). This accommodates the time it takes for the shaper to load the shape for the next  $(\Delta t, \Delta\phi)$ -combination. The series of  $(\Delta t, \Delta\phi)$  values was repeated until the molecule photobleached. Only molecules for which each  $(\Delta t, \Delta\phi)$  combination could be measured at least twice were considered in analysis. Owing to the fixed acquisition time, the shot-noise level varies; typically, each data point was determined with a total of 4,000 photons which gives a shot-noise level of 1.5%. For the measurements shown in Fig 4.2 the laser power fluctuations were determined to be <5% and for the measurements in Fig 4.4 and 4.5 <2%. Thus, the total uncertainty of the data ranges from 2.5% to 6%. The 85 MHz repetition rate of the laser system was high enough to enable the detection of single-molecule fluorescence and sufficiently low to accommodate

the fluorescence lifetime of DNQDI between successive trains of excitation pulses. The excitation power was  $\sim 1 \times 10^{-6}$  W ( $1.2 \times 10^{-14}$  J per pulse) in all measurements, which, for a diffraction limited spot at 800 nm wavelength, 15 fs pulses and a repetition rate of 85 MHz, corresponds to a peak power density of  $1 \times 10^9$  W/cm<sup>2</sup>, which is typically between 1 and 2 orders of magnitude below the values needed for fluorescence saturation, depending on the overlap of the molecular dipole with the excitation field (both in spectrum and polarization). In this context, it is also instructive to compare Figure 3.3: the position in a rabi-cycle scales with pulse area, which means that for a pulse that is 15 fs instead of  $\sim 50$  fs the values for  $E_0$  are 50/15 $\sim$ 3.5 times higher to get to the same position in the rabi cycle; a peak power density of  $1 \times 10^9$  W/cm<sup>2</sup> translates into  $P_{D,0}=E_0^2/Z_0$ , with  $Z_0 = (\epsilon_0 c_0)^{-1} \approx 377$ ,  $E_0=0.5 \times 10^8$  V/m. The equivalent position in Fig. 3.3 sits at  $\sim E_0/3.5 \approx 0.15 \times 10^8$ , which clearly is far from the saturation regime that starts at  $E_0 \approx 2 \times 10^8$  for a molecule that features close to optimal overlap between the molecular dipole and excitation field in orientation and spectrum. Note that this is only a back of the envelope comparison and that the exact dynamics of the populations and coherences in the molecule are clearly influenced not only by pulse area but also by peak power, pulse width, spectral overlap and multiple energy levels by themselves.

This excitation scheme gives typical detected single-molecule count rates of  $(3-4) \times 10^3$  counts s<sup>-1</sup> with a signal-to-background ratio  $SBR \approx 10$  for the integrated signals, whereas the count-rate saturates around  $(5-6) \times 10^5$  cps, depending on the molecule, consistent with a detection efficiency of  $\sim 1-2\%$  (see chapter 3). Background count rates are between 300 and 400 counts s<sup>-1</sup>,  $\sim 130$  counts s<sup>-1</sup> of which are detector dark counts.

### 4.3 Wave packet oscillations in a single molecule at room temperature

In a first experiment, single fluorescent molecules were imaged under excitation with a two-pulse sequence. Each image was acquired with a particular  $\Delta t$  and fixed  $\Delta\phi = 0$  (Fig 4.2a). Even though the same excitation intensity was used for all images, the molecules fluoresce with varying intensity, depending on  $\Delta t$ . Remarkably, the individual molecules do not collectively appear brighter or dimmer but show characteristic individual changes in fluorescence as a function of  $\Delta t$ . Plotting the integrated fluorescence emission of each molecule versus  $\Delta t$  reveals an oscillatory behaviour of the excitation probability, as in the examples shown in Fig 4.2b. Evidently, the probability of photoexcitation of the single molecules depends on the femtosecond temporal distribution of the photons available for absorption and varies from molecule to molecule.

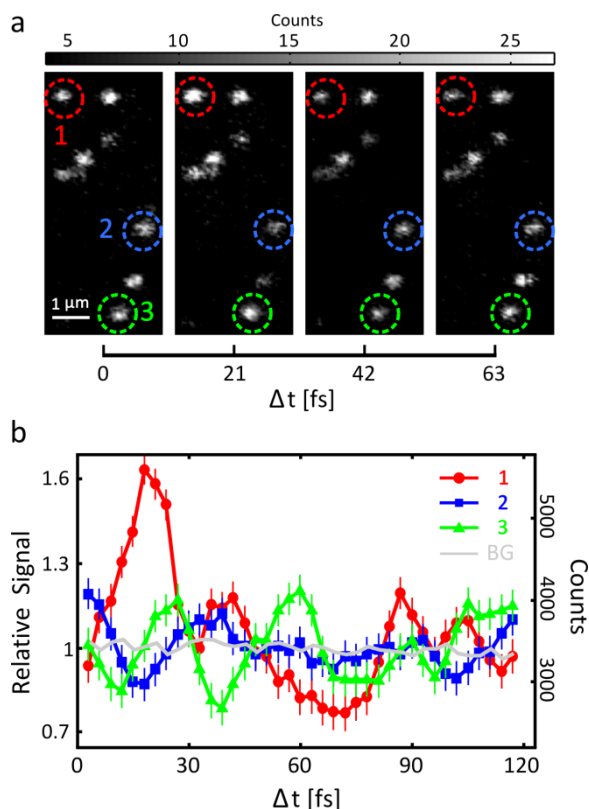


Figure 4.2: **Single-molecule wave-packet interference.** a) Fluorescence images of single molecules excited with two mutually delayed ( $\Delta t$ ), phase-locked laser pulses. b) Integrated intensity as a function of  $\Delta t$  for the fluorescence emission of the three molecules marked in a. A typical background trace is shown for reference. The counts on the right-hand axis are put for reference and are valid for trace 2. The traces are normalized to their respective average in order to visualize fluctuations in the intensity. Error bars  $\pm 1\sigma$ .

The observed oscillatory behaviour can be explained in terms of wave-packet interference (WPI)<sup>173,174</sup> (Fig. 4.3). Initially, the molecule is in the electronic ground state. The first optical pulse transfers probability amplitude to the excited state (Fig. 4.3a). If the pulse has enough bandwidth, it excites several vibrational levels and generates a quantum wave packet that will then travel in a round trip across the excited-state potential surface, with certain group and phase velocities. The interaction with the second, delayed optical pulse generates an additional wave packet in the excited state. Enhancement or suppression of the excitation probability arises from constructive or destructive quantum interference, respectively, between these two wave packets (Figs. 4.3 b-d). Alternatively, the results can be interpreted in the frequency domain, where the time delay between the phase-locked pulses translates into a modulation of the spectrum.

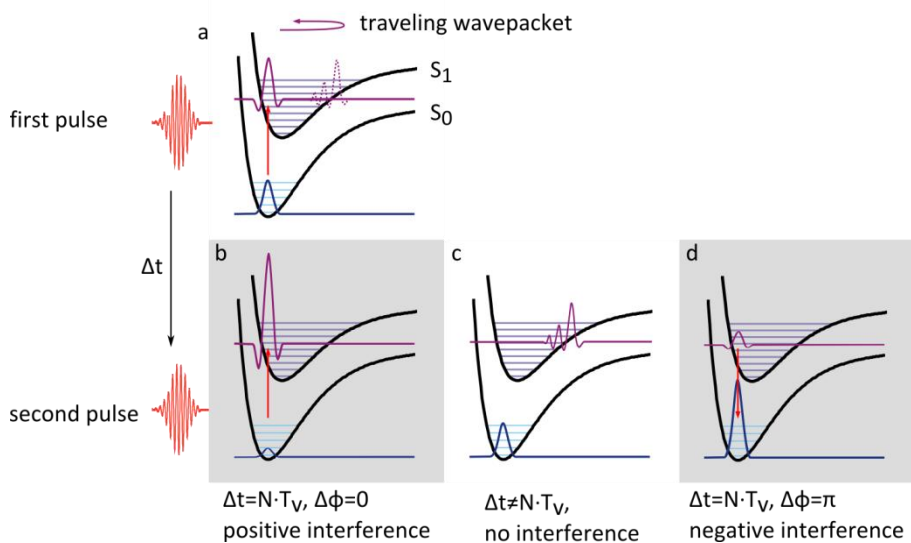
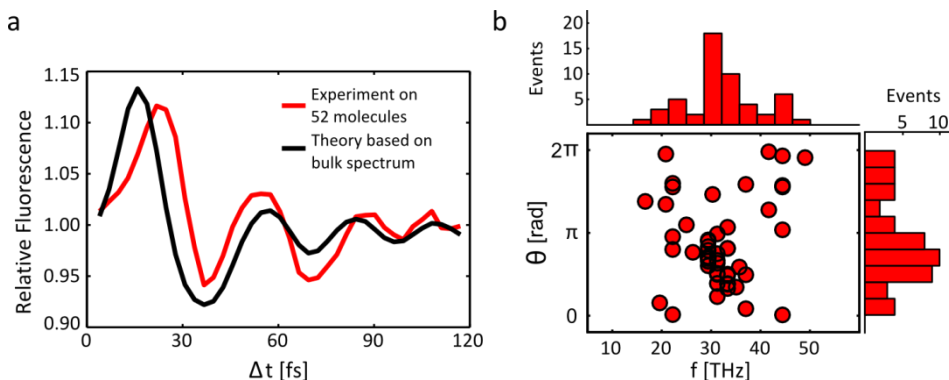


Figure 4.3: **Illustration of vibrational wavepacket interference.** a) The first excitation pulse creates a vibrational superposition in the first electronic excited state (vibrational wavepacket). b-d) If the delay of the second pulse coincides with the roundtrip time of the vibrational wavepacket  $T_v$ , it can excite a second wavepacket that interferes positively (b) or negatively (d) with the first wavepacket, thus enhancing or suppressing the excited state population. If the delay of the second pulse is off, no interference takes place (c).

The exact shape of the WPI-curve depends critically on the shape of the excited state potential landscape, the vibrational energy levels encompassed in the wavepacket and their coupling strength to the electronic dipole, and the dephasing of the wavepacket. Dispersion (dephasing) of the wavepacket leads to lower fidelity interference, broadening and damping the observed oscillations in the WPI trace. Extracting the information leading to a correct description of the Hamiltonian from these curves is a theoretical field in itself<sup>175,176</sup> (Indirect Quantum Tomography of Hamiltonians) and in the context of this experiment still work in progress.

With the first recording of wavepacket interference in single, organic units at room temperature, we can however elaborate further in several directions. Comparisons of average values to those obtained in bulk experiments will give information strengths and limits of the single molecule vs. the bulk approach. Expanding the measured traces into distributions of physical parameters that can be extracted from them will give information on the interaction of each quantum unit with its environment and allow a search for correlations. Finally, expanding the parameter space in the coherent control experiments will allow for higher fidelity superposition states, more control over the wavepacket dynamics as well as more detailed information on the molecule that can be used to reconstruct the relevant Hamiltonian. These are lines of investigation that will be followed in the rest of this chapter.



**Figure 4.4: Bulk vs. Single molecule approach.** a) Averaged response of 52 molecules compared to the theoretical prediction based on the bulk absorption spectrum. b) Result of the Fourier analysis of 52 single-molecule traces. Distributions and scatter plot of the main frequency component ( $f$ ) and its corresponding phase ( $\theta$ ). Marker size and bin width include the experimental errors.

Averaging the response of 52 investigated molecules returns the ensemble oscillation in excitation probability as a function of  $\Delta t$  (Fig. 4.4a). In spite of their smaller amplitude in comparison to single molecules, the ensemble oscillation is clearly visible owing to the higher signal to noise ratio, and shows a good agreement with theoretical WPI calculations based on the bulk absorption spectrum (Fig. 4.4a).

In order to quantify the differences in ultrafast single-molecule responses, we performed a Fourier analysis of the fluorescence intensity versus  $\Delta t$  traces for 52 single molecules, and determined the main frequency component ( $f$ ) and its corresponding phase ( $\theta$ ) (Fig. 4.4b). The frequencies range from roughly 20 to 45 THz (670 to 1,500  $\text{cm}^{-1}$ ), with a sharp peak around 32 THz (1,070  $\text{cm}^{-1}$ ), and are consistent with the energies of the vibrational bands observed for this molecule in bulk<sup>118</sup>. The distribution of frequencies reflects underlying variations in the energy and relative intensities of the vibrations for individual molecules. Analogous variations in the emission spectrum of single molecules have been ascribed to the influence of different local environments, in the form of varying dispersive interactions and structural constraints imposed by the polymer matrix<sup>15</sup>.

The broader distribution of phases indicates variations in the electronic excitation energy of the molecules. Phases ( $\theta$ ) ranging from 0 to  $2\pi$  are found, but the distribution is not uniform; it features a small peak, which causes the contrast in the ensemble fluorescence oscillation. This experiment already shows that the observation of ultrafast dynamics at the single-molecule level is feasible, and demonstrates its potential to discriminate between individual and ensemble-averaged responses. Moreover, comparison between Figs 4.2b and 4.4a shows an important feature of the single molecule vs the bulk approach: the fidelity of the wavepacket oscillation, i.e. the superposition state preparation, is

up to a factor of 4 greater in the single molecule approach, because inhomogeneous dephasing of the wavepacket, due to a wide range of vibrational energies and phases that statistically contribute to the superposition, does not occur, and only the homogeneous electronic dephasing  $\gamma_2^*$  (see chapter 3) plays a role.

The distributions of  $(f)$  and  $(\theta)$  provide tuning parameters for coherent control experiments: in other words, the pulse sequence to create a particular state can be adapted to a particular molecule, which is another aspect of the single molecule approach that gives advantage over the bulk approach. On the other hand, these distributions contain spectroscopic information:  $(\theta)$  provides information about the detuning of the excited state potential well, similar to  $(\delta)$  in chapter 3, whereas  $(f)$  directly maps vibrational frequencies. From the distribution in Fig. 4.4 no correlation between the two can be discerned from this particular experiment.

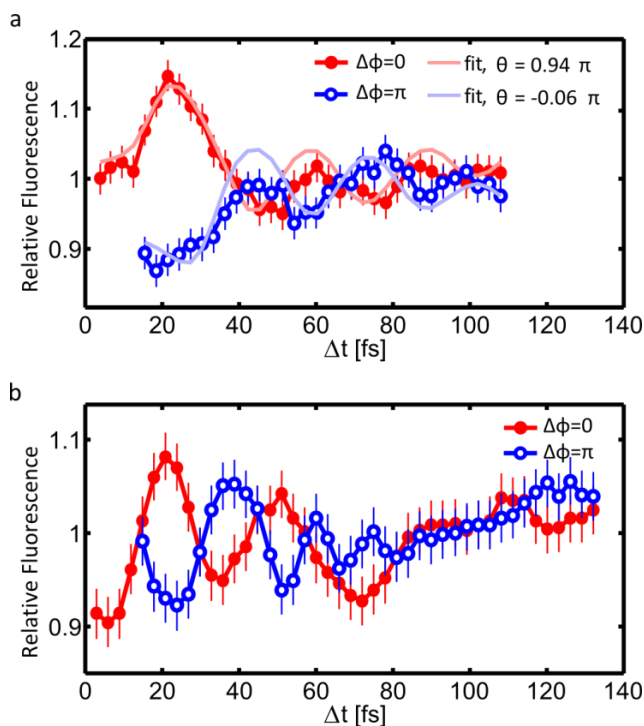


**Figure 4.5: Phase control of single-molecule wave packets.** Single-molecule fluorescence intensity as a function of the time delay between two in-phase ( $\Delta\phi=0$ ) and in-antiphase ( $\Delta\phi=\pi$ ) excitation pulses. The excitation intensity was constant for all  $(\Delta t, \Delta\phi)$  combinations except for the (excluded) points near zero delay with ( $\Delta\phi=\pi$ ). a) The fits to the ( $\Delta\phi=0$ ) and ( $\Delta\phi=\pi$ ) traces are based on the bulk absorption spectrum. Fourier analysis of the fits shows that  $f=31$  THz in both traces and the difference in  $\theta$  is  $\pi$ . b) Some molecules present fluctuations even for time delays  $\Delta t$  as long as 120 fs and with more than one frequency component. Error bars,  $\pm 1\sigma$ .

## 4.4 Phase control of wavepacket interference

One of the most important features of WPI is that the phase of the generated wave packet is determined by both the vibrational levels involved and the phase of the optical field. This interdependence of the optical and wave-packet phases is the basis for the coherent control of molecular states. A clear-cut experiment to target the phase dependence of WPI is a time-delayed two-pulse excitation scheme, where the pulses have a mutual phase shift of  $\pi$  rad<sup>173</sup>. We recorded the fluorescence of single molecules at each time delay  $\Delta t$  consecutively with the two pulses in phase ( $\Delta\phi=0$ ) and antiphase ( $\Delta\phi=\pi$ ). Two examples are shown in Figs 4.5a and b. Excitation with two pulses in phase, or with two pulses in antiphase, produces an inverted molecular response, in agreement with the expected inverse wave-packet interference. This is confirmed by fits based on the bulk absorption spectrum (Fig 4.5a): The lines in the bulk absorption spectrum are convoluted with Lorentzians with widths determined by dephasing  $\gamma_2^*$ ; the detunings, strengths and the widths of the lines are fit parameters. The best fits are determined by calculating the overlap between the resulting spectrum and the spectral shape of the delayed pulse for each delay time. The best fits for ( $\Delta\phi=0$ ) and ( $\Delta\phi=\pi$ ) are determined independently. Fourier analysis of the resulting best fits for ( $\Delta\phi=0$ ) and ( $\Delta\phi=\pi$ ) shows that the main frequency of the oscillations  $f_0=31$  THz in both cases and that the relative phase of the wavepacket oscillations differs by  $\pi$  radians ( $\theta_0(f_0)=0.94\pi$ ,  $\theta_\pi(f_0)=-0.06\pi$ ), confirming inverse wavepacket interference.

For some molecules with high photostability, we could detect WPI in the excitation probability for times as long as 120 fs, showing fluctuations that are more complex than a damped, single frequency oscillation (Fig 4.5b) In order to explore this complexity and investigate the limits of the fluorescence excitation enhancement and suppression achievable on a single molecule, we designed a multiple-pulse coherent excitation experiment. The idea is straightforward: as a wave packet propagates, its internal phase evolves with a certain phase velocity that depends on the amplitudes and phases of the vibrational states that are superimposed to form the wave packet. If one aims for maximum interference between two wave packets generated with a time delay  $\Delta t$ , a certain phase shift should be introduced in the second wave packet to compensate for the phase evolution of the first one. The resulting wave packet can then be made to interfere with subsequently launched wave packets to optimize state preparation.

In the experiment depicted here we used a train of four phase-locked pulses and varied  $\Delta t$  and  $\Delta\phi$  independently. In this way, for each individual molecule, we obtained a time–phase map of the photoexcitation probability that provides a direct view into the molecular coherent dynamics. We found that three and four pulses led to higher fidelity preparation of excited state superpositions, but that 5 pulses hardly gave rise to improvement. This can qualitatively be understood by looking at the dephasing times: the dephasing time for these organic systems at room temperature is near  $\sim 50$ -60 fs. (see chapter 3, decay times Figs. 4.3-3.5). Four 15 fs pulses therefore interact with the molecule within the dephasing

time while having a measurable mutual delay; later pulses will tend to interact with the molecule after dephasing and thus have no measurable effect.

We mapped the excitation probability as a function of  $\Delta t$  and  $\Delta\phi$  for a large number of molecules, and found a rich variety of coherent dynamics. Four examples are shown in Figs 4.6a-d. The influence of phase on the photoexcitation probability is evident. For any given delay, the opposite behaviour is observed for a phase shift of  $\pi$ . Diagonal bands of enhanced or suppressed photoexcitation probability can be seen. These are indications of the time-phase relation and clearly show how the wave-packet phase evolution can be followed by the optical field. The maximum enhancement or reduction of the excitation probability occurs for different combinations of delay and phase shift, depending on the molecule. When the excitation field is tailored to match the coherent dynamics of each molecule in its particular local environment, remarkably high degrees of control are achieved. Depending on the molecule, the control contrast (defined as the ratio of maximum to minimum excitation probability) ranges from 2.5 to as high as 4, which is approximately double that obtained with two pulses in phase or in antiphase (Figs 4.2 and 4.5) and up to 3 times higher than the contrast we measured in bulk (Fig 4.4).

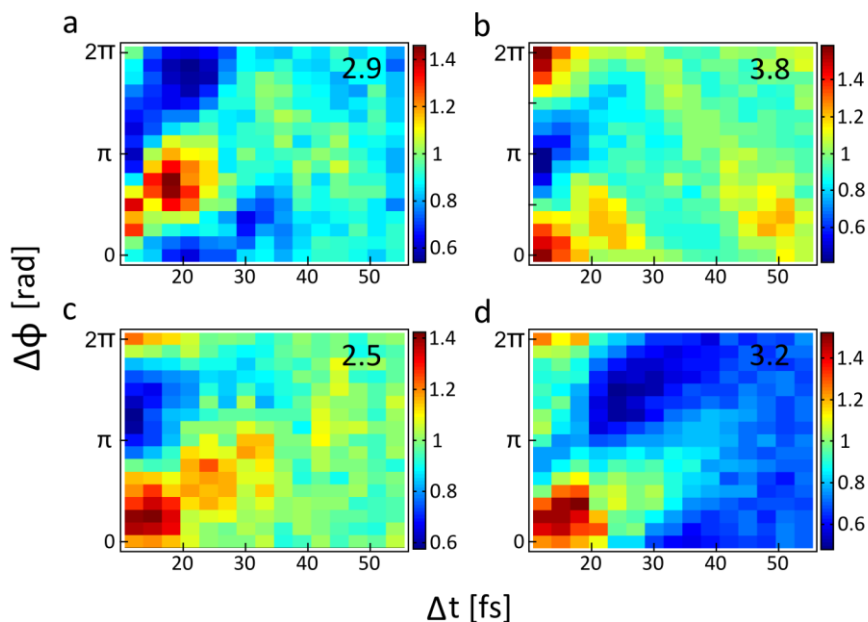


Figure 4.6: **Single-molecule time-phase coherent excitation maps.** a–d, Time-phase fluorescence excitation maps of four different molecules excited with a four-pulse sequence.  $\Delta t$  and  $\Delta\phi$  are the time delay and phase shift between each consecutive pulse in the sequence. The fluorescence intensity (colour scale) normalized to the average. The maximum/minimum ratio, that is, the contrast achievable through control of coherent excitation, is shown in the upper right corner of each plot.

Several features of these graphs merit further investigation in the context of Hamiltonian reconstruction. The  $\Delta\phi$ -offset of the diagonal bands (compare Figs 4a and 4b) is an indication of the detuning of the central laserwavelength and thus a measure of the  $S_0$ - $S_1$  energy gap. The periodicity of reemergence of maxima and minima (see e.g. Fig 4.6b) is indicative of the frequency of vibration and thus of the vibrational energy levels encompassed in the wavepacket. The decay in contrast in the figures for larger  $\Delta t$  (Figs 4.6a-d) is given by the electronic decoherence time  $T_2^*$ . The slope of the diagonal band of enhanced or suppressed fluorescence gives information about the dispersion of the wavepacket and thus on the shape of the excited state potential landscape.

## 4.5 Conclusions

The experiments presented in this chapter merge two of the most valuable experimental techniques of the past decades: ultrafast spectroscopy and single-molecule detection. They demonstrate that room-temperature coherent control experiments in ensembles are limited by intrinsic inhomogeneities, and at the same time provide the ultimate solution. The coherent dynamics of each molecule can be mapped at ambient conditions, and the excitation field can be tailored to obtain maximum control. We believe that this greatly extends the field of application and the potential of coherent control. Furthermore, expansion of the parameter set under investigation should allow higher fidelity state preparation and at the same time provide more information about the molecular potential landscape; this is work that will be continued outside the context of this thesis.

A definite advantage here would be the ability to extract stimulated signals from single molecules. Single molecules have recently been measured in absorption at room temperature<sup>5,6,8</sup>, utilizing photothermal contrast<sup>5</sup>, differential transmission measurements<sup>6</sup> and ground state depletion<sup>8</sup>. All these techniques however rely on the CW-lasers and overlap of the laser line with the largest molecular absorption line. For ultrafast measurements, pulses of 100 fs widths on dynamic timescales of 300 fs have been used to obtain stimulated emission signals of (extrapolated) 5-10 molecules<sup>9</sup>. The challenge in these measurements is optimization of the molecular signal over the inevitable shotnoise in background laser light, which will become progressively harder for higher order effects and shorter pulses. A push towards this goal is to be expected in the next years and would open the possibility of true 2D ultrafast spectroscopy on single molecules at room temperature. We note however that many features of 2D spectroscopy, i.e. the measurement of off-diagonal components of the density matrix, are in fact accommodated by the phaselock applied in our experiment: the technique developed in the past chapters therefore offers a viable alternative. Research into the similarities and differences between ultrafast phase-sensitive spectroscopy and 2D spectroscopy, and their relative merits, is therefore expected to continue in the future.

Finally, single-molecule detection offers the possibility of multi-parameter correlations, such as the relation between molecular conformation and function: this is work in progress. Investigations addressing coherent dynamics and

energy flow in complex systems and environments are among the possibilities. Examples include light-harvesting complexes, photo-active proteins, conjugated polymers and metallic or metal–organic hybrid nanostructures. The coming chapters will form an elaboration on this theme and see the techniques developed in the past chapter applied to the problem of complex, biological systems: chapter 5 will treat the work done in the context of this PhD on coherence in single photosynthetic light harvesting complexes, and chapter 6 will examine the possibilities of “artificial molecules”: asymmetric, coupled plasmonic systems, and their possibilities to bring ultrafast phase-sensitive spectroscopy to sub-diffraction limited resolution.

This work was partially published as  
Brinks et al., *Nature* **465**, 905-908 (2010),  
Brinks, Hildner, Stefani, van Hulst, *Faraday Discussions* **153**, 51 (2011)



**In this chapter we argue that the single molecule phaseshaping method can be used in the investigation of a high profile problem in biophysics: the role of quantum coherence in energy transfer in photosynthetic light harvesting complexes. We resolve the transfer between the B800 and B850 band in single LH2 complexes with a novel implementation of the phase shaping method and find that there is indeed electronic coherence between these bands that survives several times longer than would be expected from bulk measurements. Moreover, we see the coherence survive and readjust after changes in the molecule, demonstrating that it fulfills the requirements to play a key role in energy transfer under ambient conditions.**

**5. Quantum coherence persists in time-varying energy transfer in light-harvesting complexes**

## 5.1 Introduction

Quantummechanical effects in biological processes are intriguing and lively debated issues<sup>125,177–184</sup>. One biological mechanism meriting particular attention in this respect is photosynthesis. The initial steps of photosynthesis comprise the absorption of sunlight by pigment-protein complexes as well as funnelling of excitation energy to a reaction centre. This remarkably efficient excitation energy transfer is a key step in the initial light-driven processes in natural biochemistry and takes place in highly sophisticated supra-molecular assemblies, so called pigment-protein complexes<sup>185–188</sup>.

A particularly intriguing question, that emerged recently, concerns the impact of quantum coherence on promoting the efficiency and directionality of ultrafast energy transport in photosynthesis. As a consequence, much work has been devoted to mapping the energy transfer in light harvesting complexes, revealing the underlying mechanisms, and understanding the spatial and energetic organization of the pigment molecules involved<sup>71,185–211</sup>. One of the most versatile techniques applied to this end is 2-dimensional spectroscopy, which, through inducing higher order polarizabilities, can establish the energy levels in pigment protein complexes, determine their nature and quantify the coupling between them<sup>41</sup>. Utilizing 2D spectroscopy on ensembles of various light-harvesting complexes, oscillatory signatures of surprisingly long-lived coherences in energy transfer processes have been found<sup>83,84,123,124,209,212,213</sup>. Customarily, one of the axes of the 2D spectrum is then plotted in the time domain instead of the frequency domain, and the coupling between particular energy levels is theoretically discussed in terms of coherence, instead of coupling strength.

The theory that emerged to describe the aggregated data on energy transfer in light harvesting systems models the transfer process in terms of environmentally assisted quantum transport with a careful balance between coherence, dissipation, and dephasing<sup>214–217</sup>. This precarious equilibrium is influenced by temporal, spatial and spectral inter-complex variations, caused by the highly dynamic environments and broad conformational diversity in functioning bio-systems. Although the presence of this quantum effect is now generally accepted<sup>125</sup>, its nature (vibrational or electronic) is still unclear. Further open questions are, how nature designed light-harvesting antennas that can be robust against perturbations and thermal disorder under physiological conditions, and whether quantum coherent transport can help to optimise the energy flow despite the presence of disorder.

These issues are at the heart of the question whether quantum coherence plays a significant role in photosynthetic energy transfer, but owing to the large structural and electronic heterogeneity of photosynthetic antenna proteins<sup>218–221</sup> they are not testable by conventional femtosecond spectroscopy<sup>71,188,191,192,204</sup>. Hence, in order to unravel the nature of energy transfer in light-harvesting<sup>125,217</sup> it is crucial to probe the ultrafast response of antenna proteins beyond the ensemble average and to test the robustness of coherences against perturbations on the level of individual complexes<sup>85,86</sup>. Here, we address these questions by

employing a novel ultrafast single-molecule technique to a prototypical antenna protein, the light-harvesting 2 (LH2) complex from the purple bacterium *Rhodospseudomonas acidophila* (*Rps. acid.*). This assembly comprises in total 27 bacteriochlorophyll *a* (Bchl *a*) molecules, that are arranged in two concentric rings (Fig. 5.1a) giving rise to the characteristic near-infrared absorption bands (Fig. 5.1b) labelled, according to their absorption maxima, B800 (with 9 weakly coupled pigments) and B850 (with 18 strongly coupled Bchl *a*). Since the B800-B850 intra-complex transfer is governed by an elusive intermediate electronic coupling<sup>208,210</sup>, we are particularly interested in the role of quantum coherence in the transport between these energy eigenstates.

## 5.2 Experimental method

2D-spectroscopy is the method of choice to probe energy landscapes in bulk experiments: the driven transition of the quantum system between optically accessible states does very accurately map out the landscape of accessible states and the coupling (i.e. time constants of transfer) between them. However, this method is as yet not applicable to single molecule studies (despite the recent first observation of stimulated signals from below 10 molecules<sup>9</sup>) because it relies on a third-order polarizability ( $X^{(3)}$ ) and signals with this order of nonlinearity are as yet too weak from single molecules to resolve over the noise of a typical experiment. Moreover, a more fundamental issue with this method is the question whether processes induced by absorption from incoherent solar light, the intensity of which is typically far from the nonlinear regime, can accurately be mapped by a highly nonlinear process, induced by peak powers that are far higher than what these systems are usually exposed to; these may lead to e.g. exciton annihilation<sup>222</sup>. An extreme example of incompatibility in this respect are the recently uncovered indications of photoprotective mechanisms shutting down the energy transfer when the light harvesting systems are exposed to too high excitation powers<sup>223,224</sup>.

The challenge is therefore develop a method that i) is sensitive enough to resolve signals at the single molecule level, ii) does not trigger annihilation or protection mechanisms in the molecule and iii) is still sensitive to coherence between quantum states, i.e. preserves phase information.

Our experience with measurements of coherence in single molecules provides us with the tools to address this issue. For open molecular systems, i.e. molecular systems in contact with a bath, i.e. molecular systems in which dissipation takes place, weak field phase control is possible<sup>72,163,225–229</sup>; i.e. if the timescales of decay of coherence between quantum states, the pulsewidths used to create the coherence between those states, and dissipative transitions between non-coherently coupled states, take place at comparable timescales, the exact temporal shape of the excitation influences the state in which the quantum system ends up after excitation, even in the weak-field limit. (Note that a very

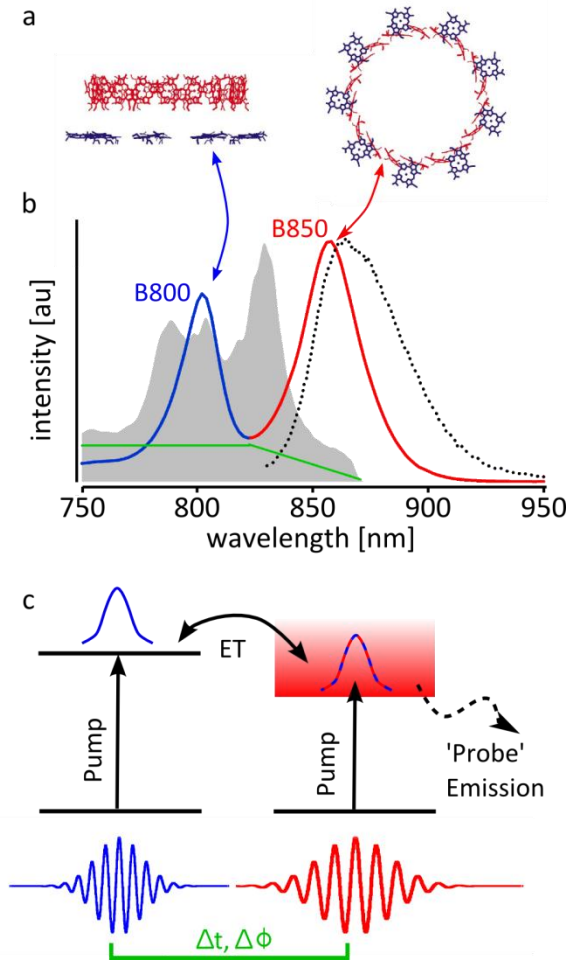


Figure 5.1: **Ultrafast phase-coherent excitation of individual LH2-complexes at room temperature.** a: Structural arrangement of the 27 bacteriochlorophyll *a* (Bchl *a*) pigments in the light-harvesting 2 (LH2) complex of the purple bacterium *Rps. acid*. (Protein Data Bank, code: 1kzu). The Bchl *a* molecules forming the B800 (B850) ring are depicted in blue (red). b: Ensemble absorption spectrum of LH2 with the characteristic near-infrared B800 (blue) and B850 bands (red) ; the emission spectrum of LH2 is shown as dotted line. The exciting laser spectrum is depicted in grey, and the green line represents the spectral phase function applied by a 4f-pulse shaper. c: Concept of the experiment: Single LH2 are excited by a 2-colour pulse pair with well-defined inter-pulse delay time ( $\Delta t$ ) and relative carrier envelope phase ( $\Delta\phi$ ), generated by applying the spectral phase function. The first pulse (blue) creates an excitation in the B800 band. After energy transfer (ET) to the B850 band the second time-delayed pulse (red), resonant with the B850 band, modulates the population transfer to the B850 excited states by quantum interference and thus changes the probe signal, the spontaneous emission from a single complex.

recent paper discusses the possibility of coherent control in the linear regime even without resorting to a system-bath dissipative interaction by positing that certain interactions qualify as a “normal” strong field effect<sup>227,230</sup> even though the power dependence is linear<sup>231</sup>).

Detection in this respect is complicated because we detect single molecule fluorescence, i.e. we measure the excited state population long after coherence has decayed. However, in chapters 3 and 4, we have shown that we have the capability to create and probe coherence between S0 and S1 electronic states<sup>86</sup> and between vibrational states in the S1-excited state potential well<sup>85</sup> in single organic molecules, using shaped pulses in the linear excitation regime. Here, the detection is based on a quasi pump-probe scheme that maps coherence to population (see chapters 3 and 4)<sup>41,44</sup>. In principle we therefore fulfil requirements i) and ii). For the phase sensitivity in this experiment a new excitation scheme is necessary however: we now probe coherence between two coupled electronic excited states and need a scheme that selectively detects this.

The weak-field phase control paradigm provides us with a scheme to fulfil this final requirement<sup>225</sup>. The B800-B850 transfer is a crossing between two electronic excited state potential wells. This type of process is sensitive to pure spectral phase in the weak-field limit, i.e. the spectral phase of the excitation influences the dynamics of the B800-B850 superposition<sup>43,44</sup> and thus the time-profile of the induced coherence between B800 and B850. Because the dynamics of the B800-B850 superposition, the decay of coherence and the dissipative transition to the lowest-lying fluorescent B850 states have similar time scales, the time-integrated B850 population depends on the temporal shape of the excitation field and we can try to design another quasi pump-probe experiment that maps the B800-B850 coherence to the B850 population<sup>72,86</sup>.

To study the femtosecond B800-B850 dynamics in single complexes, we therefore designed a specific 2-colour phase controlled pulse sequence, employing time-delayed transform limited pulses with different carrier frequencies that are resonant with the B800 and B850 bands of LH2, respectively (Fig. 5.1c), to function as the quasi pump-probe experiment. These pulses were sculpted from one broadband applying only spectral phase.

LH2 complexes were isolated and purified from membranes of *Rhodospseudomonas acidophila* strain 10050 (*Rps. acid.*) following solubilisation with the detergent lauryl dimethylamine-N-oxide (LDAO) as previously described<sup>232</sup>. To study individual complexes we mixed highly diluted LH2 in buffer (20 mM Tris/0.1% LDAO, pH8) with a poly(vinyl alcohol)-buffer solution (1.8% wt/wt). This solution was spincoated on cleaned microscope cover slips that were mounted on the piezo-stage of a sample-scanning inverted confocal microscope. The excitation source was a broadband mode-locked Ti:Sapphire laser (Octavius 85M, Menlo Systems) providing few-femtosecond pulses in the visible/near-infrared spectral region. We selected a 120 nm wide spectral band centred at 805 nm (Fig. 5.1b, grey spectrum), that covers the near-infrared absorption of LH2. This spectral band was compressed to the Fourier-limit of ca. 15 fs in the focus of the high-NA objective of our microscope (NA = 1.3, Fluor, Zeiss).

For pulse-compression and shaping we employed a double-pass 4f-shaper based on a spatial light modulator (adapted from MIIPS-box, Biophotonics Solutions Inc.). Pulse characterisation and dispersion compensation were carried out in the sample plane using the multi-photon intra-pulse interference phase scan (MIIPS)<sup>32,33,37,170</sup> method in a micrometric BBO crystal sliver. Importantly, we performed MIIPS in the sample plane, i.e. in the focus of our high-NA objective, to measure and correct the phase distortions introduced by all optical elements of our setup. Fig. 5.2a shows the laser spectrum (black) together with the residual spectral phase (red) that is measured after the compensation phase (i.e. the phase function compensating for the dispersion of the setup) was applied in the spatial-light modulator (SLM) of our pulse shaper. The residual phase is calculated from the signal trace (Fig. 5.2c) resulting from a MIIPS measurement<sup>37</sup>.

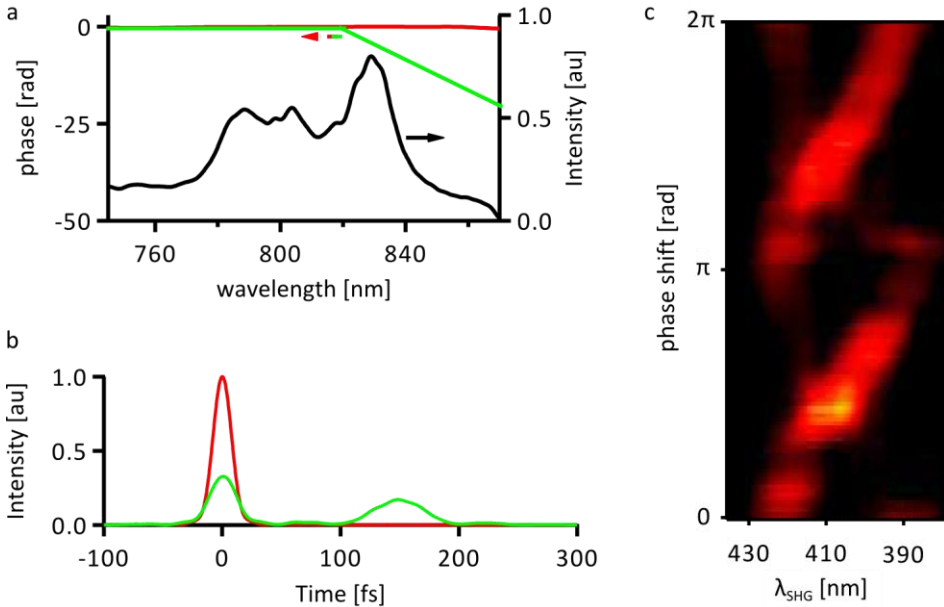


**Figure 5.2: Phase-locked 2 color pulse sequence created through pure phase shaping of the excitation pulse.** a) Laser spectrum (black), residual spectral phase (red) after compensation using MIIPS, and applied phase function to create the 2-colour time-delayed phase-controlled pulse pairs (green). b) Intensity envelope of a transform limited pulse (red) and a delayed pulse pair (green) with  $\Delta t = 155$  fs and  $\Delta\phi = 0$  rad applying the linear phase ramp for wavelengths longer than 820 nm. c) MIIPS trace of the fully compensated laser pulse.

The pulse sequences for the 2-colour phase-controlled experiments were generated by pure phase shaping: we applied a flat phase up to 820 nm and a linear phase ramp for wavelengths longer than 820 nm (Figs. 5.1b, 5.2a, green line), which shifts the corresponding spectral components in time without introducing higher order dispersion. This inversion point was chosen because it is the minimum between the B800 and B850 absorption peaks. The result is two transform-limited, time-delayed pulses with different carrier frequencies that are resonant with the B800 and B850 bands of LH2. Both the relative carrier envelope phase  $\Delta\phi$  and the time delay  $\Delta t$  between the pulses are fully controlled by the slope of the phase ramp, i.e. the spectral amplitude is the same for all pulse shapes and only the spectral phase is manipulated (Figs. 5.1b, 5.2a, green line). Fig. 5.2b depicts the transform limited laser pulse (red) that is obtained by applying the compensation phase in the SLM. The green curve represents a pulse pair with  $\Delta t = 155$  fs and  $\Delta f = 0$  rad, obtained by applying the linear phase ramp for wavelengths longer than 820 nm (green curve in Fig. 5.2a) on top of the compensation phase. Through the positioning of the inversion point, this scheme allows for the pump-probe scheme sketched in Fig. 5.1c

While this approach avoids spectral interference in the pulses itself, it means that  $\Delta\phi$  and  $\Delta t$  are not independent. However, this effect is negligible, because a phase change by  $2\pi$  shifts the delay only by less than 3 fs. The delay time is given by the derivative of the spectral phase with respect to the frequency, ( $\Delta t = \partial\Phi/\partial\omega$ ) and the relative carrier phase is expressed as the fractional part of the delay of the “red” sub-pulse divided by the period of the carrier frequency of the Fourier-limited pulse (period of the carrier frequency: 2.7 fs, corresponding to 805 nm,  $\Delta\phi = 2\pi \text{ frac}(v_{\text{carrier}}\Delta t)$ ).

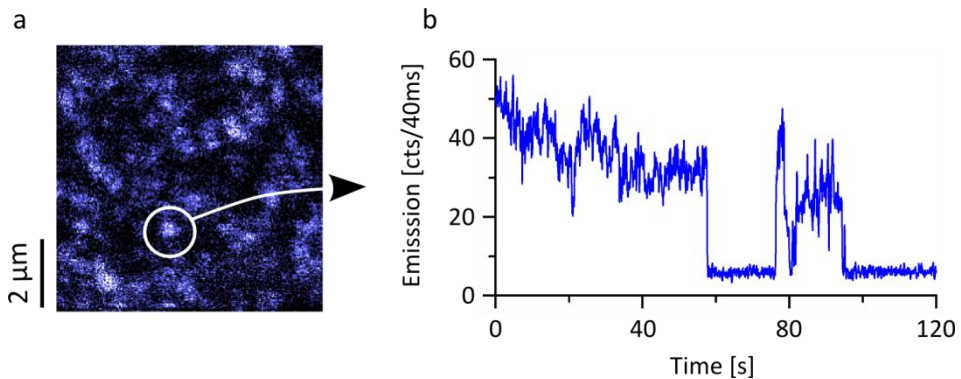


**Figure 5.3: Studying single LH2 complexes at room temperature.** a)  $7 \times 7 \mu\text{m}$  scan of a sample containing isolated LH2 with the emission intensity of individual aggregates being colour coded. b) The time-dependent fluorescence of the white circled single complex features fluctuations and digital “on-off” behaviour characteristic of a single multichromophoric system at room temperature. All experiments were carried out at room temperature under ambient conditions.

The 2-colour phase-controlled pulse pairs are then directed to a home-built confocal microscope and focussed onto single LH2-complexes (Fig. 5.3a). Their fluorescence is collected as a function of the pulse shape, separated from the excitation light by suitable dichroic beam splitters and dielectric filters, and detected by a single-photon counting avalanche photodiode (Perkin Elmer).

In our experimental design we took special care that the excitation power is constant for all delay times, and that the spectral amplitudes are not modulated by phase-shaping. The (time-averaged) excitation power was kept at a moderate level of about  $200 \text{ W/cm}^2$ , corresponding to less than 5 excitations per 100 laser pulses or  $8 \cdot 10^{12}$  photons/pulse/ $\text{cm}^2$ . This photon fluence is below the threshold for bimolecular annihilation processes in LH2<sup>222</sup> and also ensures that we are in the linear regime and neither excited state absorption nor stimulated emission occurs. Moreover, it prevents too rapid photobleaching. Nevertheless, single light-harvesting complexes feature non-discrete blinking and photobleaching on time scales of several seconds at room temperature (Fig. 5.3b). To discriminate such photoinduced emission changes from the effect of pulse-shaping on the fluorescence signal, we always recorded a reference signal between two shaped excitation pulses. The reference is the emission upon excitation with a single transform-limited pulse with the full 120 nm spectral band width. For the analysis we selected only traces where the reference signal was constant within the signal-to-noise ratio. The data points were determined from a different total number of photons (Figs. 5.4, 5.5:  $4 \cdot 10^3$ ; Figs. 5.8, 5.9:  $1 \cdot 10^3$ ), hence the shot noise level varies (1.5% resp. 3%). Together with laser power fluctuations below 3%, the total noise level of our data is then 3%, resp. 4%.

### 5.3 Persistent coherence in single LH2

In a first experiment we varied the delay time  $\Delta t$  while keeping the relative carrier envelope phase  $\Delta\phi$  constant by an appropriate choice of the spectral phase function. Individual LH2-complexes feature strikingly pronounced oscillations in their emission as a function of  $\Delta t$  up to at least 400 fs, as shown for two representative examples in Figs. 5.4a,b. Although both complexes exhibit oscillation periods of around 200 fs and contrasts of about 15 % (ratio between maximum and minimum signal), there are clear differences in their ultrafast response. This demonstrates the strong heterogeneity between complexes caused by large structural and electronic disorder, which has a substantial impact on the specific femtosecond B800-B850 intra-complex dynamics but is typically hidden in ensemble experiments.

The choice of phase shape in our experiment allows an intuitive interpretation of the observed oscillations in terms of two excitation pathways provided by the two pulses, as also sketched in Fig 5.1c. We attribute the observed oscillations in Figs. 5.4 to quantum interference between two pathways that populate the same target state, the emitting lowest-energy B850 level. Single complexes are first excited with a broadband “blue” pulse ( $\Delta t > 0$ ), that is resonant with the B800 band, and thus creates an excitation in this band.

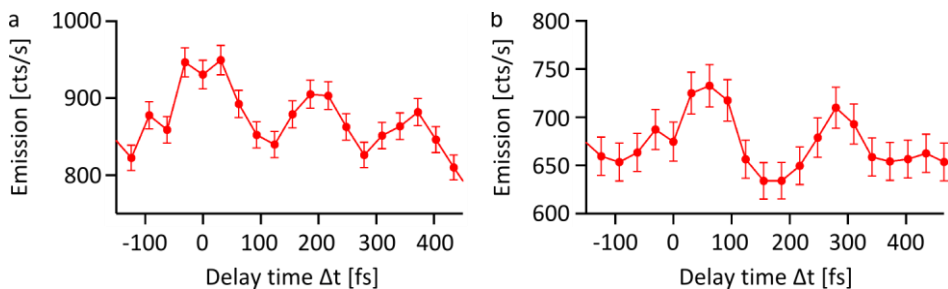


Figure 5.4: **Coherent B800-B850 energy transfer dynamics in single LH2-complexes.** a,b) Emission of single LH2-complexes as a function of the inter-pulse delay time with constant relative carrier envelope phase, demonstrating coherent population oscillations between B800 and B850 bands with very long coherence times of hundreds of femtoseconds. Error bars:  $\pm 1$  s.d.

This excitation evolves under field-free conditions during the time interval  $\Delta t$ . In particular, electronic coupling mixes B800 and B850 states and the total wave function can be expressed as  $|\psi(t)\rangle = c_{\text{B800}}(t)|\psi_{\text{B800}}\rangle + c_{\text{B850}}(t)|\psi_{\text{B850}}\rangle$ , i.e. a time-dependent coherence between B800 and B850 is induced. The delayed “red” pulse will then either enhance or reduce population transfer to the B850 excited states by quantum interference. This effect depends on the survival time of the quantum coherence as well as on the precise timing and the accumulated phase of the excitation after relaxation to optically allowed low-energy B850 exciton states. In contrast, if the electronic coherence between B800 and B850 decayed rapidly within ca. 50 fs, as usually expected for a disordered system at room temperature, we would observe a constant emission as a function of  $\Delta t$ , except for a short interval  $\Delta t \leq 50$  fs where phase memory is present<sup>86</sup>.

Alternatively, the observed oscillations in the delay traces in Figs. 5.3 may be thought to arise from vibrational wave packet interference of low-energy 160  $\text{cm}^{-1}$  vibrations. However, we discard this interpretation, despite the presence of Bchl *a* vibrational modes in this energy range<sup>233</sup>, because the electron phonon coupling in LH2 is very weak (see Table 5.1) as evidenced by bulk experiments, where only very small modulations of the transient electronic response by vibrational coherences are observed<sup>123,188,234,235</sup>.

Such subtle effects can hardly be discerned in single-molecule experiments with comparably low signal-to-noise ratios: they are in the range of our noise and several times smaller than the effects observed. Further, low-temperature single-molecule and hole-burning spectroscopy revealed only a single phonon mode with about 30  $\text{cm}^{-1}$  energy and significant coupling strength to the optical transition (Huang-Rhys parameter of  $S \sim 0.5$ )<sup>192,236</sup>. Accordingly, in time-domain experiments the oscillation period would be longer than 1 picosecond, which is clearly outside the range of oscillation periods found here.

Energy <sup>a</sup> / cm <sup>-1</sup>	<i>S</i>	Energy <sup>b</sup> / cm <sup>-1</sup>	<i>S</i>
166	0.01	84	0.027
194	0.01	117	0.013
342	0.01	177	0.036
379	0.01	212	0.028
564	0.01	332	0.013
727	0.05	355	0.01
773	0.05	384	0.013
879	0.05	464	0.005
917	0.05	569	0.011
950	0.05	682	0.014
		731	0.031
		761	0.006
		892	0.027
		1002	0.02
		1114	0.014
		1165	0.033
		1535	0.017

<sup>a</sup> taken from N. R. S. Reddy et al., Chem. Phys. Lett. **181**, 391 (1991) and T. Pullerits et al., J. Phys. Chem. B **101**, 10560 (1997).

<sup>b</sup> taken from N. J. Cherepy et al., J. Phys. Chem. B **101**, 3250 (1997).

**Table 5.1: Energies and coupling strengths (Huang-Rhys parameters *S*) of vibrational modes coupling to Bchl a.**

To test this we performed a control experiment on the B800 band only, encompassing its zero-phonon level and vibrational sidebands. For this measurement we limited the laser wavelengths to the 740 – 825 nm band, i.e. we cut laser wavelengths longer than 825 nm. Thus we are only resonant with B800 states and possibly optically allowed higher B850 exciton levels and/or vibrational modes coupling to both B800 and B850. The linear phase ramp was applied to wavelengths longer than 800 nm to shift these spectral components in time, while keeping the relative carrier envelope phase constant. For wavelengths shorter than 800 nm the applied phase function was flat. Hence the first pulse excites into the high energy tail of B800, while the second time-delayed pulse is resonant with the low-energy tail of this band. If vibrational coherences were measured in these data, we should observe an oscillatory response of the emission signal as a function of the inter-pulse delay time, with

the oscillation period reflecting the energy of the vibrational mode coupling to the electronic transition<sup>85</sup>, similar to the results from Fig. 5.4.

However, as evident from Fig. 5.5 (red symbols) we record a flat trace upon shaped excitation, which is basically identical to the reference trace for this complex (black symbols). This data rules out contributions of vibrational coherences to our experiments.

Consequently, the persistent oscillations in the delay traces are a clear signature that excitonic quantum coherences between B800 and B850 survive surprisingly long, at least 400 fs, in individual LH2-complexes under physiological conditions. Similar quantum effects have been reported by among others Lee et al., Harel et al. and Wong et al. who observed excitonic coherences between electronic states in light-harvesting antenna proteins by ensemble photon-echo methods<sup>123,209,213</sup>.

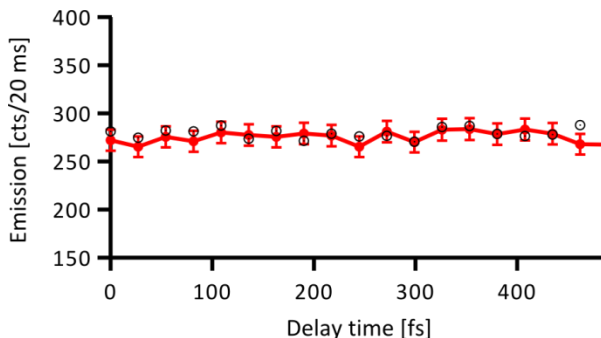


Figure 5.5: **Insensitivity of the experiment to vibrations in LH2.** Emission of a single LH2-complex as a function of the inter-pulse delay time with constant relative carrier envelope phase (red symbols). This experiment was set up similar to those shown in Fig. 5.4, but here only laser wavelengths resonant with B800 were employed (wavelengths > 825 nm were cut out). The black symbols represent the reference trace, i.e. excitation with a transform-limited pulse encompassing the entire spectral band (740 – 825 nm) of the laser.

## 5.4 B800-B850 inter-band energy transfer in LH2

To quantify the ultrafast B800-B850 intra-complex energy transfer dynamics we retrieved the oscillation periods  $T$  and the relaxation times  $\tau_{\text{rel}}$  (defined as the temporal position of the first maximum of the emission in the delay traces at  $\Delta t > 0$  fs) from data as depicted in Fig. 5.4. The resulting histograms, presented in Fig. 5.6, feature a wide distribution of periods between 140 and 400 fs with a maximum near 200 fs. Even more strikingly, they give a bimodal distribution of relaxation times. The broad spread in  $T$  and  $\tau_{\text{rel}}$  is caused by the heterogeneous local dielectric protein environment<sup>211</sup> giving rise to large structural and electronic disorder from complex to complex, corresponding to similar influence of heterogeneous polymer matrices on the steady state<sup>15</sup> and ultrafast<sup>85</sup> properties of single organic molecules.

As the B800-B850 dynamics depends on the site energies as well as on subtle details of mutual orientations and distances of the involved pigments, i.e. on their particular electronic couplings, this implies that each complex features a distinct transfer pathway characterized by the period  $T$  and the relaxation time  $\tau_{\text{rel}}$ . An analytical treatment of the B800-B850 interband-energy transfer can help to resolve this heterogeneity and give insight into different energy transfer pathways. Moreover, for coherent dynamics the B800-B850 electronic coupling  $J$  can be related to the measured periods  $T$ , which will give us a handle on comparing our results with ensemble experiments and theory<sup>192,199</sup>.

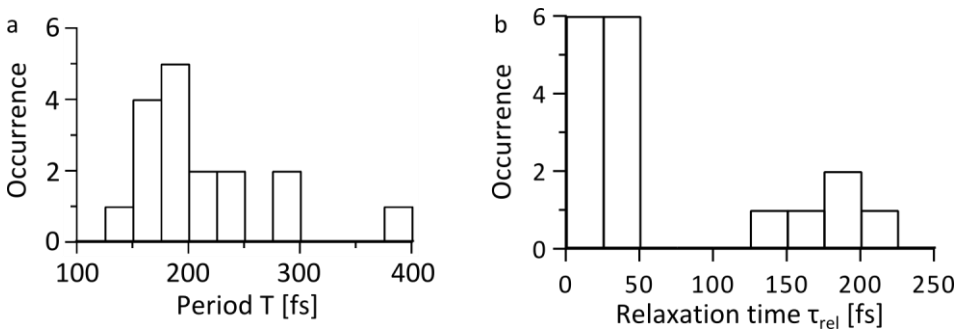


Figure 5.6: **Energy transfer pathways in single LH2-complexes.** a) Histogram of the oscillation period  $T$  retrieved from traces as shown in Figs. 5.4, 5.7. b) Histogram of relaxation times, i.e. of the first maximum of emission for  $\Delta t > 0$ , retrieved from delay traces as depicted in Figs. 5.4, 5.7

A thorough treatment of the B800-B850 dynamics is very challenging, as it takes place in the intermediate electronic coupling regime<sup>187,188,192,199,205,237</sup>, and LH2 is a rather complex multichromophoric system. An in-depth treatment is therefore beyond the scope of our work, and we have provided the intuitive pictures of weak-field phase control and quantum interference to explain our results. However, to illustrate the relevant processes that give rise to the oscillatory features in our data, we outline an analytical, though still simplified description in the following:

We consider the situation, in which our first (“blue”, “B800”) pulse is only resonant with B800, while the second delayed (“red”, “B850”) pulse is resonant with B850 states (a second scheme, where the first pulse excites optically allowed higher B850-states, as discussed in detail below, follows straightforwardly). We stress that this model is not meant to be exhaustive but to provide a simplified theoretical description of the effects measured in our experiment. To this end, we model the excitation scheme as two rectangular pulses with widths  $\tau_{B800}$  and  $\tau_{B850}$ , respectively, a delay time  $\Delta t$  between the pulse centers and a well defined carrier envelope phase difference  $\Delta\phi$  between the pulses.

The first, “blue” pulse creates population probability in B800 (essentially on monomeric Bchl *a* pigments owing to the low excitation powers). The expansion coefficient for a two-level system after interaction with a short laser pulse reads<sup>43</sup>

$$c_{B800} = -\frac{i}{2\hbar} \mu_{B800} E_{B800} \tau_{B800} \quad (5.1)$$

Note that this is a time-integrated value expressing the effect of the total interaction with the B800 pulse. We assume for simplicity a rectangular pulse shape with peak amplitude  $E_{B800}$  and pulse width  $\tau_{B800}$ ;  $\mu_{B800}$  is the transition dipole moment of Bchl *a* from the B800 pigment pool. Due to the electronic coupling  $J$  between B800 and B850 these energy eigenstates get mixed, which is expressed by the total wave function

$$|\Psi\rangle = c_{B800}(t)|\psi_{B800}\rangle + c_{B850}(t)|\psi_{B850}\rangle \quad (5.2)$$

The square magnitudes of the coefficients  $c_X(t)$  are referred to as populations, while mixed terms are called coherences. After interaction of the complex with the B800 pulse, a non-stationary superposition between B800 and B850 develops under field free conditions during the delay time  $\Delta t$ . The time-dependent B850 coefficient is – for two coupled two-level systems – given by<sup>44</sup>

$$c_{B850}(t) = -i \frac{J}{\Omega} \sin\left(\frac{\Omega t}{\hbar}\right) \exp\left(-i \frac{\delta t}{2\hbar}\right) \cdot \frac{1}{2\hbar} \mu_{B800} E_{B800} \tau_{B800}, \quad (5.3)$$

With  $\delta$  being the energy detuning between the B800 and B850 levels involved in this step, and  $\Omega$  is an energy defined by:

$$\Omega = \frac{1}{2}(\delta^2 + 4J^2)^{1/2}. \quad (5.4)$$

We stress that in terms of single-molecule experiments all processes are probabilistic, i.e. there is a finite probability of exciting B800 given by  $|c_{B800}|^2$ , and this excitation has a finite probability to oscillate to B850 according to eq. (5.3). Once in B850, there is a finite probability to oscillate back to B800 (case i) and to relax within the B850 band to lower energy optically allowed states (case ii), where interaction with the red B850 pulse takes place.

In case (i) the second (B850) pulse simply adds population probability to the B850 excited state without any interference effect, i.e. the total population probability of the coupled system after both pulses is  $|c_{B800}|^2 + |c'_{B850}|^2$ , with  $c'_{B850}$  being given by an equivalent expression as eq. (5.1), i.e.

$$|c_{incoh}|^2 = |c_{B800}|^2 + |c'_{B850}|^2 = \frac{1}{4\hbar^2} \left( \begin{aligned} & [\mu_{B800} E_{B800} \tau_{B800}]^2 \\ & + [\mu_{B850} E_{B850} \tau_{B850}]^2 \end{aligned} \right) \quad (5.5)$$

Here  $\tau_{B800}$  is the width of the B800 pulse, and  $\tau_{B850}$  is the width of the B850 pulse. This situation corresponds to incoherent two-pulse excitation, where the phase between two pulses is irrelevant, and gives the baseline of our measurement.

In case (ii) intra-B850 relaxation may induce a phase shift  $e^{i\zeta}$  in the coefficient  $c_{B850}(t)$  before interaction with the second pulse. Additionally we have to account for the well-defined carrier envelope phase difference  $\Delta\phi$  between both pulses. Equation (5.3) gives an expression for the development of the B800 excitation under field-free conditions. This condition lasts for the delay time  $\Delta t$  between the B800 and the B850 pulse, after which interaction with the “red” B850 pulse occurs. Hence the B850 coefficient after relaxation and after interaction with the second pulse may be written as:

$$\begin{aligned} c_{B850}(\Delta t) = & -i \frac{J}{\Omega} \sin\left(\frac{\Omega \Delta t}{\hbar}\right) \exp\left(-i \frac{\delta \Delta t}{2\hbar}\right) e^{i\zeta} \frac{1}{2\hbar} \mu_{B800} E_{B800} \tau_{B800} \\ & - \frac{i}{2\hbar} \mu_{B850} E_{B850} \tau_{B850} e^{-i\Delta\phi}. \end{aligned} \quad (5.6)$$

Here  $\tau_{B800}$  is the width of the B800 pulse,  $\tau_{B850}$  is the width of the B850 pulse and  $\Delta t$  is the delay between the pulses. This excitation scheme gives rise to an interference between the excitations created by the first and second pulse, and thus the oscillation on top of the baseline of our measurement (equation 5.5). This is immediately clear from expression (5.6) if written in terms of the total B850 population  $|c_{B850}|^2$  after interaction with both pulses:

$$|c_{B850}(\Delta t)|^2 = \left(\frac{J}{\Omega}\right)^2 \sin^2\left(\frac{\Omega}{\hbar}\Delta t\right) \frac{1}{4}(\omega_{B800}\tau_{B800})^2 + \frac{1}{4}(\omega_{B850}\tau_{B850})^2 + \frac{J}{2\Omega} \sin\left(\frac{\Omega}{\hbar}\Delta t\right) \omega_{B800}\tau_{B800} \cdot \omega_{B850}\tau_{B850} \cos\left(-\frac{\delta}{2\hbar}\Delta t + \zeta + \Delta\phi\right). \quad (5.7)$$

Here, a ‘‘Rabi-frequency’’  $\omega_{B800} = \mu_{B800} \cdot E_{B800} / \hbar$  has been introduced for brevity. The first two terms of the sum in (5.7) represent the population transferred from B800 (induced by the first pulse) and direct B850 excitation by the second pulse, respectively. The last term reflects interference between these two excitation pathways.

Note that this is the time integrated expression for the B850 population after interaction with both pulses. The excitation oscillation between B800 and B850 will continue until complete dephasing of the coherence between them, with the expansion coefficient  $c_{B850}(t > \Delta t)$  given by

$$c_{B850}(\tau') = \left[\cos\left(\frac{\Omega\tau'}{\hbar}\right) - i\frac{\delta}{2\Omega} \sin\left(\frac{\Omega\tau'}{\hbar}\right)\right] \exp\left(-i\frac{\delta\tau'}{2\hbar}\right) c_{B850}(\Delta t) \quad (5.8)$$

where  $\tau' = t - \Delta t$  and in principle a dedicated phase value should be added to every term containing  $\tau'$  to account for phase continuity between  $t < \Delta t$  and  $t > \Delta t$ . Because we are looking at the fluorescence, i.e. the excited state population at  $t \rightarrow \infty$  this oscillation integrates out and does not influence our signal anymore. In other words, it does not influence the total population in the excited state of the complex anymore, which is now given by

$$|c_{tot}|^2 = |c_{incoh}|^2 + \frac{J}{2\Omega} \sin\left(\frac{\Omega}{\hbar}\Delta t\right) \omega_{B800}\tau_{B800} \cdot \omega_{B850}\tau_{B850} \cos\left(-\frac{\delta}{2\hbar}\Delta t + \zeta + \Delta\phi\right) \quad (5.9)$$

For  $t \rightarrow \infty$  the total population in the excited state will relax to the lowest lying B850 state, from which it will decay to the groundstate, giving fluorescence. Our signal is therefore directly proportional to eq. (5.9) and now depends straightforwardly on our experimental variables  $\Delta t$  and  $\Delta\phi$ . This allows us to probe the phase shift  $\zeta$  that is introduced by the B800-B850 transfer.

Equation (5.9) can now be directly compared with our experimental traces. The oscillatory traces shown in Fig. 5.4 and Fig. 5.7 have been recorded by changing the delay time between the pulses while keeping their phase difference constant. Hence, the oscillations may come either from the sine or the cosine term in eq. (5.9) and the oscillation period is strongly determined by both  $\delta$  and  $J$ . On the one hand, a limiting value for  $\delta$  is the energy difference between B800 and B850 bands,  $\delta = 870 \text{ cm}^{-1}$ , whereas  $J$  is of the order of some ten  $\text{cm}^{-1}$ .<sup>(187,192,199,205)</sup> Hence, from eq. (5.4) it follows  $\Omega \approx 0.5 \cdot \delta$  and  $J/\Omega = 0.1$ . This gives an oscillatory behaviour according to (neglecting the constant factors that are typically all of the same order of magnitude)

$$\frac{J}{2\Omega} \sin\left(\frac{\delta}{2\hbar} t\right) \cdot \cos\left(\frac{\delta}{2\hbar} t - \zeta - \Delta\phi\right) \quad (5.10)$$

A simple trigonometric equality then tells us this is a single oscillation with a frequency given by  $\delta$ , i.e. a period of 40 – 50 fs. The value for delta is an upper limit here, giving an upper limit on the frequency and thus a lower limit on the period; it also provides a lower limit for the amplitude of the oscillations of about 2.5%. These values deviate significantly from the ones measured in our experiment, indicating we are not in this limiting case.

If, on the other hand,  $\delta$  and  $J$  are of the same order of magnitude,  $\Omega \approx \sqrt{5/2} J \approx \sqrt{5/2} \delta$  and the oscillatory B800-B850 dynamics reads approximately:

$$\frac{1}{\sqrt{5}} \sin\left(\frac{\Omega}{\hbar} t\right) \cdot \cos\left(\frac{\Omega}{2\hbar} t - \zeta - \Delta\phi\right). \quad (5.11)$$

The trigonometric equality

$$\begin{aligned} \sin(\Omega t) \cos(\Omega t / 2) &= 0.5[\sin(3\Omega t / 2) + \sin(\Omega t / 2)] \\ &= 0.5[\sin(2\Omega t) \cos(\Omega t / 2) + \sin^2(\Omega t) \sin(\Omega t / 2)] \end{aligned} \quad (5.12)$$

tells us that this gives an oscillation with frequency components  $\Omega/2$  and  $3\Omega/2$ . However, fits to the first few periods of this equation typically converge to  $2\Omega$  because of the second part of the equality, showing that the trace has oscillation components at  $2\Omega$ , modulated by a slower oscillation at  $\Omega/2$ ; the frequency content of our measurements typically mimics the second part of the equality because we resolve only a few periods in the oscillation due to the limited time of the measurements and coherence dephasing.

This yields oscillations with initial amplitudes of about 20% ( $[2\sqrt{5}]^{-1}$ ) as observed in our experiment. For the electronic coupling  $J$ , values between 30  $\text{cm}^{-1}$  and 80  $\text{cm}^{-1}$  are reported in the literature<sup>187,192,199,205</sup>. Using eq. (5.4) and inserting these limiting numbers into expression (5.11) then yields oscillatory traces with a period of 200 fs for a rather small detuning between  $\delta = 155 \text{ cm}^{-1}$  and 45  $\text{cm}^{-1}$ , for oscillations dominated by  $2\Omega$ . (if the 200 fs oscillations were dominated by  $1.5\Omega$  and for the given limits of  $J$ ,  $154 \text{ cm}^{-1} < \delta < 214 \text{ cm}^{-1}$ ).

Hence, our data indicate that a contribution to the ultrafast coherent B800-B850 dynamics comes from optically dark or very weakly optically allowed B850 states ( $\delta \ll 870 \text{ cm}^{-1}$ ), that are near-resonant with B800. Based on this treatment, our data are consistent with  $J \leq 80 \text{ cm}^{-1}$  on average, which is in agreement with ensemble experiments and theory<sup>192,199</sup>.

We note again that the precise B800-B850 transfer mechanism is not clear as yet, e.g. it is unknown, which levels are involved, and thus the precise detuning is not accessible. The strongly delocalized nature of B850 states has to be taken into account for a thorough description. Our treatment reflects only a simplified approach intended to give a basic idea of the involved processes. For completeness we also note that this theory does not cover the question to which extent the B800 and B850 ground states are coupled or shared, but that this does

not matter in the weak field limit where we perform our experiment, i.e. where the population depletion from the ground state is negligible.

From eqs. (5.6), (5.7) and (5.9) it is clear that quantum interference can only occur if the initially created excitation (by the “blue” pulse) has relaxed to lower B850 exciton states that carry oscillator strength, i.e. for which  $\mu_{B850} \neq 0$ . The time constant of this first transfer and relaxation step after excitation corresponds to the point in time when constructive quantum interference occurred for the first time, and can be retrieved from the temporal position of the first maximum of the emission in the delay traces at  $\Delta t > 0$  fs (see Fig. 5.4 and 5.6b). The histogram obtained from our data is depicted in Fig. 5.6b, and allows to gain some insights into these fast processes in single LH2-complexes. The distribution is bimodal with a peak below 50 fs and a second maximum around 180 fs, further demonstrating the large inter-complex electronic disorder.

The slow 180 fs component is in accordance with the picture described above. The first step in the oscillation is a B800-B850 transfer: the “blue” pulse is only resonant with the B800 band and creates an excitation in this band, which oscillates to the B850 manifold, relaxes to lower-energy B850 exciton states and finally interacts with the delayed “red” pulse. The reported B800-B850 transfer times from our measurements, i.e. oscillation periods of up to 400 fs, thus fit to interference delayed up to  $\sim 200$  fs, i.e. half an oscillation period.

The fast component in the histogram is ascribed to a sub-population of LH2-complexes featuring optically allowed high-energy (“hot”) B850 states. Early single-molecule studies revealed that ca. 40 % of LH2 from *Rps. acidophila* possess higher lying absorptions between 830 and 850 nm identified as  $k = \pm 3$  B850 exciton states<sup>238,239</sup>. If a complex does have such optically accessible hot B850 states, the “blue” pulse can interact with both B800 and hot B850 states. Three excitation pathways towards population of the lower-lying B850 states are then possible:

- i. Excitation into B800 states, followed by coherent (back and forth) dynamics to B850 states, with final relaxation to bottom B850 states, as discussed above.
- ii. Direct excitation into hot B850 states, followed by (back and forth) dynamics to B800 levels.
- iii. Direct excitation into hot B850 states without substantial interaction with the B800 band, followed by rapid relaxation to lower lying B850 states, which takes place within a few 10 fs<sup>188,234</sup>.

The exact shape of delay traces from molecules featuring optically allowed hot B850 states is therefore determined by the precise B800-B850 electronic coupling, the corresponding site energies and the overlap of hot B850 states with the “blue” pulse excitation spectrum. The relative probability of pathways (i) and (ii) is influenced by the specific electronic structure, particularly by the presence of optically allowed higher B850 states, and will give rise to many possible shapes for the oscillatory traces. While pathway (i) has been discussed in detail above, the presence of excitations that are dominated by pathway (ii) is verified by the observation of oscillatory features at delay times  $\Delta t < 0$  fs for some complexes (Fig. 5.7): upon initial “red” B850 excitation the created electronic wave packet can coherently oscillate to B800 states and interaction

with the “blue” pulse gives then rise to quantum interference. Excitations dominated by (iii) would not appear in our histograms, since intra-B850 relaxation is so fast that a complete transfer cycle (i.e. an oscillation in the delay trace) is unlikely to happen. For delay traces without oscillations we can presently not distinguish between molecules where the coherence decays so fast that only incoherent transfer takes place, or the relaxation into lower lying B850 is so fast that B800-B850 transfer cannot take place.

The peak in the histogram below 50 fs (Fig. 5.6b) thus represents molecules that do feature optically-accessible hot B850 states, whereas the peak at 180 fs comes from complexes without such states. Revealing sub-populations from the fast component in Fig. 5.6b is still work in progress.

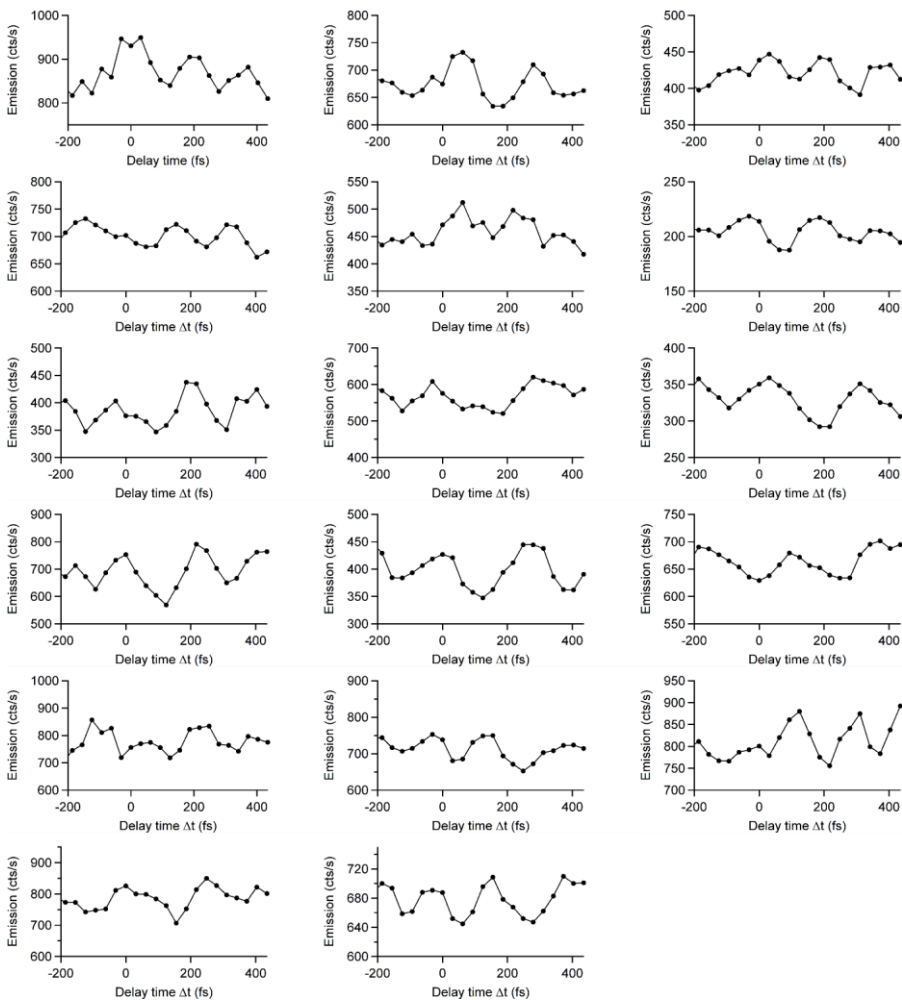


Figure 5.7: **Raw delay traces from 17 individual LH2-complexes.** The left and middle traces in the top row are shown in Fig. 5.4.

## 5.5 Coherence mediates robust energy transfer under external perturbation

Long-lived quantum coherences evidently contribute to the very fast and efficient transfer dynamics in individual complexes. A crucial question concerns the role of coherence in the robustness of energy transport against external perturbations, which modify the electronic couplings between pigments on slow (seconds) time scales. To investigate this issue we resolved phase changes in the energy transfer by recording the fluorescence of individual complexes as a function of the relative carrier envelope phase  $\Delta\phi$  at constant  $\Delta t$ . The delay time is chosen to be longer than 100 fs to avoid pulse-overlap effects, but well below 400 fs to be still in the coherent regime.

The result of this phase-cycling approach is presented in Fig. 5.8 (red symbols) featuring a full sinusoidal period of the emission upon a relative phase change by more than  $2\pi$  at a delay time of  $\Delta t = 150$  fs. Comparison with the reference signal from the same complex, taken with a Fourier-limited pulse encompassing the full laser spectrum (Fig. 5.8, open black circles), shows that the excitation probability is enhanced (reduced) by 15 % for a relative phase of about  $0.5\pi$  ( $1.5\pi$ ). This observation demonstrates weak-field phase-control of the quantum interference between the excitation pathways to the B800 and B850 excited states; or in other words, this demonstrates phase control of the efficiency of the coherent contribution to the functionally important B800-B850 transfer pathway. Such efficient phase control indicates that the B800-B850 population transfer<sup>187,188</sup> is comparable to the time scale for dissipative interactions with the local (protein) bath<sup>72,228</sup>.

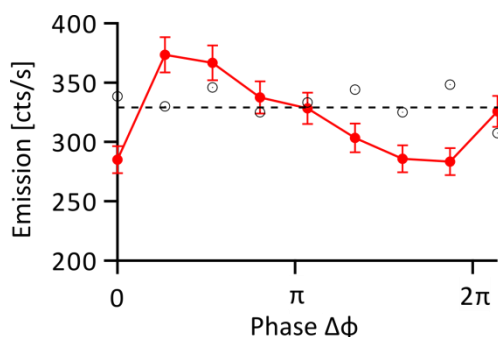


Figure 5.8: **Coherent phase control of the population transfer to the excited states of a single LH2-ring.** Fluorescence signal of a single LH2-complex as a function of the relative carrier envelope phase  $\Delta\phi$  at a constant inter-pulse delay time of  $\Delta t = 150$  fs (red). The emission features a 15 % enhancement (reduction) compared with the reference signal (open black symbols), i.e. the emission upon excitation with a single transform-limited pulse covering the entire 120 nm spectral band width. Error bars:  $\pm 1$  s.d

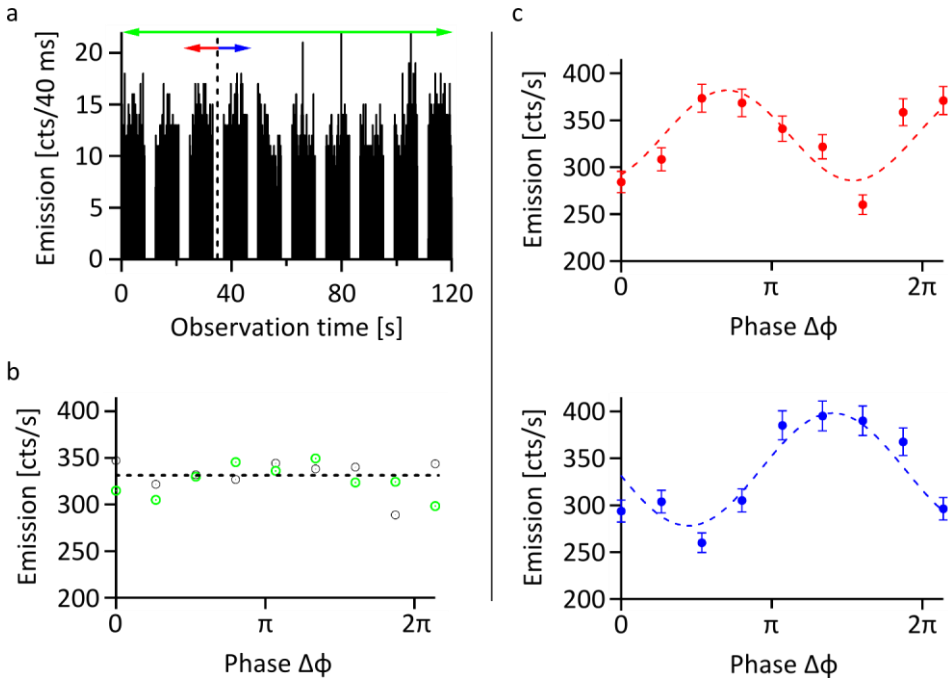


Figure 5.9: **Time-varying coherent energy transfer pathways.** a) Raw data from a single LH2-complex as a function of observation time: each block represents a phase scan from 0 to  $2\pi$  at a constant delay  $\Delta t = 100$  fs, interleaved with reference measurements using a single Fourier-limited pulse. b) Reference signal (black symbols) and LH2-emission as a function of  $\Delta\phi$  temporally averaged over all ten raw data blocks (green symbols). The dashed line is a guide to the eye representing the average signal. c) Phase-dependence of the LH2-emission averaged over the blocks left (red dots, top) and right (blue dots, bottom) to the dashed line in a. Only blocks with a constant reference signal were considered. The red and blue dashed lines are cosine-fits to the corresponding data revealing a clear phase jump of about  $\pi$  after about 35 s of observation time. This is attributed to a modified energy transfer pathway within this single complex. Error bars:  $\pm 1$  s.d.

Remarkable variations in the ultrafast response of single complexes were tracked with our rapid phase-cycling approach. As an example Fig. 5.9a presents the raw data from an individual aggregate. Each block with about 8 s measurement time represents a phase-scan at a constant inter-pulse delay of 100 fs. Whereas the (temporal) average over the entire 120 s measurement (Fig. 5.9b, green symbols) is basically identical to the reference signal (open black symbols) and does not reveal phase-sensitive features, analysing time intervals of the data gives a completely different picture as demonstrated in Fig. 5.9c: the red circles depict the emission as a function of phase for the first ca. 35 s of observation time, and the blue circles show the fluorescence at later parts of the

measurement. The observed jump of the oscillation phase by about  $\pi$  demonstrates a change in the ultrafast response of this single complex after some ten seconds. This phase jump must result from a change of the accumulated phase of the relaxing excitation, because the experimental conditions were the same throughout the entire measurement.

A comparison to eq. (5.9) is also in this case instructive. For the data shown in Fig. 5.8, recorded at fixed inter-pulse delay, all parameters are constant except the relative phase  $\Delta\phi$  between the pulses. Then the last cosine-term gives an oscillatory total excited state population as a function of  $\Delta\phi$ . The phase jump observed in Fig. 5.9 can then only arise from a change in the energy mismatch  $\delta$  or in the accumulated phase  $\zeta$  during relaxation. As variation of  $\delta$  also influences the amplitude of the oscillations, which is not observed in our data, we ascribe the phase jump to a change in the accumulated phase during transfer.

This change in relaxation phase implies a modification of the energy transfer pathway probably related to subtle structural rearrangements in the complex<sup>218,219</sup> that alter mutual distances and angles between the Bchl *a* pigments as well as their site energies due to different local interactions. Remarkably, the amplitude of the phase dependent modulation remains basically constant although the phase relation is inverted, which indicates persistent coherence even for changing transfer pathways.

It is important to note that both ensemble and temporal averaging washes out all features observed in the sub-sets of the data as illustrated in the temporal average in Fig. 5.9b (open green symbols). Hence, experiments integrating over too long time scales or on ensembles of many complexes would lead to the unjustified conclusion that phase memory was lost completely already within  $\Delta t=100$  fs. It is clear from these data that only single-molecule detection allows all subtle details of a complex system in the presence of thermal disorder to be revealed.

Long-lived quantum coherences in photosynthetic complexes have been attributed to correlated nuclear motions in the local dielectric environments of the pigments<sup>83,84,123,124,209,213</sup>, such that the energy gap as well as the electronic coupling between B800 and B850 remains constant. For the biological function of LH2 it is the interplay between this persistent coherence and energy dissipation by interactions with the surrounding bath<sup>214-217</sup> that rapidly directs the excitation energy towards the lowest-energy B850 target levels, from where further transfer to adjacent LH2 or LH1 occurs. Dissipative interactions, on the one hand, stabilise the initially created electronic excitations in lower-energy states on sub-ps time scales to create the ultrafast energy funnel to bottom B850 states and to prevent relaxation along loss channels. On the other hand, quantum coherences survive long enough to allow averaging over local inhomogeneities of the rough excited state energy landscape and thus to avoid trapping in local minima. The highest efficiencies for this environmentally assisted quantum transfer in photosynthetic light-harvesting complexes have been found for comparable time scales of population transfer and dissipative relaxation<sup>214-217</sup>. This requirement is fulfilled for the B800-B850 transfer as we have shown in Figs. 5.8 and 5.9 by efficient weak-field phase-control of the 1-photon transitions into the B800 and B850 excited states<sup>163,225</sup>.

An intriguing feature of our observations is that the quantum beats are rather well-defined compared to ensemble data<sup>83,84,209</sup> and can be described by only a single oscillatory component. Hence, it seems that in each specific LH2 complex only one energy transfer pathway at a time is present. As a rather large number of pigments and thus possible pathways exist per ring, this is likely to be the optimal pathway for the particular geometrical and electronic structure, i.e. for the specific electronic couplings. Moreover, the phase jump observed for the assembly in Fig. 5.9 demonstrates that the long-lived coherences also provide the flexibility to adapt to modifications of the (local) electronic structure, and to find efficient new energy transfer pathways within a complex. In other words, long-lived coherences contribute to the necessary robustness against external perturbations and disorder since thermal disorder is ubiquitous in biological systems at physiological temperatures. In this respect the biological function of these complexes – light absorption and energy funnelling towards the reaction centre – is optimised for each individual aggregate and long-lived quantum coherences play an important role here.

### 5.5 Conclusions

We demonstrated ultrafast quantum coherent energy transfer within single light-harvesting complexes and find that quantum coherences between electronically coupled energy eigenstates persist at least 400 fs, significantly longer than previously reported<sup>84,124,209,213</sup>. Moreover, distinct energy transfer pathways can be identified in each complex. Strikingly, also changing transfer pathways in individual complexes on time scales of seconds are revealed. This is attributed to structural rearrangements of the pigment molecules and the surrounding protein scaffold caused by ubiquitous thermal disorder at room temperature. Our data show that long-lived quantum coherence renders energy transfer in photosynthetic systems robust in the presence of disorder, which is a prerequisite for efficient light harvesting.

Where the previous chapters dealt with the proof of principle experiments and the physics of coherence in open quantum systems, this chapter treated the first application of single molecule coherent control to a biological system. The method resolved energy transfer dynamics in photosynthetic light harvesting with unprecedented selectivity. However, the absolute resolution of excitation was still diffraction limited; in order to select one LH2-complex, the complexes have to be sufficiently spaced in a polymer matrix. It would be a significant improvement if the complexes could be investigated in their native membranes, interacting with their neighboring complexes<sup>186,187</sup>. Ideally, we would still want to be able to selectively excite one complex in these circumstances, and resolves its interaction with neighboring complexes. For this, molecular resolution would be necessary, combined with the ability to shape ultrafast pulses at those length scales.

While this is a goal that has not been attained yet, in the next and final chapter of this thesis (chapter 6) we present the experimental implementation of a framework for ultrafast photonics at the nanoscale that does have the potential of reaching this highly intriguing regime.

This chapter is under review for Nature as  
Hildner, Brinks, Cogdell & van Hulst, *Quantum Coherence Persists in Time-varying Energy Transfer Pathways in Single Light Harvesting Complexes*.

**In this chapter we argue that, in order to bring coherent control to the next level, it is necessary to not only resolve the signal from individual quantum units, but to be able to do so while these units are in close proximity and interacting with other active components in their environment. We develop a framework based on optical antennas that allows for deterministic engineering of the amplitude and phase in subwavelength hotspots, and the development of ultrafast plasmonic components. We experimentally demonstrate phaseshaping by a coupled nanoantenna and a sub-100 fs plasmonic switch.**

## **6. Plasmonic nanoantennas as design elements for coherent ultrafast nanophotonics**

## 6.1 Introduction

Physics, biology, chemistry and engineering are pushed to ever smaller length scales and ever shorter time scales, lured by the prospect of observing and utilizing quantum-mechanical phenomena in large, complex, or disordered systems<sup>85,123</sup>. In the past chapters we have made a contribution to this from a new angle: we developed methods to apply ultrafast spectroscopy to single molecules, i.e. individual quantum units, and utilized this to investigate the effects of long-lived coherence in photosynthetic light harvesting. However, the ultimate goal of this research is to go one step further: to deterministically address individual quantum units in their natural environments. This should be seen in the broadest sense possible: systems of interest include light harvesting complexes in their natural membranes, interacting with their neighboring complexes; nanoscale electrical components leveraging quantum effects (tunneling) at room temperature; spin networks constructed with NV-centers in diamond; chemical reactions on the surface of catalysts; protein evolution under varying light conditions, and the list goes on: really any physical process taking place at ambient conditions and defined or influenced by the properties and dynamics of electrons can be influenced by electromagnetic fields and can benefit from this different perspective.

These processes have several common features: i) a quantummechanical description is necessary to understand the physical phenomena, ii) the process is defined not by isolated quantum units or bulk reactions but by interaction between quantum units and its environment (ranging from highly structured to highly random but dense), iii) the process takes place at room temperature. Feature i) indicates that phase information needs to be encoded into the measurements. ii) shows that a real spatial resolution (as opposed to a fitting resolution) far below the diffraction limit is necessary, in order to resolve substructures in a complex, nanoscopic molecular environment. iii) puts an upper limit on the time resolution: at room temperature in dense matrices, dephasing between superposition states is caused by scattering events governed in a very crude first approximation by a factor that scales with  $(\sqrt{kT})^{-1}$ <sup>137,240,241</sup>, giving dephasing times  $T_2^*$  typically in the  $\sim 10^2$  fs range, while our results for the first time provided a direct measurement for single complex organic molecules in solids of  $T_2^* \sim 30\text{-}60$  fs<sup>85,86,115,242</sup>. The time resolution of measurements on these systems therefore needs to be at least in the low 10 fs.

To unlock this regime many efforts have been made to combine plasmonics, which promises optical investigations at deep subwavelength resolutions, with ultrafast techniques<sup>66,98,113,243-249</sup>. Examples include polarization control of localization<sup>98,244</sup>, measurements of plasmon dephasing<sup>113,245,246</sup>, adiabatic compression of pulses at plasmonic tips<sup>248</sup> and ultrafast excitation of quantum dots in the near field<sup>247</sup>. However, so far a framework for controlling the ultrafast properties of localized fields utilizing plasmonic structures at will has been lacking, as have simple design rules and flexible, scalable and reproducible

designs. These are nevertheless prerequisites for ultrafast plasmonics to find widespread use in nanoscale applications.

An ideal platform to fulfill these objectives is that of plasmonic nanoantennas: metallic particles confining far field excitation to near-field hotspots with properties determined by geometry<sup>50,60,250</sup>, material<sup>61</sup> and excitation method<sup>251-253</sup>. A design that has been tested and analyzed particularly rigorously is that of single and coupled bar antennas<sup>60,61,64,254-258</sup>. These are metal bars of nanometric dimensions, where the width and the height of the bars are typically as small as possible to validate a 1-dimensional approximation. The bars generally exhibit resonant behaviour, where the resonance wavelength can be tuned by the dimensions of the bar<sup>61</sup>. In a first approximation, momentum matching between the plasmon wavevector, the resonance wavevector and the wavevector of the excitation light is required, which determines the wavelengths and polarizations that can excite resonances on particles of a given material with a particular geometry<sup>254,259</sup>. Bringing bars close together creates coupled oscillators, with the coupling strength and thus the resonance splitting determined by the gap size between the bars<sup>64,256</sup>.

The current insights about bar antennas can be distilled down to two important facts: plasmonic antennas confine far-field to near-field, preserving coherence<sup>66,244</sup>; and their resonances exhibit wide bandwidths, which renders them inherently suited for ultrafast processes and coherent control<sup>257,260,261</sup>. In the work presented in this chapter we utilize these properties to design coupled plasmonic antennas for two of the most heralded applications of ultrafast plasmonics: a subwavelength resolution phase shaper and an ultrafast spatial hotspot switch, the aim of which is to facilitate direct phase sensitive, ultrafast measurements in sub-diffraction limited hotspots without the need for a phaseshaping setup.

## 6.2 Experimental method

The output of a broadband Ti:Sapphire laser (Menlo-Systems Octavius 85 M) was expanded and collimated with a set of spherical mirrors and fed into a double pass 4f-pulse shaper based on an in-lab modified MIIPS-box. A 120 nm spectral band centered around 776 nm of the laser output was dispersed with a grating and focused on a 640 pixel double layer spatial light modulator (SLM). The light was reflected back through the SLM, recollimated and recombined, caught on an end-mirror and reflected back through the entire shaper. The shaper output was separated from the input with a polarizing beam splitter and directed through a Glan-Taylor polarizer. The beam was subsequently spatially filtered using a telescope with a 100  $\mu\text{m}$  pinhole.

The experiments were performed on a modified confocal microscope (Zeiss Axiovert). The shaped pulses were led into the back aperture of the microscope and reflected into the sample with a short-pass dichroic mirror (Semrock SDi-01-670). The pulses were focused into the sample plane with a 1.3 NA objective (Zeiss Fluor). The two-photon photoluminescence (TPPL) of the antennas was collected through the same objective, separated from the excitation light by the

dichroic mirror and two short pass filters (Semrock FF01-720SP-25 and FF01-660SP-25) and focused on an APD (Perkin Elmer SPCM-AQRH-16).

Pulse calibration was done via the MIIPS method described in chapter 1 with a micrometer sized BBO-crystal plate in the sample plane. The second harmonic (SH)-signal of the crystal plate was collected in transmission by an optical fiber and focused onto an imaging spectrograph with a sensitive charge-coupled device (CCD) camera (Andor SR-163 with camera Andor DV437-BV). The calibration resulted in a compression mask: a phase added in the shaper to ensure a Fourier limited starting pulse in the sample plane; the pulse shapes utilized in the experiment were added on top of this. For calibration and measurement integration times of at least 20 seconds were used to ensure phase stability of the SH and TPPL signals.

The experiments were performed on gold nanoantennas of variable length, 50 nm width and 20 nm thickness. The sample was fabricated on 10 nm ITO on glass by e-beam lithography, thermal gold evaporation and lift-off, according to a previously described procedure<sup>61</sup>. On the same sample, matrices with repetitions of single antennas with varying lengths and coupled antennas with different ratios between bar lengths were alternated.

The sample was excited with an 85 MHz train of pulses centered at 776 nm with the spectral amplitude and phase as shown in Fig. 6.1. The time-averaged power in the sample plane after spatial filtering and application of additional neutral density filters was  $3.3 \cdot 10^{-6}$  W, corresponding to a flux of  $\sim 2.8 \text{ kW/cm}^2$ .

The antennas were excited with linear polarization along the antenna axis; in combination with the linear antennas this served to avoid any polarization effects.

At the start of each experiment the sample was scanned through the focus of the microscope objective with a piezo scanner (Mad City Labs Nanoview/M 100-3), yielding TPPL images of the matrices of antennas with each hotspot lighting up. The experiments were performed by positioning one of the hotspots in the focus with the piezo scanner. Subsequently the phase shape of the pulse was changed, and the corresponding TPPL response of the antenna was recorded. Typically, all phase shapes were cycled with a 1 s integration time each. The measurement for every phase shape was alternated with an equally long measurement with a Fourier limited reference pulse. This ensures long total integration times for each signal point, and at same time provides the time resolution and reference signal to monitor signal changes unrelated to the experiment. Depending on the antenna and its resonance, the signal was between 2.5 and 6.5 kcts/s. For the data from Figure 6.3 and 6.4, this cycle was repeated between 20 and 30 times; each cycle consisted of 64 measurements of different phase shapes, alternated with 64 reference measurements. The signal traces are based on total amounts of counts between 50 and 200 kcts per point. For the data in Figure 6.5, the cycle consisted of 36 delay measurements, interleaved with 36 reference measurements. This cycle was repeated 5 times; the signal traces are based on a total amount of counts between 12 and 35 kcts per point.

The signal error bars in all graphs are the magnitude of deviations of the 64 reference measurements to their average. The errorbars for Figure 6.4 also hold

for Figure 6.3 and are 1.5%; note that in Figure 6.3, although the measurements were performed on individual antennas and the stated error holds for that, the graph shows the average signature of three antennas to enhance the signal to noise. The error bars in  $\delta$  in Figure 6.4 reflect the calibration accuracy for the Fourier limited pulse: the residual phase after compression was flat to within  $0.1\pi$  radian. This error practically falls away in the significantly larger phase added to the pulse in Figure 6.5:  $-500 \text{ fs}^2$  chirp gives a quadratic phasefunction with a range of  $5\pi$  radians throughout the pulse spectrum; the error resulting from the uncertainty in compression amounts to a 2% uncertainty in delay, i.e. maximum  $\pm 2 \text{ fs}$  at  $100 \text{ fs}$  delay. The signal error bars in Figure 6.5 are also determined by the deviation of the reference measurements to their average and are in the range of 6% due to the shorter integration time and the division between 2 traces.

### 6.3 Phase measurements through antenna signatures

To engineer the femtosecond field dynamics in coupled antenna hotspots, we control the ultrafast properties of the building blocks: single bar antennas. The Fourier principle states that this can be done by measuring their spectral amplitude and phase profiles. The antenna exhibits a resonance that creates a spectral phase jump which we measure using a phase-sensitive technique grafted onto the Multiphoton Intrapulse Interference Phase Scan Method (MIIPS)<sup>32,170</sup>. Briefly, we excite a gold nanoantenna with pulses of  $15 \text{ fs}$ , (corresponding to a spectral width of  $120 \text{ nm}$  at  $776 \text{ nm}$ , Fig. 6.1a) and add a series of cosinusoidal phase functions to the pulse in a pulseshaper:  $\varphi(\omega) = \alpha \cos[(\omega - \omega_0)\beta + \delta]$  (Fig 6.1b). The phase the antenna adds to the pulse changes the PTP, which is sampled by the scanning cosinusoidal phase (Fig 6.1b) and read out in the Two-Photon Photoluminescence (TPPL) intensity from the antenna as a function of the phase offset  $\delta$  (fig. 6.1d). This antenna signature maps how strongly each wavelength in the laser spectrum contributes to the two photon excitation when influenced by the antenna phase.

As explained in Chapter 1, for a laser pulse with a spectrum centered at  $\omega_0$  and spectral amplitude  $E(\Delta)$  at  $\Delta = \omega - \omega_0$  we can calculate a probability for a two-photon interaction (PTP) at frequency  $\omega_{TP} = 2(\omega_0 + \Delta)$ . The PTP is defined as

$$PTP(\Delta) = \left| \int |E(\Delta + \Omega)| |E(\Delta - \Omega)| e^{i[\varphi(\Delta + \Omega) + \varphi(\Delta - \Omega)]} d\Omega \right|^2 \quad (6.1)$$

where the integration variable  $\Omega$  is the detuning from the central frequency  $\omega_0$ .

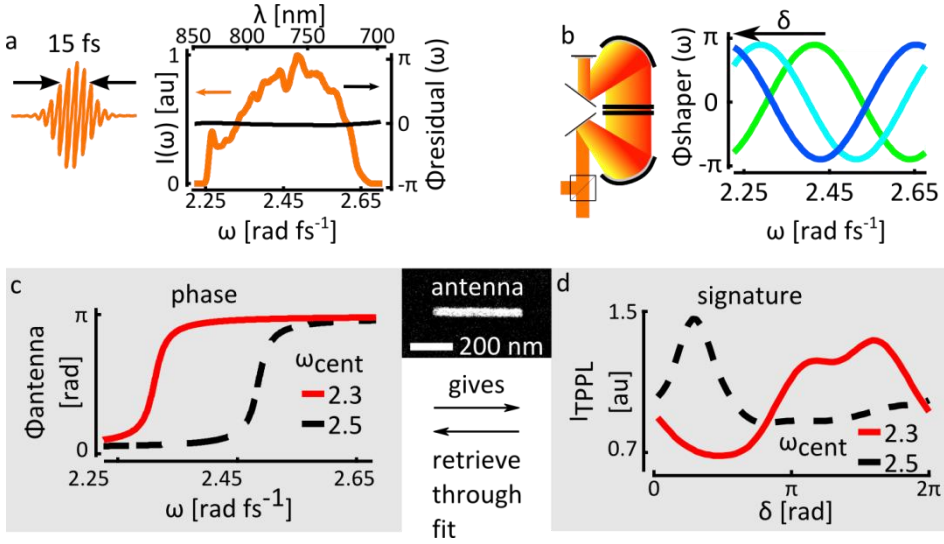


Figure 6.1: **Characterization of spectral amplitude and phase in nano-antenna hotspots.** a) A gold nanoantenna (inset) is excited with a Fourier limited 15 fs pulse with depicted spectrum and residual phase  $\Phi_{\text{residual}}$  flat within  $(0.05 \pm 0.05\pi)$  rad. b) A series of cosinusoidal phases with shifting offset  $\delta$  is added to the pulse in double pass 4f pulse shaper. c) The antenna resonance adds a particular phase the field in hotspots that is absorbed to create TPPL. d) The shifting cosinusoidal phase samples the antenna phase, which gives an antenna signature that can be fitted to retrieve the phase profile (see also Fig. 6.2).

Here,  $E(\omega)$  is the spectral amplitude of the field in a hotspot, and  $\varphi = \varphi_{\text{residual}} + \varphi_{\text{shaper}} + \varphi_{\text{antenna}}$ . The PTP thus depends on three phases: the known residual phase in the fundamental spectrum after pulse compression (Fig. 6.1a), a known phase added in the shaper (Fig. 6.1b), and the phase added to the field by the antenna (Fig. 6.1c).

Following the MIIPS method we add a series of cosinusoidal phase functions  $\varphi_{\text{shaper}}(\omega) = \alpha \cos[(\omega - \omega_0)\beta + \delta]$  to the excitation spectrum (Fig. 6.1b). For a treatment of MIIPS, we point to chapter 1 and the references therein. In a first approximation, with the antenna in place,  $\delta_{\text{max}}$ , the value for  $\delta$  giving the maximum signal at SH frequency  $\omega_{\text{TP}} = 2(\omega_0 + \Delta)$ , measures the relative phase the antenna adds to the pulse at  $\omega = \omega_0 + \Delta$ .

The PTP is directly imprinted onto a Second Harmonic (SH) spectrum acquired for each value of  $\delta$  (Fig. 6.2, inset), and consequently recording the SH spectrum as a function of  $\delta$  would allow for calculation of the completely unknown antenna phase in a hotspot (Fig. 6.2).

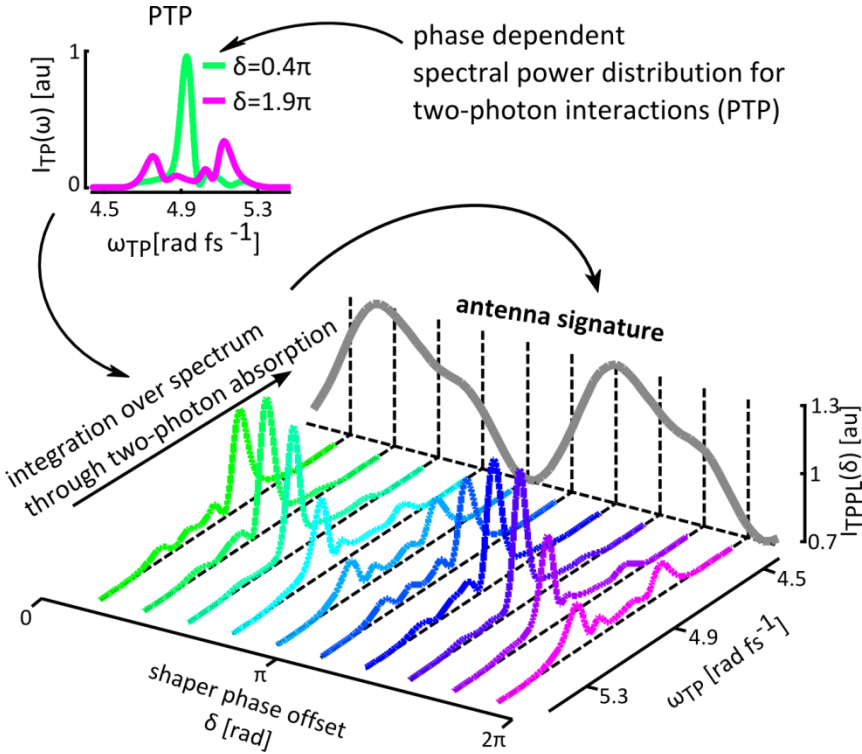


Figure 6.2: **Mapping the antenna phase in a TPPL signature.** In SH, the frequency with maximum spectral intensity as a function of  $\delta$ ,  $\omega_{\max}(\delta)$ , maps the spectral phase. In good approximation the PTP for each  $\delta$  is dominated by this frequency (inset). For a nonzero spectral phase,  $\omega_{\max}(\delta)$  will deviate from the linear relationship between  $\delta$  and  $\omega_{\max}$  as shown in eq. 6.6. This deviation is mapped in the antenna signature for 2 opposite trial phases in the ranges  $0 < \delta < \pi$  resp.  $\pi < \delta < 2\pi$ . This provides a quasi-2D solution to the amplitude-phase determination problem, allowing to fit the signatures to determine the spectral amplitudes and phase.

However, gold nanoantennas generate only small SH signals but exhibit two photon absorption followed by luminescence (Two-Photon Photo-Luminescence, TPPL)<sup>60,251</sup>. This signal,  $I_{TPPL}$ , depends on the total probability of generating a two-photon transition in gold and is proportional to the integrated PTP. Recording  $I_{TPPL}$  as a function of  $\delta$  in a hotspot thus gives an antenna signature (Fig. 6.2). While it is the entire signature that provides the information, and a fit to the antenna signature is needed to gain full access to this information, under some simplifying assumptions a rather intuitive picture emerges. For example,

$$\varphi''_{shaper}(\omega, \delta_{\max}) + \varphi''_{antenna}(\omega) = 0 \quad (6.2)$$

expands to

$$-\alpha\beta^2 \cos[(\omega - \omega_0)\beta + \delta_{max}] = 0 \quad (6.3)$$

if there is no antenna phase added to the pulse; this equation has a solution

$$\delta_{max} = -\beta(\omega - \omega_0) \pm \frac{\pi}{2} \quad (6.4)$$

which shows that there is a linear relation between the frequency  $\omega$  and the value for  $\delta$  that gives the maximum SH signal at  $2\omega$  (with a periodicity  $\pi$  in phase space). By satisfying

$$(\omega - \omega_0)_{max} = \frac{(\frac{\pi}{2} - \delta)}{\beta} \quad (6.5)$$

this equation also gives, for a given  $\delta$ , the position of the maximum in the PTP:

$$\omega_{TP,max} = 2(\omega_0 + \Delta)_{max} = 2\omega_{max} = 2\omega_0 + \frac{(\pi - 2\delta)}{\beta} \quad (6.6)$$

i.e. the frequency that has the maximum probability of creating a two photon excitation (Fig. 6.2, inset).

Fig. 6.2 shows that it is a realistic assumption that the PTP for each given  $\delta$  is dominated by this frequency. This means that the two photon excitation in the gold and with that the TPPL signal for each  $\delta$  is so as well. It follows that the signature between 0 and  $\pi$ , when no antenna phase is present, maps the shape of the fundamental spectrum, as can be seen in Fig. 6.2 (compare the signature in the  $0 < \delta < \pi$  range in Fig 6.2 with the shape of the spectrum in Fig. 6.1, keeping in mind that  $\omega_{max}$  is decreasing for increasing delta and the spectrum is thus mirrored in the signature).

A change in spectral phase caused by the antenna will change the relative contribution of the affected wavelengths to the TPPL, which will be reflected in the TPPL response as a function of  $\delta$  (Fig 6.1c-d). When the antenna influences the pulse amplitude and phase, and thus the TPPL signal, the signature cannot be read in such a straightforward manner anymore, primarily because the linear relation in eq. 6.6 does in general not hold true anymore after interaction with the antenna, either because some frequencies in the excitation band have their strength reduced due to the amplitude shaping effect of the antenna, or because in  $\varphi''_{shaper}(\omega, \delta_{max}) + \varphi''_{antenna}(\omega) = 0$ ,  $\varphi''_{antenna}(\omega)$  is not negligibly small anymore for all  $\omega$ . Therefore a complete fit is needed to resolve the antenna phase. However, the difference between the signature in the range  $0 < \delta < \pi$  and in the range  $\pi < \delta < 2\pi$  allows us to differentiate between the effects the antenna has on the spectral amplitude and on the spectral phase of the field. This

can readily be seen when it is taken into account that  $\varphi_{shaper}(\omega, 0 < \delta < \pi) = -\varphi_{shaper}(\omega, \pi < \delta < 2\pi)$ . This means we are obtaining a quasi-2D solution to the 2D problem of measuring an unknown amplitude and phase.

The relation between an antenna signature and a full, spectrally resolved MIIPS trace is akin to that between an autocorrelation or cross correlation measurement and a FROG signal. To be more precise, a MIIPS and a FROG trace contain the same information; the signature contains as much information as two cross correlation measurements on an unknown pulse with two correlation pulses with different central wavelength. In analogy to the approach to get information about the spectral phase in a pulse from an autocorrelation, we fit the measured antenna signature and obtain the phase profile in the antenna hotspot (Fig. 6.1d), by applying prior knowledge of the fundamental spectrum and limiting the search space for the fit to expected types of phase profiles. In this case, we employ a least squares fit in a basis of Lorentzian resonances where the number of resonances, their central wavelengths, their widths and their relative weights are free parameters. Invoking Occam's razor, we keep the number of resonances as low as possible, i.e. we start with one resonance, let the central wavelength, width, and relative strength run and choose the best fit. We fix that resonance and add a second resonance, of which we let the central wavelength, width and relative strength run, and obtain the best fit. We keep adding resonances until  $\chi^2$  of the fit approaches 1.

## 6.4 The building blocks: single bar antennas

Figure 6.3a presents the antenna signatures of single bar antennas with increasing lengths from 480 to 640 nm, recorded with  $\alpha=0.9\pi$  and  $\beta=14$  fs. An intuitive understanding of these data can be gained by considering that the highest TPPL signal occurs when the shifting cosinusoidal phase  $\varphi_{shaper}$  compensates for the spectral phase of the antenna resonance best. The particular shape of the band of maximum intensity that starts at  $\delta = 0$  rad at 480 nm rods and curves towards  $\delta = \pi$  for longer rods (Fig. 6.3a) can thus be interpreted as the phase jump that the excitation light at carrier wavelength 776 nm experiences when it drives the antenna above or below the resonance frequency, which decreases towards longer structures. Recording the signature between  $0 < \delta < \pi$  and  $\pi < \delta < 2\pi$  allows us to differentiate between the effect the antenna has on the spectral amplitude and on the spectral phase of the field.

To retrieve the spectral resonance profiles of the antennas, the measured signatures are compared to fits based on Lorentzian resonances that are given by

$$L(\omega) \propto \frac{1}{\omega_{cent} - \omega - i\gamma} + \frac{1}{\omega_{cent} + \omega + i\gamma} \quad (6.7)$$

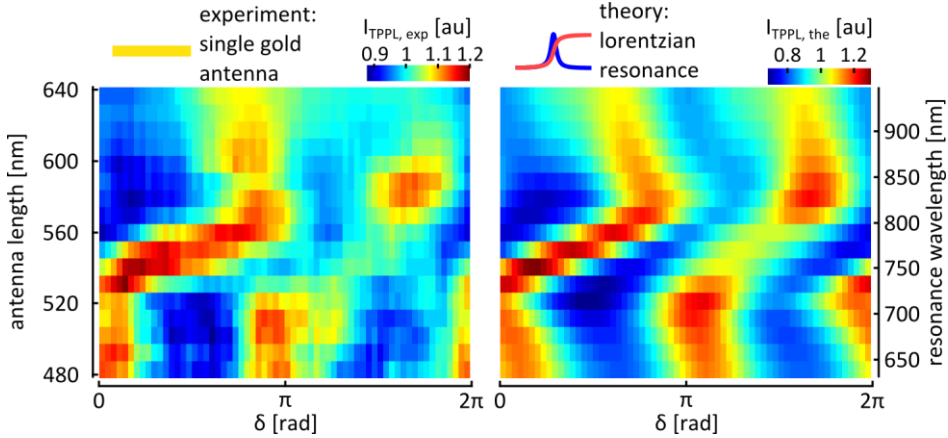


Figure 6.3: **Coherent ultrafast dynamics of single nanoantenna hotspots.** a) Antenna signatures measured for gold nano-antennas of different lengths. b) Corresponding signatures calculated for Lorentzian resonances at different wavelengths with a width of  $0.13 \pm 0.02$  rad fs<sup>-1</sup> (or  $41 \pm 6$  nm at 776 nm).

Here  $\omega_{\text{cent}}$  is the central frequency of the resonance,  $2\gamma$  is the full width at half maximum (FWHM) of the imaginary (i.e. absorptive) part of the resonance and the antenna phase is defined as  $\varphi_{\text{antenna}}(\omega) = \arg[L(\omega)]$ . These fitted signatures are depicted in Fig 6.3b. The best fits are obtained if the width of the Lorentzian is kept at  $2\gamma = 0.13 \pm 0.02$  rad fs<sup>-1</sup> (or  $\Delta\lambda = 41 \pm 6$  nm at 776 nm central wavelength) while the resonance wavelength is varied from 640 nm for antennas of 480 nm length to 940 nm for antennas of 640 nm length (corresponding respectively to  $\omega_{\text{cent}} = 2.95$  rad fs<sup>-1</sup> and 2 rad fs<sup>-1</sup>).

TPPL has been used as a preferred characterization tool for hotspots from the earliest works on plasmonic antennas (see e.g. <sup>60,251,262</sup>). The good qualitative agreement, shown in Figure 6.3, in the trend between the signatures measured on the single antenna bars and calculated for the reconstructed resonances demonstrates that viable phase information can be extracted from the TPPL measurements of the antenna signatures. However, the contrast in the measured signatures is markedly less than that in the calculated signatures. This can have several reasons. First, liquid crystal based phase shapers work under the approximation that a particular pixel in the liquid crystal (LC) corresponds to a particular wavelength in the spectrum. In reality however, each pixel will receive a band of wavelengths determined by the pixel size and the NA of the optics focusing the light on the LC. Hence, each wavelength will be focused on a band of pixels determined by the same parameters. As a consequence of this, a phase function added in the shaper  $\phi(\omega)$  transforms to the actual phasefunction

$$\varphi(\omega) \text{ given by } \varphi(\omega) = \int \phi(\Omega) g(\omega - \Omega) d\Omega, \text{ where ideally } g(\omega) = \delta(\omega),$$

the Dirac delta function, but in reality is a function with a finite width. Effectively this means that amplitude  $\alpha$  of the applied function will become slightly lower than in theory, limiting the contrast in the recorded signature.

Another source of limited contrast is the phase noise in the excitation pulse. When the residual phase in the spectrum fluctuates, it is possible to obtain a PTP with the correct shape by integrating long enough, but the total power in the integrated PTP will be lower and the effective amplitude  $\alpha$  of the added phase function will go down with the width of the noise band; this will limit the contrast in the signature.

Finally, an interesting possibility was posited by Biagoni *et al.*<sup>263,264</sup> that an intermediate state in the gold is involved in the generation of TPPL. The exact dependency of a TPPL signal on this state is elusive; it shows varying behaviour depending on pulse widths, peak powers, central wavelengths, etc. The variation in the signatures clearly shows a phase dependence of the TPPL signal, but a short lived intermediate level is a likely candidate in accounting for the loss in contrast in the measured signal compared to theory. However, a full treatment of its causes and influences goes beyond the scope of this work, especially since the behaviour measured by Biagoni *et al.* is for significantly higher peak powers and pulse lengths.

## 6.5 The subwavelength resolution phase shaper

Knowledge of the amplitude-phase profiles of the single antennas (Fig. 6.3) allows us to create hotspots with tailored ultrafast responses by coupling antennas. The field in each hotspot in such a system is influenced by the resonances of the building blocks, modified by the dispersion and absorption of the coupled system. The subwavelength resolution phase shaper can then be engineered by combining single antenna bars as building blocks into a linearly coupled asymmetric antenna, separated by a nanometer sized gap.

The concept of engineering ultrafast nanophotonic systems with plasmonic antennas as building blocks is demonstrated in Figure 6.4 where we present the retrieved amplitude-phase profiles of the hotspots on a single bar antenna of 530 nm (Fig. 6.4a) and 620 nm length (Fig. 6.4b), as well as the 530 nm (Fig. 6.4c), resp. the 620 nm side (Fig. 6.4d) of a coupled antenna with a gap of  $\sim 30$  nm. The comparison of the signatures of antennas of the same length, either coupled to another antenna or not, reveals distinct differences in the amplitude- and phase-profiles in their hotspots (compare Figs. 6.4a and c; Figs. 6.4b and d).

Insight into the mechanism that determines the ultrafast properties in each hotspot is gained by fits to the measured signatures. Figure 6.4 shows the data with the best fit (left) and the corresponding reconstructed resonance profile (right). The best fits for the signatures were obtained by significantly broadening the single antenna resonances from  $0.13 \pm 0.02$  to  $0.26 \pm 0.06$  rad fs<sup>-1</sup> for coupled antennas, indicating that the total dispersion of the combined antenna determines the width of the resonances in each profile.

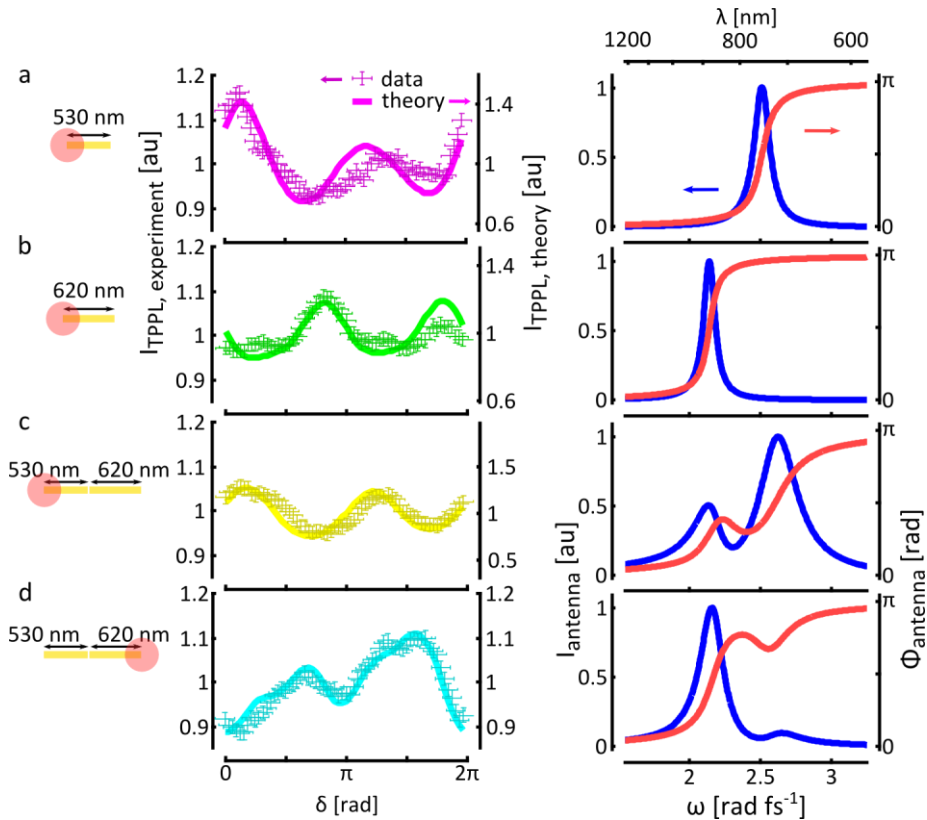


Figure 6.4: **A subwavelength resolution plasmonic phaseshaper.** a) Antenna signature measured in a hotpot on a 530 nm single antenna (left) and the resonance profile retrieved from the fit (right). b-d) Corresponding signatures (left) and resonance profiles (right) for a 620 nm single antenna and different positions on a coupled 530-620 nm asymmetric antenna, demonstrating the engineering of spectral phase in antenna hotspots by mixing resonances with different strengths.

The losses in the metal, giving rise to the broadening, are a vital property of the design, because they largely determine the range of the spatial mode associated with the resonance and therefore its strength in a particular hotspot. In this way, a plasmonic nanoantenna can be employed as a subwavelength resolution phase shaper, as shown in Fig. 6.4 (c,d, right): the phase the antenna imprints on the hotspot-sized field can directly be tuned by adapting the strength and separability of the resonances of the constituent antennas in the hotspot.

## 6.6 The ultrafast plasmonic switch

The reconstructed phase-profiles in the hotspots give insight into the phase-sensitive properties of hotspots on coupled nanoantennas, and more specifically the role of the spatial range of resonant modes. This now allows us to redefine coherent control in coupled plasmonic systems in an intuitive way as addressing spectrally separable resonances in a particular hotspot with the appropriate strength and timing to achieve the desired temporal field structure. Hotspot switching can then be realized by simply addressing localized resonances at different times in an excitation pulse through application of a spectral phase. To demonstrate this concept, we engineer a simple asymmetric coupled antenna to function as a sub-100 fs spatial hotspot switch.

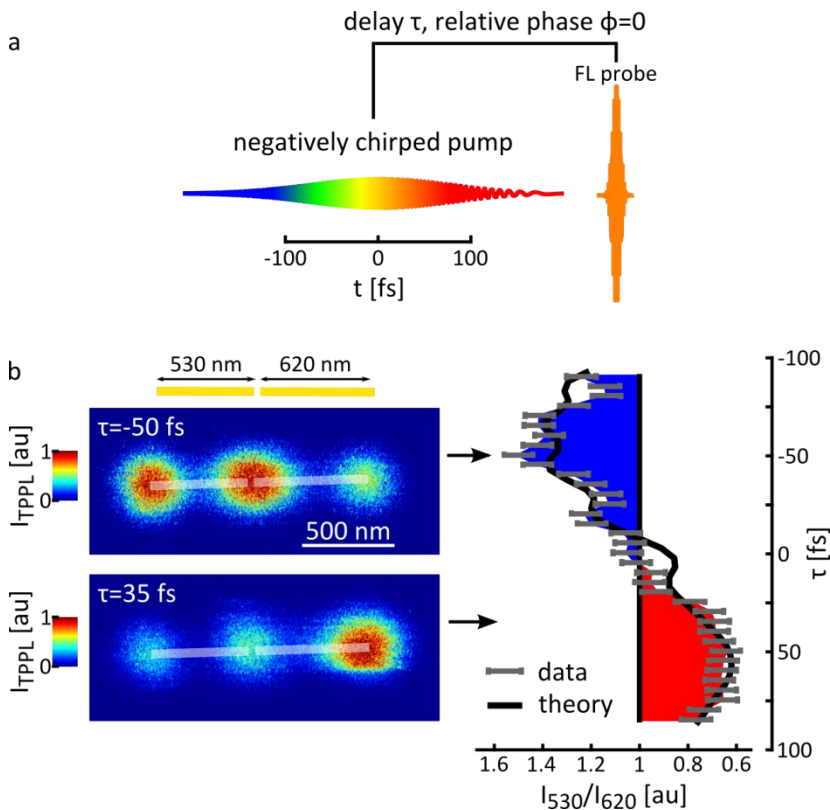


Figure 6.5: **A sub-100 fs plasmonic switch.** a) The dynamics of the hotspots are resolved in a pump-probe experiment. b) Between a pump-probe delay of -50 fs and 35 fs the luminescence intensity switches from the 530 nm antenna bar to the 620 nm antenna bar with a contrast ratio  $\sim 2.8$  (right). Imaging the antenna with these delays fixed, demonstrates the sub-100 fs plasmonic switching (left).

Antennas with lengths of 530 nm and 620 nm are chosen as suitable building blocks because they feature resonances on the high-, resp. low frequency side of our excitation spectrum. The coupled antenna is excited with a negatively chirped pulse (-500 fs<sup>2</sup> chirp). Using the asymmetry in the resonances of the different hotspots (as shown in Fig. 6.4c,d, right), this creates a concentration of intensity on the short antenna bar in the first half of the pulse, switching to the long antenna bar in the second half of the pulse. The dynamics of the field can be resolved by employing a time-delayed, Fourier-limited probe pulse (Fig. 6.5a).

For the pump probe experiment the intensity of the TPPL signal in the hotspots is recorded as a function of the delay between the chirped pump pulse and the Fourier limited probe pulse, with both pulses having the same spectrum. This double pulse was created in a pulse shaper. In order to avoid fast interference fringes, the probe pulse was phaselocked to the central frequency of the band it was overlapping in the chirped pump pulse at each delay (Fig. 6.5a). The total probability for a two-photon-excitation in each hotspot depends on the initial spectrum of the pulse (Fig. 6.1), the chirp added in the pump pulse (-500 fs<sup>2</sup>), the amplitude and phase profiles in the hotspots (Fig. 6.4), and the delay and phase between the pump and the probe pulse (Fig. 6.5a).

The ratio between the TPPL intensity from the hotspots on the 530 resp. 620 nm side of the coupled antenna is depicted in Fig. 6.5b (right, gray points) as a function of pump-probe delay. The intensity switches from the 530 nm side to the 620 nm side between delays of -50 fs and +35 fs with appreciable contrast (~2.8). The comparison between experiments and theory based on the resonance structure of the hotspots and the chirp in the excitation pulse (Fig. 6.5b, right, solid black line) shows a good agreement between the actual hotspot switching of the antenna and the theoretical behaviour for which the antenna was designed ( $R^2=0.92$ ). The theoretical curve was calculated by integrating the PTP for each pump-probe pair in both hotspots, and dividing the two values.

The ultrafast switching can directly be visualized by imaging the antennas with fixed pump-probe delay at -50 fs (Fig. 6.5b, top left), resp. 35 fs (bottom left). This demonstrates the utility of a coupled antenna for hotspot switching within 85 fs, applying only quadratic chirp in the excitation pulse.

Our scheme shows the potential for subwavelength coherent control and spectrally selective ultrafast microscopy without the need for a phase shaper: one can design an antenna that will have the required spectral phase for the desired multiphoton excitation process in the hotspot of interest. Spatially resolved pump-probe experiments are another easily performed application: the switching time in the ultrafast plasmonic switch can be scanned by changing the chirp in the excitation pulse, simply through adding dielectric material in the beam path. Bandwidths, switching times, localization contrast and phase gradients are all governed by the prominence of the resonances in each hotspot; material properties, gap sizes and relative orientations provide a wide range of parameters to tune the resonance strength and separability in the hotspots.

## 6.7 Conclusions

Investigations at ultrafast timescales are being rapidly embraced in fields as diverse as semiconductor physics, cell biology and quantum optics. What unites these areas is the transition from research on phenomena in isolated or uniform systems (molecular jets, ultracold atoms, solutions) to nanoscale components interconnected in larger systems (optoelectronic switches, supramolecular complexes, cells, NV-center networks). For this paradigm shift, femtosecond time resolution needs to be combined with high spatial selectivity and complete control of the time-evolution of fields with nanometer precision, as we have demonstrated here.

One application that will be particularly interesting in the context of this thesis is the investigation of LH2-complexes as in the previous chapter, but now not in a polymer membrane but in their native membranes. A resolution that would allow to differentiate between clusters of LH2 surrounded by other LH2 resp. adjacent to e.g. LH1 would become feasible: for the investigation of single LH2 in this context the resolution (i.e. gap size) of 10 nm would be necessary<sup>186</sup>. This type of resolutions has been achieved with e.g. bowtie antennas<sup>265</sup>, which would be a viable symmetry to continue this line of investigation on.

This chapter is under review for Science as  
Brinks, Castro-Lopez, Hildner & van Hulst, *Plasmonic Nanoantennas as Design Elements for Coherent Ultrafast Nanophotonics*.



## **Conclusion**

The results presented in this thesis show the possibility of creating, manipulating and probing coherence in room temperature single molecules. This allows investigation of e.g. the coherent nature of energy transfer in single light harvesting complexes at room temperature; a technique based on plasmonic antennas, with the potential to apply the ultrafast single molecule scheme in *in vivo* molecular complexes, is outlined.

Special care is needed to avoid artefacts of spatio-temporal coupling when focusing ultrabroadband pulses to the diffraction limit. Utilizing a calibrated double pass scheme and stringent spatial filtering will allow for uniform spectral characteristics throughout the focal region; calibration of the pulse in the focal plane using Multiphoton Intrapulse Interference Phase Scan (MIIPS) ensures a Fourier limited pulse to start experiments with.

Single molecule measurements at room temperature are typically done in fluorescence. To measure coherence in a fluorescent signal, a phaselocked pump probe measurement is necessary where the first pulse creates a coherence in the molecule that is mapped to a population with the second pulse. Using this method the decay of coherence in single organic molecules was measured, yielding an average decoherence time of 50 fs with a wide spread in values.

Manipulating the superposition state at timescales below the decoherence time allows bringing the molecule into a rabi cycle and to drive it as an ultrafast single molecule “qubit” at room temperature. At even faster timescales, the coherence is modulated by vibrational interactions, leading to nonstationary superpositions (wavepackets) that can be probed to quantify the ultrafast vibrational dynamics of single molecules, visualize the influence of the environment on molecular dynamics and manipulate the superposition state with high fidelity; this is the first step towards quantum tomography of molecular quantum systems at room temperature.

Light Harvesting Antennas (LH2) of purple bacteria were investigated using the insights of the proof-of-principle experiments. A two-color, phaselocked pump probe experiment was designed to investigate the energy transfer between the B800 and B850 molecules in LH2. Transfer takes place through delocalization of an exciton over B800 and B850; oscillations of the induced wavepacket between B800 and B850 were measured, showing two distinct energy transfer pathways and a wide distribution in coupling strengths: it can be deduced that dark B850 mediate the coupling to B800. Time resolved measurements allow the visualization of changes in the energy transfer pathway, while coherence is maintained, indicating that the coherent transfer pathway is dominant even for changing conformations of the molecule.

---

Another way of interpreting this experiment is that weak-field phase control of the B800-B850 Energy transfer pathway is performed; this is possible when the Energy transfer times, coherence decay times and energy dissipation times are of the same order of magnitude, as is the case in LH2.

Finally, in order to investigate the dynamics of these molecular systems in their natural environment, a spatial resolution significantly below the diffraction limit is necessary. Coupled plasmonic antennas provide hotspots with the ultrafast characteristics to make this possible. It is shown that the spectral phase of light in a plasmonic hotspot is easily tunable by the antenna dimensions, and can be measured directly in the hotspot.

Simplification of the ultrafast scheme should lead to a wider applicability: to this end, plasmonic antennas can be configured in schemes that achieve nanoscale ultrafast experiments by themselves. As examples, a plasmonic phaseshaper and an ultrafast plasmonic switch for spatially resolved pump probe experiments is presented.

The results presented in this thesis form the first induction and observation of ultrafast coherent dynamics in individual molecular systems at room temperature. This is a necessary step to be able to do true quantum tomography in complex systems and resolve the influence of the environment on molecular dynamics. Moreover, the groundwork has been laid for the investigation of quantum dynamics in functioning biosystems and a technique has been presented that has the potential to achieve this in natural environments, e.g. cell membranes. This opens the fascinating possibility of exploring the quantum physics that determines evolutionary optimization and functionality in biomolecules.



## **Acknowledgments**

*If I have seen further, it is by standing on ye sholders of Giants*

- *Sir Isaac Newton*

Science is not an endeavor one pursues alone. I am forever indebted to the following people, for plentiful knowledge, for scientific rigor, for support during the hard times and company during the good ones, for keeping me sane during the uninterrupted days-long measurement sessions, for broadening my horizon, and for shaping my experience to be the best one possible.

I am no Newton, but I have had the pleasure to be in the company of giants, both scientifically and personally, and for that I am deeply grateful.

I will never be able to sufficiently express my appreciation, respect and gratitude towards my advisor Niek van Hulst. Deeply knowledgeable and with the confidence to allow others freedom, he truly showed me what science is about, educated me on every aspect of scientific life and defined the value of this PhD. He kept me going after the first years of my work ended in a major disappointment, provided ideas, knowledge and insights on projects, allowed the freedom to pursue own ideas and was generous enough to invest in them. I am honored to have been able to work with him and hope that this PhD was the start of a long collaboration.

Every project I undertook was a joint effort. I worked closely together with Richard Hildner and Fernando Stefani for most of my PhD; they planted the experimental tricks, the day-to-day-knowledge, the habit of looking at problems from different sides, the laboratory savvy, the practical approach and the need to keep asking; in short: they made me a scientist not just in theory, but in practice, and in doing so exposed the beauty of scientific experimentation, the thrill of a well-designed experiment and the joy of discovery. Better scientists or better people will be hard to find and I am proud to call them friends.

The same holds for Florian Kulzer, whose vast, insane amount of knowledge on physics is only surpassed by his skill in scientific programming; without him, none of the experiments would have been possible, and most of my late evenings in ICFO would have been very boring. It did not matter with what I turned to him, he would not only be willing, but actually be able to help. I hope I will one day be in a position to have his back the way he continuously had mine.

The plasmonic part of this thesis would not have been possible without the great work of Marta Castro-Lopez, whose nanofabrication skills far outweigh mine with an ultrafast laser. Professional, smart and kind she was the ideal collaborator. Marta, wherever I find Estrella Galicia, I'll raise one for you.

I have shared long (and I mean loooooong) days and late nights with my officemates. Gabriel Sanchez Garcia and Aude Lereu (though technically not in my office we did have similar late-night working habits) had the task of keeping me awake during my early years; they made ICFO feel like good place to be at any point of day or night. Later Florian, Jacob Hoogenboom, Alberto Curto and Martin Kuttge were great company, great sources of knowledge and discussion, and great friends, and somehow managed to make it very agreeable that I saw

---

them more than anyone else on a daily basis. I hope to continue seeing them, albeit somewhat less frequently.

I am grateful to everyone I met in the van Hulst group: Niek van Hulst, Alberto Curto, Martin Kuttge, Lars Neumann, Klaas-Jan Tielrooij, Jana Nieder, Anshuman Singh, Marta Castro, Riccardo Sapienza, Pablo Roque, Nicolo Accanto, Gaetan Calbris, Ion Hancu, Richard Hildner, Fernando Stefani, Koen Thuijs, Lukas Novotny, Gabriel Sanchez, Dominique Heinis, Aude Lereu, Tim Taminiau, Florian Kulzer, Richard Hildner, Jacob Hoogenboom, Pavan Kumar, Pierre Bondareff, Benedicte Hingent, Jorick van 't Oever, Haiyan Ma, Salvatore Minissale, Loc le Xuan, and anyone I might be forgetting because I am writing this towards a deadline: thank you. Thank you for being wonderful colleagues, inspiring collaborators, and great friends. You made these past years fly by like a breeze, provided humor and insights when needed (often at the same time and related to an error on my part) and thanks to you, I would do this PhD all over again. Good luck!

ICFO and Barcelona have given me some of the best friends imaginable. Koen, Candan, Sashka, Masa, Lars, Guen: Thanks for keeping me sane. I fully expect to see all of you in every corner of the world with great regularity. A hearty 'balk' for you, bambini! Marcos, Lisa, Lisa, Stephen, Saba, thanks for giving me a home. Maria Rosaria, Fabio, Erika, Carolina, Tijmen: Chic@s, nuestro show era lo major de Barcelona. Un dia lo continuaremos!

There is a great amount of people at ICFO that I should thank for general support, for fun, for friendship, for being there without question and for making these past years absolutely wonderful. Rather than spelling out an enormous list of names with the risk of overseeing a name I should not oversee, I'm going to say you all know who you are: I could not have done it without you and I will always consider you friends. We will stay in touch.

Distance creates perspective, and for impressing that very necessary sense of relativity on me, for providing balance and for friendship that stood the test of time and distance I am thankful to Thijs, Maaïke, Carsten, Daan and Tjeerd.

Maaïke, for more than a decade your friendship brought me rest and peace of mind: thank you for always being there.

Thijs, my fellow Balconato, what can I say? You know me better than I know myself. Should I have needed a paranimf, it could only have been you.

Which brings me to the final part, the cream of the crop. And the funny thing is, once you reach a certain point, the more important and general it gets, the less words you need.

Thanks to my sister and brother, Eva and Koen. For being family.

Thanks to my parents, Ria and Ger. For everything.

Thanks to Si-Hui. You leave me speechless.



---

## Publications

*Publications covered in this thesis:*

1. D. Brinks, F.D. Stefani, F. Kulzer, R. Hildner, T.H. Taminiau, Y. Avlasevich, K. Müllen, N.F. van Hulst, Visualizing and controlling vibrational wave packets of single molecules. *Nature*, **465**, 905-908 (2010)
2. R. Hildner, D. Brinks & N.F. van Hulst, Femtosecond coherence and quantum control of single molecules at room temperature. *Nature Physics*, **7**, 172-177 (2011)
3. D. Brinks, R. Hildner, F.D. Stefani & N.F. van Hulst, Coherent control of single molecules at room temperature, *Faraday Discussions*, **153**, 51-60 (2011)
4. D. Brinks, R. Hildner, F.D. Stefani & N.F. van Hulst, Beating Spatio-Temporal Coupling: implications for pulse shaping and coherent control experiments, *Optics Express* **19**, 26486-26499 (2011).
5. R. Hildner, D. Brinks, R.J. Cogdell & N. F. van Hulst, Persistent Quantum Coherence and Time-Varying Energy Transfer Pathways in Single Light-Harvesting Complexes, Under review with Nature
6. D. Brinks, M. Castro-Lopez, R. Hildner & N.F. van Hulst, Plasmonic antennas as design elements for coherent ultrafast nanophotonics, under review with Science

*Other relevant publications by the author:*

7. D. Brinks, F.D. Stefani & N.F. van Hulst, Nanoscale Spatial Effects of Pulse Shaping. *Ultrafast Phenomena XVI*, **92**, 890 (2009)
8. R. Hildner, D. Brinks, F.D. Stefani & N.F. van Hulst, Electronic coherences and vibrational wave-packets in single molecules studied with femtosecond phase-controlled spectroscopy. *Physical Chemistry Chemical Physics*, **13**, 1888-1894 (2011)
9. M. Castro-Lopez, D. Brinks, R. Sapienza & N.F. van Hulst, Aluminum for nonlinear plasmonics: resonance-driven polarized luminescence of Al, Ag, and Au nanoantennas. *Nano letters* **11**, 4674-4678 (2011)



## **Bibliography**

1. Moerner, W. & Kador, L. Optical detection and spectroscopy of single molecules in a solid. *Physical Review Letters* **62**, 2535–2538 (1989).
2. Wineland, D.J., Itano, W.M. & Bergquist, J.C. Absorption spectroscopy at the limit: detection of a single atom. *Optics letters* **12**, 389-91 (1987).
3. Hwang, J. *et al.* A single-molecule optical transistor. *Nature* **460**, 76-80 (2009).
4. Gerhardt, I. *et al.* Strong Extinction of a Laser Beam by a Single Molecule. *Physical Review Letters* **98**, 1-4 (2007).
5. Gaiduk, A., Yorulmaz, M., Ruijgrok, P.V. & Orrit, M. Room-temperature detection of a single molecule's absorption by photothermal contrast. *Science* **330**, 353-6 (2010).
6. Kukura, P., Celebrano, M., Renn, A. & Sandoghdar, V. Single-Molecule Sensitivity in Optical Absorption at Room Temperature. *The Journal of Physical Chemistry Letters* **1**, 3323-3327 (2010).
7. Celebrano, M., Kukura, P., Renn, A. & Sandoghdar, V. Single-molecule imaging by optical absorption. *Nature Photonics* **5**, 95-98 (2011).
8. Chong, S., Min, W. & Xie, X.S. Ground-State Depletion Microscopy: Detection Sensitivity of Single-Molecule Optical Absorption at Room Temperature. *The Journal of Physical Chemistry Letters* **1**, 3316-3322 (2010).
9. Min, W. *et al.* Imaging chromophores with undetectable fluorescence by stimulated emission microscopy. *Nature* **461**, 1105-9 (2009).
10. Orrit, M. & Bernard, J. Single pentacene molecules detected by fluorescence excitation in a p-terphenyl crystal. *Physical review letters* **65**, 2716–2719 (1990).
11. Güttler, F., Irngartinger, T., Plakhotnik, T., Renn, A. & Wild, U.P. Fluorescence microscopy of single molecules. *Chemical Physics Letters* **217**, 393-397 (1994).
12. Betzig, E. & Chichester, R.J. Single molecules observed by near-field scanning optical microscopy. *Science* **262**, 1422-5 (1993).

- 
13. Trautman, J.K., Macklin, J.J., Brus, L.E. & Betzig, E. Near-field spectroscopy of single molecules at room temperature. *Nature* **369**, 40-42 (1994).
  14. Ambrose, W., Goodwin, P., Martin, J. & Keller, R. Single molecule detection and photochemistry on a surface using near-field optical excitation. *Physical Review Letters* **72**, 160-163 (1994).
  15. Macklin, J., Trautman, J., Harris, T. & Brus, L. Imaging and time-resolved spectroscopy of single molecules at an interface. *Science* **272**, 255 (1996).
  16. Xie, X.S. & Dunn, R.C. Probing single molecule dynamics. *Science* **265**, 361-4 (1994).
  17. Lu, H.P. & Xie, X.S. Single-molecule spectral fluctuations at room temperature. *Nature* **385**, 143-146 (1997).
  18. Kulzer, F. & Orrit, M. Single-molecule optics. *Annual review of physical chemistry* **55**, 585-611 (2004).
  19. Moerner, W. & Fromm, D.P. Methods of single-molecule fluorescence spectroscopy and microscopy. *Review of Scientific Instruments* **74**, 3597 (2003).
  20. Betzig, E. Proposed method for molecular optical imaging. *Optics Letters* **20**, 237 (1995).
  21. Betzig, E. *et al.* Imaging intracellular fluorescent proteins at nanometer resolution. *Science* **313**, 1642-5 (2006).
  22. Rust, M.J., Bates, M. & Zhuang, X. Sub-diffraction-limit imaging by stochastic optical reconstruction microscopy (STORM). *Nature methods* **3**, 793-5 (2006).
  23. Minsky, M. US Patent Number 3013467: Microscopy apparatus. (1961).
  24. Tournois, P. Acousto-optic programmable dispersive filter for adaptive compensation of group delay time dispersion in laser systems. *Optics Communications* **140**, 245-249 (1997).
  25. Verluise, F., Laude, V., Cheng, Z., Spielmann, C. & Tournois, P. Amplitude and phase control of ultrashort pulses by use of an acousto-

- optic programmable dispersive filter□: pulse compression and shaping. *Optics Letters* **25**, 575–577 (2000).
26. Verluise, F., Laude, V., Huignard, J.P., Tournois, P. & Migus, A. Arbitrary dispersion control of ultrashort optical pulses with acoustic waves. *Journal of the Optical Society of America B* **17**, 138–145 (2000).
27. Guild, J.B., Xu, C. & Webb, W.W. Measurement of group delay dispersion of high numerical aperture objective lenses using two-photon excited fluorescence. *Applied Optics* **36**, 397–401 (1997).
28. Weiner, A.M., Leaird, D., Wiederrecht, G.P. & Nelson, K.A. Femtosecond pulse sequences used for optical manipulation of molecular motion. *Science* **247**, 1317-1319 (1990).
29. Weiner, A.M., Leaird, D.E., Patel, J.S. & Wullert, J.R. Programmable femtosecond pulse shaping by use of a multielement liquid-crystal phase modulator. *Optics letters* **15**, 326 (1990).
30. Weiner, A.M., Leaird, D.E., Patel, J.S. & Wullert, J.R. Programmable shaping of femtosecond optical pulses by use of 128-element liquid crystal phase modulator. *IEEE Journal of Quantum Electronics* **28**, 908-920 (1992).
31. Weiner, A.M. Femtosecond pulse shaping using spatial light modulators. *Review of Scientific Instruments* **71**, 1929 -1960 (2000).
32. Lozovoy, V., Pastirk, I. & Dantus, M. Multiphoton intrapulse interference. IV. Ultrashort laser pulse spectral phase characterization and compensation. *Optics letters* **29**, 775-777 (2004).
33. Walowicz, K.A., Pastirk, I., Lozovoy, V.V. & Dantus, M. Multiphoton intrapulse interference. I. Control of multiphoton processes in condensed phases. *Journal of Physical Chemistry A* **106**, 9369–9373 (2002).
34. Lozovoy, V.V., Pastirk, I., Walowicz, K. a. & Dantus, M. Multiphoton intrapulse interference. II. Control of two- and three-photon laser induced fluorescence with shaped pulses. *The Journal of Chemical Physics* **118**, 3187 (2003).
35. Dantus, M. & Lozovoy, V.V. Experimental coherent laser control of physicochemical processes. *Chemical Review* **104**, 1813-1859 (2004).

- 
36. Lozovoy, V.V. & Dantus, M. Systematic control of nonlinear optical processes using optimally shaped femtosecond pulses. *ChemPhysChem* **6**, 1970-2000 (2005).
  37. Xu, B., Gunn, J.M., Cruz, J.M.D., Lozovoy, V.V. & Dantus, M. Quantitative investigation of the multiphoton intrapulse interference phase scan method for simultaneous phase measurement and compensation of femtosecond laser pulses. *Journal of the Optical Society of America B* **23**, 750 (2006).
  38. Xu, B., Coello, Y., Lozovoy, V.V. & Dantus, M. Two-photon fluorescence excitation spectroscopy by pulse shaping ultrabroad-bandwidth femtosecond laser pulses. *Applied Optics* (2010).
  39. Pestov, D., Lozovoy, V.V. & Dantus, M. Single-beam shaper-based pulse characterization and compression using MIIPS sonogram. *Optics Letters* **35**, 1422–1424 (2010).
  40. Bowman, R., Dantus, M. & Zewail, A. Femtosecond transition-state spectroscopy of iodine: From strongly bound to repulsive surface dynamics. *Chemical Physics Letters* **161**, 297-302 (1989).
  41. Mukamel, S. *Principles of Nonlinear Optical Spectroscopy*. (Oxford University Press: New York, 1995).
  42. Mukamel, S. Multidimensional femtosecond correlation spectroscopies of electronic and vibrational excitations. *Annual review of physical chemistry* **51**, 691-729 (2000).
  43. Loudon, R. *The Quantum Theory of Light*. 448 (Oxford University Press: New York, 2000).
  44. Parson, W.W. *Modern Optical Spectroscopy*. (Springer: Dordrecht, 2007).
  45. Bhawalkar, J.D., He, G.S. & Prasad, P.N. Nonlinear multiphoton processes in organic and polymeric materials. *Reports on Progress in Physics* **59**, 1041-1070 (1996).
  46. Ritchie, R. Plasma Losses by Fast Electrons in Thin Films. *Physical Review* **106**, 874-881 (1957).
  47. Ebbesen, T., Lezec, H., Ghaemi, H. & Thio, T. Extraordinary optical transmission through sub-wavelength hole arrays. *Nature* **391**, 667-669 (1998).

48. Barnes, W.L., Dereux, A. & Ebbesen, T.W. Surface plasmon subwavelength optics. *Nature* **424**, 824-30 (2003).
49. Schuller, J. a *et al.* Plasmonics for extreme light concentration and manipulation. *Nature materials* **9**, 193-204 (2010).
50. Novotny, L. & van Hulst, N.F. Antennas for light. *Nature Photonics* **5**, 83-90 (2011).
51. Luk'yanchuk, B. *et al.* The Fano resonance in plasmonic nanostructures and metamaterials. *Nature Materials* **9**, 707-715 (2010).
52. Novotny, L. & Hecht, B. *Principles of Nano-Optics*. 560 (Cambridge University Press: 2006).
53. Maier, S.A. *Plasmonics: Fundamentals and Applications*. 248 (Springer: 2007).
54. Fischer, U. & Pohl, D. Observation of Single-Particle Plasmons by Near-Field Optical Microscopy. *Physical Review Letters* **62**, 458-461 (1989).
55. Betzig, E. & Trautman, J.K. Near-field optics: microscopy, spectroscopy, and surface modification beyond the diffraction limit. *Science* **257**, 189-95 (1992).
56. Novotny, L., Pohl, D. & Hecht, B. Light confinement in scanning near-field optical microscopy. *Ultramicroscopy* **61**, 1-9 (1995).
57. Hecht, B., Heinzlmann, H. & Pohl, D. Combined aperture SNOM/PSTM: best of both worlds? *Ultramicroscopy* **57**, 228-234 (1995).
58. Bouhelier, a. *et al.* Surface Plasmon Characteristics of Tunable Photoluminescence in Single Gold Nanorods. *Physical Review Letters* **95**, 4-7 (2005).
59. Balashov, S.P. *et al.* Xanthorhodopsin: a proton pump with a light-harvesting carotenoid antenna. *Science (New York, N.Y.)* **309**, 2061-4 (2005).
60. Mühlischlegel, P., Eisler, H.-J., Martin, O.J.F., Hecht, B. & Pohl, D.W. Resonant optical antennas. *Science* **308**, 1607-1609 (2005).

- 
61. Castro-Lopez, M., Brinks, D., Sapienza, R. & van Hulst, N.F. Aluminum for nonlinear plasmonics: resonance-driven polarized luminescence of Al, Ag, and Au nanoantennas. *Nano letters* **11**, 4674-4678 (2011).
  62. Taminiau, T., Stefani, F.D., Segerink, F. & Van, N. Optical antennas direct single-molecule emission. *Nature Photonics* 1-16 (2008).
  63. Curto, A.G. *et al.* Unidirectional Emission of a Quantum Dot Coupled to a Nanoantenna. *Science* **329**, 930-933 (2010).
  64. Prodan, E., Radloff, C., Halas, N.J. & Nordlander, P. A hybridization model for the plasmon response of complex nanostructures. *Science* **302**, 419-422 (2003).
  65. Fan, J.A. *et al.* Self-Assembled Plasmonic Nanoparticle Clusters. *Science* **328**, 1135-1138 (2010).
  66. Stockman, M., Faleev, S. & Bergman, D. Coherent Control of Femtosecond Energy Localization in Nanosystems. *Physical Review Letters* **88**, 067402 (2002).
  67. Stockman, M.I., Kling, M.F., Kleineberg, U. & Krausz, F. Attosecond nanoplasmonic-field microscope. *Nature Photonics* **1**, 539-544 (2007).
  68. Stockman, M., Bergman, D. & Kobayashi, T. Coherent control of nanoscale localization of ultrafast optical excitation in nanosystems. *Physical Review B* **69**, 054202 (2004).
  69. Durach, M., Rusina, A., Stockman, M.I. & Nelson, K. Toward full spatiotemporal control on the nanoscale. *Nano letters* **7**, 3145-3149 (2007).
  70. Meshulach, D. & Silberberg, Y. Coherent quantum control of two-photon transitions by a femtosecond laser pulse. *Nature* **396**, 239-242 (1998).
  71. Herek, J.L., Wohlleben, W., Cogdell, R., Zeidler, D. & Motzkus, M. Quantum control of energy flow in light harvesting. *Nature* **417**, 533-535 (2002).
  72. Prokhorenko, V.I. *et al.* Coherent control of retinal isomerization in bacteriorhodopsin. *Science* **313**, 1257 (2006).

73. Voronine, D.V., Abramavicius, D. & Mukamel, S. Coherent control protocol for separating energy-transfer pathways in photosynthetic complexes by chiral multidimensional signals. *The journal of physical chemistry. A* **115**, 4624-9 (2011).
74. Assion, A. *et al.* Control of chemical reactions by feedback-optimized phase-shaped femtosecond laser pulses. *Science* **282**, 919 (1998).
75. Brixner, T. & Gerber, G. Quantum control of gas-phase and liquid-phase femtochemistry. *ChemPhysChem* **4**, 418–438 (2003).
76. Stanciu, C. *et al.* All-Optical Magnetic Recording with Circularly Polarized Light. *Physical Review Letters* **99**, 1-4 (2007).
77. Hillerkuss, D. *et al.* 26 Tbit s<sup>-1</sup> line-rate super-channel transmission utilizing all-optical fast Fourier transform processing. *Nature Photonics* **5**, 364-371 (2011).
78. Jiang, Z., Huang, C.-B., Leaird, D.E. & Weiner, A.M. Optical arbitrary waveform processing of more than 100 spectral comb lines. *Nature Photonics* **1**, 463-467 (2007).
79. Král, P., Thanopoulos, I. & Shapiro, M. Coherently controlled adiabatic passage. *Reviews of Modern Physics* **79**, 53-77 (2007).
80. Greentree, A., Devitt, S. & Hollenberg, L. Quantum-information transport to multiple receivers. *Physical Review A* **73**, 1-5 (2006).
81. Rabitz, H., de Vivie-Riedle, R., Motzkus, M. & Kompa, K. Whither the future of controlling quantum phenomena? *Science* **288**, 824 (2000).
82. Kuroda, D.G., Singh, C.P., Peng, Z. & Kleiman, V.D. Mapping excited-state dynamics by coherent control of a dendrimer's photoemission efficiency. *Science* **326**, 263-7 (2009).
83. Engel, G.S. *et al.* Evidence for wavelike energy transfer through quantum coherence in photosynthetic systems. *Nature* **446**, 782-786 (2007).
84. Collini, E. *et al.* Coherently wired light-harvesting in photosynthetic marine algae at ambient temperature. *Nature* **463**, 644–647 (2010).
85. Brinks, D. *et al.* Visualizing and controlling vibrational wave packets of single molecules. *Nature* **465**, 905-908 (2010).

- 
86. Hildner, R., Brinks, D. & van Hulst, N.F. Femtosecond coherence and quantum control of single molecules at room temperature. *Nature Physics* **7**, 172-177 (2011).
  87. Saar, B.G. *et al.* Video-rate molecular imaging in vivo with stimulated Raman scattering. *Science* **330**, 1368-70 (2010).
  88. Freudiger, C.W. *et al.* Highly specific label-free molecular imaging with spectrally tailored excitation-stimulated Raman scattering (STE-SRS) microscopy. *Nature Photonics* **5**, 103-109 (2011).
  89. Zeidler, D., Hornung, T., Proch, D. & Motzkus, M. Adaptive compression of tunable pulses from a non-collinear-type OPA to below 16 fs by feedback-controlled pulse shaping. *Applied Physics B: Lasers and Optics* **131**, 125-131 (2000).
  90. Tan, H.-S., Schreiber, E. & Warren, W.S. High-resolution indirect pulse shaping by parametric transfer. *Optics letters* **27**, 439-41 (2002).
  91. Lorenc, D., Velic, D., Markevitch, A. & Levis, R. Adaptive femtosecond pulse shaping to control supercontinuum generation in a microstructure fiber. *Optics Communications* **276**, 288–292 (2007).
  92. Ganz, T., Pervak, V., Apolonski, a & Baum, P. 16 fs, 350 nJ pulses at 5 MHz repetition rate delivered by chirped pulse compression in fibers. *Optics letters* **36**, 1107-9 (2011).
  93. Martinez, O.E., Gordon, J.P. & Fork, R.L. Negative group-velocity dispersion using refraction. *Journal of the Optical Society of America A* **1**, 1003-1006 (1984).
  94. Treacy, E. Optical pulse compression with diffraction gratings. *IEEE Journal of Quantum Electronics* **5**, 454-458 (1969).
  95. Martinez, O. Design of high-power ultrashort pulse amplifiers by expansion and recompression. *IEEE Journal of Quantum Electronics* **23**, 1385–1387 (1987).
  96. Szipocs, R., Ferencz, K., Spielmann, C. & Krausz, F. Chirped multilayer coatings for broadband dispersion control in femtosecond lasers. *Optics Letters* **19**, 201-203 (1994).
  97. Brixner, T. & Gerber, G. Femtosecond polarization pulse shaping. *Optics letters* **26**, 557-559 (2001).

98. Aeschlimann, M. *et al.* Adaptive subwavelength control of nano-optical fields. *Nature* **446**, 301-4 (2007).
99. Tian, P., Keusters, D., Suzuki, Y. & Warren, W.S. Femtosecond phase-coherent two-dimensional spectroscopy. *Science* **300**, 1553-5 (2003).
100. Krebs, N., Probst, R. a & Riedle, E. Sub-20 fs pulses shaped directly in the UV by an acousto-optic programmable dispersive filter. *Optics express* **18**, 6164-71 (2010).
101. Dixon, R. Acoustic diffraction of light in anisotropic media. *IEEE Journal of Quantum Electronics* **3**, 85–93 (1967).
102. Dorrer, C. & Salin, F. Phase amplitude coupling in spectral phase modulation. *IEEE Journal of Selected Topics in Quantum Electronics* **4**, 342-345 (1998).
103. Tanabe, T., Tanabe, H., Teramura, Y. & Kannari, F. Spatiotemporal measurements based on spatial spectral interferometry for ultrashort optical pulses shaped by a Fourier pulse shaper. *Journal of the Optical Society of America B* **19**, 2795-2802 (2002).
104. Monmayrant, A., Weber, S. & Chatel, B. A newcomer's guide to ultrashort pulse shaping and characterization. *Journal of Physics B: Atomic, Molecular and Optical Physics* **43**, 103001 (2010).
105. McCabe, D.J. *et al.* Space–time coupling of shaped ultrafast ultraviolet pulses from an acousto-optic programmable dispersive filter. *Journal of the Optical Society of America B* **28**, 58 (2010).
106. Martinez, O.E. Grating and prism compressors in the case of finite beam size. *Journal of the Optical Society of America B* **3**, 929–934 (1986).
107. Bonadeo, N. *et al.* Coherent optical control of the quantum state of a single quantum dot. *Science* **282**, 1473-1476 (1998).
108. Brinks, D., Stefani, F.D. & van Hulst, N.F. Nanoscale spatial effects of pulse shaping. *Ultrafast Phenomena XVI* **92**, 890 (2009).
109. Sussman, B., Lausten, R. & Stolow, A. Focusing of light following a 4-f pulse shaper: Considerations for quantum control. *Physical Review A* **77**, 043416 (2008).

- 
110. Frei, F., Bloch, R. & Feurer, T. Influence of finite spatial resolution on single- and double-pass femtosecond pulse shapers. *Optics Letters* **35**, 4072-4074 (2010).
  111. Goodman, J.W. *Introduction to Fourier Optics*. (Roberts & Company Publishers: Englewood, Colorado, 2005).
  112. Wefers, M. & Nelson, K. Space-time profiles of shaped ultrafast optical waveforms. *IEEE Journal of Quantum Electronics* **32**, 161–172 (1996).
  113. Anderson, A., Deryckx, K.S., Xu, X.G., Steinmeyer, G. & Raschke, M.B. Few-femtosecond plasmon dephasing of a single metallic nanostructure from optical response function reconstruction by interferometric frequency resolved optical gating. *Nano letters* **10**, 2519-2524 (2010).
  114. Sadiq, D. *et al.* Adiabatic Nanofocusing Scattering-Type Optical Nanoscopy of Individual Gold Nanoparticles. *Nano letters* **11**, 1609-13 (2011).
  115. Hildner, R., Brinks, D., Stefani, F.D. & van Hulst, N.F. Electronic coherences and vibrational wave-packets in single molecules studied with femtosecond phase-controlled spectroscopy. *Physical Chemistry Chemical Physics* **13**, 1888-94 (2011).
  116. Strickland, D. & Mourou, G. Compression of amplified chirped optical pulses. *Optics Communications* **56**, 219-221 (1985).
  117. Wefers, M.M. & Nelson, K. a. Analysis of programmable ultrashort waveform generation using liquid-crystal spatial light modulators. *Journal of the Optical Society of America B* **12**, 1343 (1995).
  118. Avlasevich, Y., Müller, S., Erk, P. & Müllen, K. Novel core-expanded rylenebis (dicarboximide) dyes bearing pentacene units: Facile synthesis and photophysical properties. *Chemistry-A European Journal* **13**, 6555–6561 (2007).
  119. Ladd, T.D. *et al.* Quantum computers. *Nature* **464**, 45-53 (2010).
  120. Buluta, I. & Nori, F. Quantum simulators. *Science* **326**, 108-11 (2009).
  121. Bennett, C. & DiVincenzo, D. Quantum information and computation. *Nature* **404**, 247-55 (2000).

122. Hosaka, K. *et al.* Ultrafast Fourier Transform with a Femtosecond-Laser-Driven Molecule. *Physical Review Letters* **104**, 180501 (2010).
123. Lee, H., Cheng, Y.-C. & Fleming, G.R. Coherence dynamics in photosynthesis: protein protection of excitonic coherence. *Science* **316**, 1462-1465 (2007).
124. Panitchayangkoon, G. *et al.* Long-lived quantum coherence in photosynthetic complexes at physiological temperature. *Proceedings of the National Academy of Sciences of the United States of America* **107**, 12766-70 (2010).
125. Scholes, G.D. Quantum-Coherent Electronic Energy Transfer: Did Nature Think of It First? *The Journal of Physical Chemistry Letters* **1**, 2-8 (2010).
126. Sarovar, M., Ishizaki, A., Fleming, G.R. & Whaley, K.B. Quantum entanglement in photosynthetic light-harvesting complexes. *Nature Physics* **5**, 1-6 (2010).
127. Abramavicius, D. & Mukamel, S. Quantum oscillatory exciton migration in photosynthetic reaction centers. *The Journal of Chemical Physics* **133**, 064510 (2010).
128. Mukamel, S. Signatures of quasiparticle entanglement in multidimensional nonlinear optical spectroscopy of aggregates. *The Journal of chemical physics* **132**, 241105 (2010).
129. van Dijk, E.M.H.P. *et al.* Single-molecule pump-probe detection resolves ultrafast pathways in individual and coupled quantum systems. *Physical review letters* **94**, 78302 (2005).
130. Gerhardt, I. *et al.* Coherent state preparation and observation of Rabi oscillations in a single molecule. *Physical Review A* **79**, 11402 (2009).
131. Wrigge, G., Gerhardt, I., Hwang, J., Zumofen, G. & Sandoghdar, V. Efficient coupling of photons to a single molecule and the observation of its resonance fluorescence. *Nature Physics* **4**, 60-66 (2007).
132. Kamada, H., Gotoh, H., Temmyo, J., Takagahara, T. & Ando, H. Exciton Rabi Oscillation in a Single Quantum Dot. *Physical Review Letters* **87**, 246401 (2001).

- 
133. Htoon, H. *et al.* Interplay of Rabi Oscillations and Quantum Interference in Semiconductor Quantum Dots. *Physical Review Letters* **88**, 087401 (2002).
134. Childress, L. *et al.* Coherent dynamics of coupled electron and nuclear spin qubits in diamond. *Science* **314**, 281-285 (2006).
135. Celebrano, M., Kukura, P., Renn, A. & Sandoghdar, V. Single-molecule imaging by optical absorption. *Nature Photonics* **5**, 95-98 (2011).
136. Feynman, R.P., Vernon, F.L. & Hellwarth, R.W. Geometrical Representation of the Schrödinger Equation for Solving Maser Problems. *Journal of Applied Physics* **28**, 49 (1957).
137. Allen, L. & Eberly, J.H. *Optical Resonance and Two-Level atoms*. (Dover: New York, 1987).
138. Zewail, A.H. Optical molecular dephasing: principles of and probings by coherent laser spectroscopy. *Accounts of Chemical Research* **13**, 360-368 (1980).
139. Mais, S. *et al.* Terrylenediimide: A novel fluorophore for single-molecule spectroscopy and microscopy from 1.4 K to room temperature. *Journal of Physical Chemistry A* **101**, 8435-8440 (1997).
140. Schweitzer, G. *et al.* Intramolecular Directional Energy Transfer Processes in Dendrimers Containing Perylene and Terrylene Chromophores †. *The Journal of Physical Chemistry A* **107**, 3199-3207 (2003).
141. Fourkas, J.T., Wilson, W.L., Wäckerle, G., Frost, A.E. & Fayer, M. Picosecond time-scale phase-related optical pulses: measurement of sodium optical coherence decay by observation of incoherent fluorescence. *Journal of the Optical Society of America B* **6**, 1905-1910 (1989).
142. Brewer, R. & Genack, A. Optical Coherent Transients by Laser Frequency Switching. *Physical Review Letters* **36**, 959-962 (1976).
143. Balasubramanian, G. *et al.* Ultralong spin coherence time in isotopically engineered diamond. *Nature materials* **8**, 383-7 (2009).
144. Collini, E. & Scholes, G.D. Coherent intrachain energy migration in a conjugated polymer at room temperature. *science* **323**, 369 (2009).

145. Zewail, A.H. Femtochemistry: atomic-scale dynamics of the chemical bond. *Journal of Physical Chemistry A* **104**, 5660 (2000).
146. Moerner, W. A dozen years of single-molecule spectroscopy in physics, chemistry, and biophysics. *Journal of Physical Chemistry B* **106**, 910–927 (2002).
147. Michalet, X., Weiss, S. & Jäger, M. Single-molecule fluorescence studies of protein folding and conformational dynamics. *Chemical Review* **106**, 1785–1813 (2006).
148. Lu, H.P., Xun, L. & Xie, X.S. Single-molecule enzymatic dynamics. *Science* **282**, 1877 (1998).
149. Yildiz, A. *et al.* Myosin V walks hand-over-hand: single fluorophore imaging with 1.5-nm localization. *Science* **300**, 2061 (2003).
150. Elf, J., Li, G.-W. & Xie, X.S. Probing transcription factor dynamics at the single-molecule level in a living cell. *Science* **316**, 1191–4 (2007).
151. Zondervan, R., Kulzer, F., Berkhout, G.C.G. & Orrit, M. Local viscosity of supercooled glycerol near T<sub>g</sub> probed by rotational diffusion of ensembles and single dye molecules. *Proceedings of the National Academy of Sciences of the United States of America* **104**, 12628 (2007).
152. Barbara, P.F., Gesquiere, A.J., Park, S.J. & Lee, Y.J. Single-molecule spectroscopy of conjugated polymers. *Accounts of Chemical Research* **38**, 602–610 (2005).
153. Hell, S.W. & Wichmann, J. Breaking the diffraction resolution limit by stimulated emission: stimulated-emission-depletion fluorescence microscopy. *Optics Letters* **19**, 780 (1994).
154. Hell, S.W. Far-field optical nanoscopy. *Science* **316**, 1153–8 (2007).
155. Hugel, T. *et al.* Single-molecule optomechanical cycle. *Science* **296**, 1103 (2002).
156. Kulzer, F., Kummer, S., Matzke, R., Bräuchle, C. & Basché, T. Single-molecule optical switching of terrylene in p-terphenyl. *Nature* **387**, 688–691 (1997).
157. Hoogenboom, J.P., van Dijk, E.M.H.P., Hernando, J., van Hulst, N.F. & García-Parajó, M.F. Power-law-distributed dark states are the main

- 
- pathway for photobleaching of single organic molecules. *Physical review letters* **95**, 97401 (2005).
158. Hofmann, C., Aartsma, T.J., Michel, H. & Köhler, J. Direct observation of tiers in the energy landscape of a chromoprotein: a single-molecule study. *Proceedings of the National Academy of Sciences of the United States of America* **100**, 15534-8 (2003).
159. Hoogenboom, J.P. *et al.* The single molecule probe: nanoscale vectorial mapping of photonic mode density in a metal nanocavity. *Nano letters* **9**, 1189-95 (2009).
160. Cohen, A.E. & Moerner, W.E. Controlling Brownian motion of single protein molecules and single fluorophores in aqueous buffer. *Optics express* **16**, 6941-56 (2008).
161. Hettich, C. *et al.* Nanometer resolution and coherent optical dipole coupling of two individual molecules. *Science* **298**, 385 (2002).
162. Kastrop, L. & Hell, S.W. Absolute optical cross section of individual fluorescent molecules. *Angewandte Chemie International Edition* **43**, 6646–6649 (2004).
163. Shapiro, M. & Brumer, P. Coherent control of molecular dynamics. *Reports on Progress in Physics* **66**, 859–942 (2003).
164. Judson, R.S. & Rabitz, H. Teaching lasers to control molecules. *Physical Review Letters* **68**, 1500–1503 (1992).
165. Warren, W.S., Rabitz, H. & Dahleh, M. Coherent control of quantum dynamics: the dream is alive. *Science* **259**, 1581 (1993).
166. Gross, P., Singh, H., Rabitz, H., Mease, K. & Huang, G. Inverse quantum-mechanical control: A means for design and a test of intuition. *Physical Review A* **47**, 4593–4604 (1993).
167. Bardeen, C.J. *et al.* Feedback quantum control of molecular electronic population transfer. *Chemical Physics Letters* **280**, 151-158 (1997).
168. Dudovich, N., Oron, D. & Silberberg, Y. Single-pulse coherently controlled nonlinear Raman spectroscopy and microscopy. *Nature* **418**, 512–514 (2002).

169. Bartels, R.A. *et al.* Shaped-pulse optimization of coherent emission of high-harmonic soft X-rays. *Nature* **406**, 164–166 (2000).
170. Brinks, D., Hildner, R., Stefani, F.D. & van Hulst, N.F. Beating spatio-temporal coupling: implications for pulse shaping and coherent control experiments. *Optics Express* **19**, 26486-26499 (2011).
171. Amstrup, B., Carlson, R.J., Matro, A. & Rice, S.A. Use of pulse shaping to control the photodissociation of a diatomic molecule: preventing the best from being the enemy of the good. *The Journal of Physical Chemistry* **95**, 8019–8027 (1991).
172. Hornung, T., Motzkus, M. & de Vivie-Riedle, R. Teaching Optimal Control Theory to distill robust pulses even under experimental constraints. *Physical Review A* **65**, 21403 (2002).
173. Scherer, N.F. *et al.* Fluorescence-detected wave packet interferometry: Time resolved molecular spectroscopy with sequences of femtosecond phase-locked pulses. *The Journal of Chemical Physics* **95**, 1487 (1991).
174. Scherer, N. *et al.* Fluorescence-detected wave packet interferometry. II. Role of rotations and determination of the susceptibility. *The Journal of Chemical Physics* **96**, 4180 (1992).
175. Yuen-Zhou, J. & Aspuru-Guzik, A. Quantum process tomography of excitonic dimers from two-dimensional electronic spectroscopy. I. General theory and application to homodimers. *The Journal of chemical physics* **134**, 134505 (2011).
176. Burgarth, D., Maruyama, K. & Nori, F. Indirect quantum tomography of quadratic Hamiltonians. *New Journal of Physics* **13**, 013019 (2011).
177. Cai, J. Quantum Probe and Design for a Chemical Compass with Magnetic Nanostructures. *Physical Review Letters* **106**, 100501 (2011).
178. Vaziri, A. & Plenio, M.B. Quantum coherence in ion channels: resonances, transport and verification. *New Journal of Physics* **12**, 085001 (2010).
179. Brookes, J., Hartoutsiou, F., Horsfield, A. & Stoneham, A. Could Humans Recognize Odor by Phonon Assisted Tunneling? *Physical Review Letters* **98**, 038101 (2007).

- 
180. Gegear, R.J., Casselman, A., Waddell, S. & Reppert, S.M. Cryptochrome mediates light-dependent magnetosensitivity in *Drosophila*. *Nature* **454**, 1014-1018 (2008).
181. Cai, J., Guerreschi, G.G. & Briegel, H.J. Quantum Control and Entanglement in a Chemical Compass. *Physical Review Letters* **104**, 220502 (2010).
182. Maeda, K. *et al.* Chemical compass model of avian magnetoreception. *Nature* **453**, 387-90 (2008).
183. Gauger, E., Rieper, E., Morton, J., Benjamin, S. & Vedral, V. Sustained Quantum Coherence and Entanglement in the Avian Compass. *Physical Review Letters* **106**, 040503 (2011).
184. Rieper, E. Quantum Coherence in Biological Systems. (2011).
185. McDermott, G. *et al.* Crystal structure of an integral membrane light-harvesting complex from photosynthetic bacteria. *Nature* **374**, 517-521 (1995).
186. Bahatyrova, S. *et al.* The native architecture of a photosynthetic membrane. *Nature* **430**, 1058–1062 (2004).
187. Cogdell, R.J., Gall, A. & Köhler, J. The architecture and function of the light-harvesting apparatus of purple bacteria: from single molecules to in vivo membranes. *Quarterly reviews of biophysics* **39**, 227-324 (2006).
188. van Grondelle, R. & Novoderezhkin, V.I. Energy transfer in photosynthesis: experimental insights and quantitative models. *Physical Chemistry Chemical Physics* **8**, 793-807 (2006).
189. Kennis, J.T.M., Streltsov, A.M., Aartsma, T.J., Nozawa, T. & Ames, J. Energy Transfer and Exciton Coupling in Isolated B800–850 Complexes of the Photosynthetic Purple Sulfur Bacterium *Chromatium tepidum*. The Effect of Structural Symmetry on Bacteriochlorophyll Excited States. *The Journal of Physical Chemistry* **100**, 2438-2442 (1996).
190. Kennis, J.T.M., Streltsov, A.M., Permentier, H., Aartsma, T.J. & Ames, J. Exciton Coherence and Energy Transfer in the LH2 Antenna Complex of *Rhodospseudomonas acidophila* at Low Temperature. *The Journal of Physical Chemistry B* **101**, 8369-8374 (1997).

191. Kennis, J.T.M. *et al.* Femtosecond Dynamics in Isolated LH2 Complexes of Various Species of Purple Bacteria. *The Journal of Physical Chemistry B* **101**, 7827-7834 (1997).
192. Wu, H.-M. *et al.* Femtosecond and Hole-Burning Studies of B800's Excitation Energy Relaxation Dynamics in the LH2 Antenna Complex of *Rhodospseudomonas acidophila* (Strain 10050). *The Journal of Physical Chemistry* **100**, 12022-12033 (1996).
193. Reddy, N.R.S., Small, G.J., Seibert, M. & Picorel, R. Energy transfer dynamics of the B800-B850 antenna complex of *Rhodobacter sphaeroides*: a hole burning study. *Chemical Physics Letters* **18**, 391-399 (1991).
194. Reddy, N.R.S., Picorel, R. & Small, G.J. B896 and B870 components of the *Rhodobacter sphaeroides* antenna: a hole burning study. *The Journal of Physical Chemistry* **96**, 6458-6464 (1992).
195. Reddy, N.R.S. *et al.* High pressure studies of energy transfer and strongly coupled bacteriochlorophyll dimers in photosynthetic protein complexes. *Photosynthesis Research* **48**, 277-289 (1996).
196. Nantakalaksakul, A., Reddy, D.R., Bardeen, C.J. & Thayumanavan, S. Light harvesting dendrimers. *Photosynthesis research* **87**, 133-150 (2006).
197. Polivka, T. *et al.* The carotenoid S1 state in LH2 complexes from purple bacteria *Rhodobacter sphaeroides* and *Rhodospseudomonas acidophila*: S1 energies, dynamics, and carotenoid radical formation. *Journal of Physical Chemistry B* **106**, 11016–11025 (2002).
198. Wohlleben, W., Buckup, T., Herek, J.L., Cogdell, R. & Motzkus, M. Multichannel carotenoid deactivation in photosynthetic light harvesting as identified by an evolutionary target analysis. *Biophysical journal* **85**, 442–450 (2003).
199. Herek, J.L. *et al.* B800-->B850 energy transfer mechanism in bacterial LH2 complexes investigated by B800 pigment exchange. *Biophysical journal* **78**, 2590-6 (2000).
200. Schubert, A. *et al.* In vitro self-assembly of the light harvesting pigment-protein LH2 revealed by ultrafast spectroscopy and electron microscopy. *Biophysical journal* **86**, 2363–2373 (2004).

- 
201. Herek, J.L. *et al.* Ultrafast Carotenoid Band Shifts: Experiment and Theory. *Journal of Physical Chemistry B* **108**, 10398–10403 (2004).
  202. Pullerits, T., Hess, S., Herek, J.L. & Sundström, V. Temperature Dependence of Excitation Transfer in LH2 of Rhodobacter sphaeroides. *The Journal of Physical Chemistry B* **101**, 10560-10567 (1997).
  203. Wohlleben, W. *et al.* Pump- Deplete- Probe Spectroscopy and the Puzzle of Carotenoid Dark States. *Journal of Physical Chemistry B* **108**, 3320–3325 (2004).
  204. Kosumi, D. *et al.* Ultrafast energy-transfer pathway in a purple-bacterial photosynthetic core antenna, as revealed by femtosecond time-resolved spectroscopy. *Angewandte Chemie International Edition* **50**, 1097-100 (2011).
  205. Scholes, G.D. & Fleming, G.R. On the Mechanism of Light Harvesting in Photosynthetic Purple Bacteria: B800 to B850 Energy Transfer. *The Journal of Physical Chemistry B* **104**, 1854-1868 (2000).
  206. Scholes, G.D., Gould, I.R., Cogdell, R.J. & Fleming, G.R. Ab Initio Molecular Orbital Calculations of Electronic Couplings in the LH2 Bacterial Light-Harvesting Complex of Rps. Acidophila. *The Journal of Physical Chemistry B* **103**, 2543-2553 (1999).
  207. Turner, D.B., Wilk, K.E., Curmi, P.M.G. & Scholes, G.D. Comparison of Electronic and Vibrational Coherence Measured by Two-Dimensional Electronic Spectroscopy. *The Journal of Physical Chemistry Letters* **2**, 1904-1911 (2011).
  208. Scholes, G.D. Long-range resonance energy transfer in molecular systems. *Annual review of physical chemistry* **54**, 57-87 (2003).
  209. Wong, C.Y. *et al.* Electronic coherence lineshapes reveal hidden excitonic correlations in photosynthetic light harvesting. *Nature Chemistry* **4**, 396-404 (2012).
  210. Beljonne, D., Curutchet, C., Scholes, G.D. & Silbey, R.J. Beyond Förster resonance energy transfer in biological and nanoscale systems. *The journal of physical chemistry. B* **113**, 6583-99 (2009).
  211. Curutchet, C. *et al.* Photosynthetic light-harvesting is tuned by the heterogeneous polarizable environment of the protein. *Journal of the American Chemical Society* **133**, 3078-84 (2011).

212. Brixner, T. *et al.* Two-dimensional spectroscopy of electronic couplings in photosynthesis. *Nature* **434**, 625–628 (2005).
213. Harel, E. & Engel, G.S. Quantum coherence spectroscopy reveals complex dynamics in bacterial light-harvesting complex 2 (LH2). *Proceedings of the National Academy of Sciences of the United States of America* **109**, 706-11 (2012).
214. Rebentrost, P., Mohseni, M., Kassal, I., Lloyd, S. & Aspuru-Guzik, A. Environment-assisted quantum transport. *New Journal of Physics* **11**, 033003 (2009).
215. Plenio, M.B. & Huelga, S.F. Dephasing-assisted transport: quantum networks and biomolecules. *New Journal of Physics* **10**, 113019 (2008).
216. Mohseni, M., Rebentrost, P., Lloyd, S. & Aspuru-Guzik, A. Environment-assisted quantum walks in photosynthetic energy transfer. *The Journal of chemical physics* **129**, 174106 (2008).
217. Hoyer, S., Ishizaki, A. & Whaley, K.B. Propagating quantum coherence for a biological advantage. *Arxiv preprint* 1106.2911 (2011).
218. Bopp, M.A., Sytnik, A., Howard, T.D., Cogdell, R.J. & Hochstrasser, R.M. The dynamics of structural deformations of immobilized single light-harvesting complexes. *Proceedings of the National Academy of Sciences of the United States of America* **96**, 11271-6 (1999).
219. van Oijen, A.M., Ketelaars, M., Köhler, J., Aartsma, T.J. & Schmidt, J. Unraveling the electronic structure of individual photosynthetic pigment-protein complexes. *Science* **285**, 400 (1999).
220. Rutkauskas, D., Novoderezhkin, V., Cogdell, R.J. & van Grondelle, R. Fluorescence spectral fluctuations of single LH2 complexes from *Rhodospseudomonas acidophila* strain 10050. *Biochemistry* **43**, 4431-8 (2004).
221. Rutkauskas, D. *et al.* Spectral trends in the fluorescence of single bacterial light-harvesting complexes: experiments and modified redfield simulations. *Biophysical journal* **90**, 2475-85 (2006).
222. Pflock, T.J. *et al.* The electronically excited states of LH2 complexes from *Rhodospseudomonas acidophila* strain 10050 studied by time-resolved spectroscopy and dynamic Monte Carlo simulations. II. Homomembranes of LH2 complexes reconstituted into phospholipid model membranes. *The journal of physical chemistry. B* **115**, 8821-31 (2011).

- 
223. Ilioaia, C. *et al.* Photoprotection in plants involves a change in lutein 1 binding domain in the major light-harvesting complex of photosystem II. *The Journal of biological chemistry* **286**, 27247-54 (2011).
224. Gall, A. *et al.* Molecular adaptation of photoprotection: triplet states in light-harvesting proteins. *Biophysical journal* **101**, 934-42 (2011).
225. Prokhorenko, V.I., Nagy, A.M., Brown, L.S. & Miller, R. On the mechanism of weak-field coherent control of retinal isomerization in bacteriorhodopsin. *Chemical Physics* **341**, 296–309 (2007).
226. Shapiro, M. & Brumer, P. The equivalence of unimolecular decay product yields in pulsed and cw laser excitation. *The Journal of chemical physics* **84**, 540-541 (1986).
227. Shapiro, M. & Brumer, P. Laser control of product quantum state populations in unimolecular reactions. *The Journal of Chemical Physics* **84**, 4103 (1986).
228. Katz, G., Ratner, M. a & Kosloff, R. Control by decoherence: weak field control of an excited state objective. *New Journal of Physics* **12**, 015003 (2010).
229. Hoki, K. & Brumer, P. Dissipation effects on laser control of cis/trans isomerization. *Chemical Physics Letters* **468**, 23-27 (2009).
230. Brumer, P. & Shapiro, M. Control of unimolecular reactions using coherent light. *Chemical Physics Letters* **126**, 541–546 (1986).
231. Han, A. & Shapiro, M. Linear Response in the Strong Field Domain. *Physical Review Letters* **108**, 1-5 (2012).
232. Hawthornthwaite, A.M. & Cogdell, R.J. Bacteriochlorophyll-binding proteins. *Chlorophylls* 493-528 (1991).
233. Cherepy, N.J., Shreve, A.P., Moore, L.J., Boxer, S.G. & Mathies, R.A. Electronic and Nuclear Dynamics of the Accessory Bacteriochlorophylls in Bacterial Photosynthetic Reaction Centers from Resonance Raman Intensities. **5647**, 3250-3260 (1997).
234. Nagarajan, V., Alden, R.G., Williams, J.C. & Parson, W.W. Ultrafast exciton relaxation in the B850 antenna complex of Rhodobacter sphaeroides. *Proceedings of the National Academy of Sciences of the United States of America* **93**, 13774-9 (1996).

235. Trinkunas, G. *et al.* Exciton Band Structure in Bacterial Peripheral Light-Harvesting Complexes. (2012).
236. Hofmann, C., Michel, H., van Heel, M. & Köhler, J. Multivariate Analysis of Single-Molecule Spectra: Surpassing Spectral Diffusion. *Physical Review Letters* **94**, 1-4 (2005).
237. Sumi, H. Bacterial photosynthesis begins with quantum-mechanical coherence. *Chemical record* **1**, 480-93 (2001).
238. Ketelaars, M. *et al.* Spectroscopy on the B850 band of individual light-harvesting 2 complexes of *Rhodospseudomonas acidophila*. I. Experiments and Monte Carlo simulations. *Biophysical journal* **80**, 1591-1603 (2001).
239. Matsushita, M. *et al.* Spectroscopy on the B850 band of individual light-harvesting 2 complexes of *Rhodospseudomonas acidophila*. II. Exciton states of an elliptically deformed ring aggregate. *Biophysical journal* **80**, 1604-1614 (2001).
240. Aharonov, Y. & Bohm, D. Time in the Quantum Theory and the Uncertainty Relation for Time and Energy. *Physical Review* **122**, 1649-1658 (1961).
241. de Vries, H. & Wiersma, D.A. Photophysical and photochemical molecular hole burning theory. *The Journal of Chemical Physics* **72**, 1851 (1980).
242. Brinks, D., Hildner, R., Stefani, F.D. & van Hulst, N.F. Coherent control of single molecules at room temperature. *Faraday Discussions* **153**, 51 (2011).
243. Huang, J., Voronine, D., Tuchscherer, P., Brixner, T. & Hecht, B. Deterministic spatiotemporal control of optical fields in nanoantennas and plasmonic circuits. *Physical Review B* **79**, 195441 (2009).
244. Aeschlimann, M. *et al.* Spatiotemporal control of nanooptical excitations. *Proceedings of the National Academy of Sciences of the United States of America* **107**, 5329-5333 (2010).
245. Hanke, T. *et al.* Efficient nonlinear light emission of single gold optical antennas driven by few-cycle near-infrared pulses. *Physical Review Letters* **103**, 257404 (2009).

- 
246. Aeschlimann, M. *et al.* Coherent Two-Dimensional Nanoscopy. *Science* **333**, 1723-1726 (2011).
  247. Guenther, T. *et al.* Coherent Nonlinear Optical Response of Single Quantum Dots Studied by Ultrafast Near-Field Spectroscopy. *Physical Review Letters* **89**, 057401 (2002).
  248. Berweger, S., Atkin, J.M., Xu, X.G., Olmon, R.L. & Raschke, M.B. Femtosecond nano-focusing with full optical waveform control. *Nano letters* **11**, 4309-13 (2011).
  249. Vasa, P., Ropers, C., Pomraenke, R. & Lienau, C. Ultra-fast nano-optics. *Laser & Photonics Review* **3**, 483-507 (2009).
  250. Kalkbrenner, T. *et al.* Optical Microscopy via Spectral Modifications of a Nanoantenna. *Physical Review Letters* **95**, 200801 (2005).
  251. Beversluis, M., Bouhelier, A. & Novotny, L. Continuum generation from single gold nanostructures through near-field mediated intraband transitions. *Physical Review B* **68**, 115433 (2003).
  252. Nelayah, J. *et al.* Mapping surface plasmons on a single metallic nanoparticle. *Nature Physics* **3**, 348-353 (2007).
  253. Verhagen, E., Spasenović, M., Polman, A. & Kuipers, L. Nanowire Plasmon Excitation by Adiabatic Mode Transformation. *Physical Review Letters* **102**, 203904 (2009).
  254. Novotny, L. Effective wavelength scaling for optical antennas. *Physical review letters* **98**, 266802 (2007).
  255. Dorfmueller, J. *et al.* Plasmonic nanowire antennas: experiment, simulation, and theory. *Nano letters* **10**, 3596-3603 (2010).
  256. Huang, J.-S. *et al.* Mode Imaging and Selection in Strongly Coupled Nanoantennas. *Nano letters* 2105-2110 (2010).doi:10.1021/nl100614p
  257. Yu, N. *et al.* Light propagation with phase discontinuities: generalized laws of reflection and refraction. *Science* **334**, 333-7 (2011).
  258. Agio, M. Optical antennas as nanoscale resonators. *Nanoscale* **4**, 692-706 (2012).

259. Taminiau, T.H., Stefani, F.D. & van Hulst, N.F. Optical nanorod antennas modeled as cavities for dipolar emitters: evolution of sub- and super-radiant modes. *Nano letters* **11**, 1020-1024 (2011).
260. Utikal, T., Stockman, M.I., Heberle, A.P., Lippitz, M. & Giessen, H. All-Optical Control of the Ultrafast Dynamics of a Hybrid Plasmonic System. *Physical Review Letters* **104**, 113903 (2010).
261. Schumacher, T. *et al.* Nanoantenna-enhanced ultrafast nonlinear spectroscopy of a single gold nanoparticle. *Nature communications* **2**, 333 (2011).
262. Ghenuche, P., Cherukulappurath, S., Taminiau, T.H., van Hulst, N.F. & Quidant, R. Spectroscopic Mode Mapping of Resonant Plasmon Nanoantennas. *Physical Review Letters* **101**, 116805 (2008).
263. Biagioni, P. *et al.* Dependence of the two-photon photoluminescence yield of gold nanostructures on the laser pulse duration. *Physical Review B* **80**, 45411 (2009).
264. Biagioni, P. *et al.* Dynamics of multi-photon photoluminescence in gold nanoantennas. *Arxiv* **1109.5475**, (2011).
265. Duan, H., Fernández-Domínguez, A.I., Bosman, M., Maier, S. a & Yang, J.K.W. Nanoplasmonics: Classical down to the Nanometer Scale. *Nano letters* (2012).doi:10.1021/nl3001309